

2023

Improving the recovery efficiency of the Aquifer Storage and Recovery system in Hoorn



Dylan C. Dirks

Delft University of Technology

Faculty of Civil Engineering and Geosciences





TECHNICAL UNIVERSITY OF DELFT
Faculty of Civil Engineering
(Water Management)

Improving the recovery efficiency of the Aquifer Storage and Recovery system in Hoorn

A Thesis submitted in partial fulfillment of the requirements of
Master of Science in Civil Engineering
(Water Management)

by

Dylan Dirks

Bachelor of Science in Civil Engineering
Delft University of Technology, 2020

Supervised By

Mark Bakker (TU Delft)

Bas des Tombe (PWN)

Lucas Borst (PWN)

Delft, 2023

Preface

This report has been written as a graduation project for the Master's program in Water Management at TU Delft. Through this report, I demonstrate my ability to comprehend complex projects using my knowledge and skills. I can identify project bottlenecks and translate them into potential solutions. By doing so, I showcase my professional competence and readiness to take the next step in my career.

I would like to express my gratitude to PWN for the opportunity they have given me to investigate this fantastic project. The ASR system was a wonderful example of a project where hydrology and modeling come together, which aligns with my passion. I had the privilege of working in an amazing team where the positive atmosphere made it a pleasure to work in the office.

Furthermore, I would like to extend my gratitude to Lucas Borst, who was closely involved in the implementation and monitoring of the ASR system. He was always willing to brainstorm solutions for any challenges I encountered throughout the process. With his knowledge and expertise, he helped me fill in the gaps. Moreover, his engagement and positive attitude played a vital role in keeping me motivated throughout the research.

I would also like to express my gratitude to Mark Bakker, who was willing to supervise me from TU Delft. One of my stumbling blocks is my tendency to rush and take on too much at once. Mark was able to provide guidance at the right moments during the research. As a result, I was able to work towards the final outcome step by step and avoid getting stuck in the meantime. His knowledge also contributed to the valuable result.

Lastly, I would like to thank Bas des Tombe, who was willing to supervise me from PWN. He was highly involved and regularly provided critical feedback on the progress of the research and interim results. Additionally, when necessary, he was able to provide technical support related to the modeling aspects. During conversations with Bas, his enthusiasm often rubbed off on me. It gave me a sense of heading in the right direction and helped maintain my motivation.

Summary

PWN is responsible for supplying sufficient quantities of high-quality water to its customers. The growing population and the effects of climate change, such as heat waves and droughts, are straining the capacity of the water supply network, especially during dry and warm periods when water demand increases. A significant portion of the drinking water is produced in Andijk. From there, the drinking water is transported to Hoorn, where it is further distributed to customers. The connection between Andijk and Hoorn is therefore crucial, and in the event of a pipeline failure due to a calamity or maintenance, capacity issues can arise. To maintain the redundancy of this connection and to smooth out the daily water demand and supply fluctuations, PWN is exploring the implementation of an Aquifer Storage and Recovery (ASR) system in Hoorn. The ASR system in Hoorn faces strict requirements, which address the challenge of maintaining water quality standards and optimising recovery efficiency. These requirements must ensure that the extracted water remains suitable for consumption, with no more than 1% dilution with ambient groundwater. The objective of this study is to identify a method to improve the recovery efficiency of the ASR system in Hoorn.

The ASR system operates by injecting drinking water into an aquifer during periods of water availability and recovering it when needed. Compared to installing a new pipeline, the ASR system offers a more cost-effective solution with additional benefits such as space efficiency and temperature stability. However, the ASR system in Hoorn faces challenges related to maintaining water quality standards and optimising recovery efficiency. Processes such as lateral flow, dispersion, and buoyancy affect the system's performance, and a thorough understanding of these processes is crucial for accurately predicting recovery efficiency. A comprehensive analysis of a pilot ASR system in Hoorn was conducted by PWN to address these challenges. The pilot system consists of a single well where two pumps operate at two different filter depths in an aquifer. In the final layout of the ASR, additional wells are necessary to achieve the desired capacity.

A radially symmetric model was used to simulate groundwater flow, conservative solute transport, and heat transport. Due to the stringent water quality requirements, the radially symmetric model must accurately capture essential processes in an Aquifer Storage and Recovery (ASR) system, such as flow, dispersion, retardation, and buoyancy. The performance of a radial symmetric model in SEAWAT and MODFLOW 6 was assessed based on analytical methods and 3D models. Through this analysis, it was decided to utilise a radial symmetric model in SEAWAT due to the presence of numerical dispersion in a model using MODFLOW 6.

After this analysis, the model's performance was tested against various measurements, including hydraulic head, temperature, and electrical conductivity. It is evident that the model effectively captures both solute transport and heat transport. Discrepancies between measurements and the model can be attributed to assumptions made during the study and uncertainties in the measured values. However, the presence of clay layers between the deep and shallow filters in the pumping well significantly contributes to local differences between the model and the measurements. The main reason for this difference is that these layers are not homogeneous throughout the depths, allowing water to flow between them. This heterogeneity cannot be simulated with a radially symmetric model. However, despite this heterogeneity, these clay layers consistently result in low recovery efficiency in the current system.

The objective of this study was to identify a method to improve the recovery efficiency of the ASR system in Hoorn. The current system has a recovery efficiency of about 30%. This can be improved by implementing a check valve in the shallow filter of the pump well, with 60% to 65% of the filter dedicated to recovery to achieve a recovery efficiency of 80%. During the testing of this system, an injection period was followed by a recovery period with specific pumping rates. It took three cycles to achieve the desired recovery efficiency. It is important to note that these

cycles did not include storage and rest phases. The system's recovery efficiency may change when these phases are incorporated. However, an important assumption is that homogeneous layers are present. Heterogeneity of layers can lead to deviations from the modelled recovery efficiency.

This research contributes to a better understanding of the pilot ASR system in Hoorn and provides insights into improving its recovery efficiency. With the lessons learned from this study, PWN can assist in developing the final design for the ASR system. This design will involve multiple wells to meet the required capacity.

Table of Contents

Preface	i
Abstract	iii
1 Introduction	1
2 Aquifer Storage and Recovery (ASR) system in a saline aquifer	4
2.1 Introduction	4
2.2 Lateral Flow	5
2.3 Mixing	5
2.4 Density driven flow	6
2.5 Aquifer type	7
3 Pilot ASR system in Hoorn	8
3.1 Introduction	8
3.2 Aquifer properties	8
3.3 Design of the pumping well	10
3.4 Water quality	10
3.4.1 Recovered water quality	10
3.4.2 Temperature	11
3.4.3 Electrical Conductivity	12
3.5 Types of measurements	13
3.5.1 Online monitoring in the pumping well	13
3.5.2 Distributed Temperature Sensing	14
3.5.3 Borehole logging	14
3.5.4 Data loggers in observation wells	15
3.5.5 Sampling and field measurements	15
3.6 Pilot cycles	16
4 Modeling groundwater flow	17
4.1 Introduction	17
4.2 Analytical solutions	18
4.2.1 Confined flow in steady state	18
4.2.2 Semi confined flow in steady state	18
4.2.3 Semi confined transient flow	19
4.3 Radial model	19
4.4 Test case	20
4.5 Results	22
4.5.1 Confined flow in steady state	22
4.5.2 Semi confined flow in steady state	22
4.5.3 Semi confined transient flow	23
5 Modeling transport of heat and solutes in an ASR system	24
5.1 Introduction	24
5.2 Method	24
5.3 Results	26
5.3.1 Advection	26
5.3.2 Dispersion	26

5.3.3	Numerical Dispersion	28
5.3.4	Sorption	30
5.3.5	Buoyancy	31
5.3.6	Computation times	31
6	Modeling the ASR system in Hoorn	32
6.1	Method	32
6.1.1	Estimation of the horizontal hydraulic conductivity	32
6.1.2	Estimation of the retardation in heat transport	32
6.1.3	Refining horizontal hydraulic conductivity and heat retardation	32
6.1.4	Estimation of the porosity	33
6.1.5	Estimation of the buoyancy	33
6.1.6	Estimation of dispersion	33
6.2	Model design	33
6.2.1	Discretization	33
6.2.2	Aquifer properties	34
6.2.3	Model features	35
6.3	Results	37
6.3.1	Hydraulic head change	37
6.3.2	Heat transport	38
6.3.3	Solute transport	40
7	The potential of the ASR system in Hoorn	44
7.1	Introduction	44
7.2	Influence of the clay layers between the two pump filters	45
7.2.1	Current situation	45
7.2.2	Single clay layer	47
7.2.3	No clay layer	48
7.3	Pumping water around the clay layers between the two pump filters	49
7.4	Using a check valve	50
8	Conclusions and recommendations	52
8.1	Conclusions	52
8.1.1	Key processes resulting in losses of recoverable water of the ASR system	52
8.1.2	Modeling the ASR system using heat and conservative solute transport	52
8.1.3	Modeling the recovery efficiency of the ASR system	53
8.1.4	Influence of the clay layers around -85 mNAP and -90 mNAP	53
8.1.5	Improving the monitoring system of the ASR system	54
8.1.6	Improving the recovery efficiency of the ASR system in Hoorn	54
8.2	Recommendations	54
	References	56
	Appendices	58
	A Cycle operational values	58
	B Numerical dispersion	59
	C Borehole measurement at the ASR well	60

D	Hydraulic head change at filter depths in observation wells 19FNW012 and 19FNW004	61
E	Temperature at filter depths in the pumping well and observation wells	63
F	Electrical Conductivity at filter depths in the pumping well and observation wells	64
G	Iterative parameter estimation	65
H	Important python code	66
H.1	SEAWAT model	66
H.2	Model input	68
H.2.1	Discretization	68
H.2.2	Aquifer properties	69
H.2.3	Initial conditions	70
H.2.4	Model features	70
H.2.5	Solver criteria	74

1 Introduction

PWN is responsible for delivering enough quantities of water with decent quality to customers (PWN, 2022). The water demand is higher during dry and warm periods, because people use water to fill pools, are showering and watering the garden more often during these periods (Drinkwaterplatform, 2022). Furthermore, water consumption varies throughout the day, with higher demand in the morning and afternoon due to showering habits. The network of PWN is designed to satisfy the demand during these maximum conditions (Spierenburg, Zuurbier, & Borst, 2020). However, the drinking water demand increases and this might lead to capacity problems in the future (Spierenburg & Borst, 2019). The increasing drinking water demand is mainly caused by an increasing population. Moreover, climate change is causing longer and more frequent heat waves and droughts, which further intensify the demand for drinking water. (Cirkel, Blokker, & Dorland, 2016).

The connection between Andijk and Hoorn is one of the expected bottlenecks in the network of PWN. Approximately one-third of the drinking water is produced in Andijk, and the majority of it is distributed through Hoorn (Spierenburg et al., 2020). This shows the importance of this connection regarding reliability of the network. Figure 1.1 shows the main connections between Andijk and Hoorn, consisting of one transport pipeline and a smaller distribution pipeline. During a calamity or maintenance in the transport pipeline, drinking water is distributed through the smaller one. This pipeline has a smaller capacity causing less, but still enough transport of drinking water to Hoorn (Spierenburg et al., 2020). PWN expects that the increasing demand for water, particularly during a calamity or maintenance of the transport pipeline, will lead to insufficient capacity between Hoorn and Andijk.

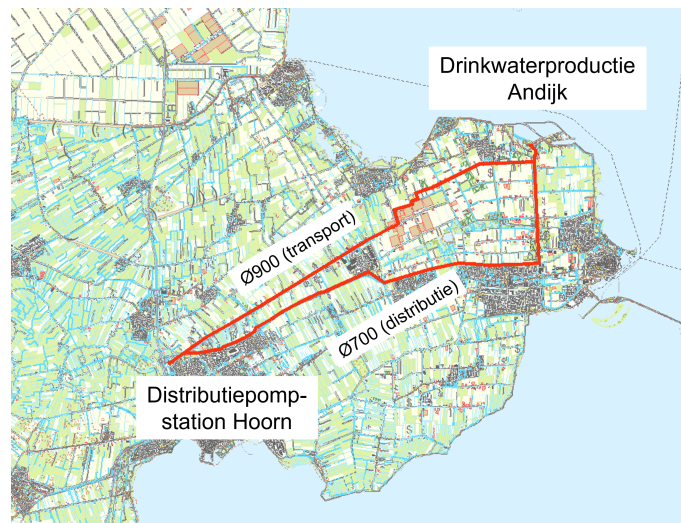


Figure 1.1: Location main pipelines between Hoorn and Andijk (Spierenburg & Borst, 2019).

Traditionally, capacity issues are resolved by installing a new pipeline. This solution, however, is costly, particularly given that the pipeline will only be used during calamities or maintenance between Andijk and Hoorn (Spierenburg et al., 2020). As a result, PWN is exploring the potential of an Aquifer Storage and Recovery (ASR) system. This system works by injecting drinking water into an aquifer using a well when water is available, where it is then stored until it is needed, and later retrieved using the same well (Zuurbier, 2016). In comparison to the redundant pipeline, this system presents a more cost-effective construction option with additional benefits. An ASR

system does not require a large above-ground space like a reservoir, has fewer fluctuations in temperature, and does not experience water loss due to evaporation (Zuurbier, Paalman, van Loon, & Stuyfzand, 2013). PWN desires to use the ASR during calamities, but additionally is able to cover daily peaks as well. The latter contributes to a more efficient provision or production of drinking water and could help build a more reliable and robust drinking water network (Spierenburg et al., 2020).

The ASR system in Hoorn injects water of drinking water quality into an aquifer. This water is surrounded by ambient groundwater, which does not meet drinking water quality requirements. Zuurbier, Ros, and Stuyfzand (2018) reports that even a very limited mixing of both waters already causes the water being unsuitable as drinking water. The report is based on standards in accordance with Dutch drinking water quality regulations. Nevertheless, PWN has established even more strict target values to prevent any potential issues during the distribution of drinking water. While many of these targets can be successfully met, the presence of ammonium remains a significant obstacle. This means that the ASR system in Hoorn is not permitted to extract more than 1% of ambient groundwater (Spierenburg & Borst, 2023).

The ratio of the volume of drinking water recovered relative to the injected volume is called the recovery efficiency, and is used to assess the performance of an ASR. There are losses, which negatively affect the recovery efficiency of an ASR system. Four main processes are considered in this report. First two processes are groundwater flow and density driven flow which can cause earlier extraction of ambient groundwater. Other two processes are dispersivity and diffusivity, which cause mixing of injected water and ambient groundwater. Chapter 2 provides further details on these processes.

PWN investigated in collaboration with KWR possibilities of installing an ASR system located nearby pumping station Hoorn. In 2020, PWN constructed one ASR well and initiated a pilot program to test various cycles. However, uncertainties in the transport of injected water were observed during the pilot. During the construction of the pumping well unexpected clay layers were found at depths around -85 and -90 mNAP. The impact of this layer was still unclear. Since PWN desires to scale up to a larger system, they urge to understand and improve the functioning of the pilot ASR system. The pilot is studied in this thesis to get a better understanding of the ASR system in Hoorn and improve its performance. This problem statement results in the following main objective:

How can the recovery efficiency of the ASR system in Hoorn be improved?

The objective is divided in the following research questions:

- What are the key processes that result in losses of recoverable water in the ASR system in Hoorn?
- How to model the ASR system accurately using heat and conservative solute transport?
- How to model the recovery efficiency of the ASR system in Hoorn?
- How does the presence or absence of a clay layer between the deep and shallow filters in the pumping well influence the recovery efficiency of the ASR system?
- How can the design and monitoring system of the aquifer storage and recovery system be improved?

This report is structured into eight chapters, each addressing specific aspects of the ASR system. Chapter 2 provides an introduction to the system, highlighting its importance and outlining the key processes that result in losses of recoverable water. Chapter 3 focuses on the pilot ASR

system implemented in Hoorn, discussing the aquifer properties, design considerations, and water quality aspects. Furthermore, it examines various types of measurements conducted. Chapter 4 introduces the modeling of groundwater flow using a radial model, providing a foundation for further analysis. This model is expanded in Chapter 5 to incorporate the transport of heat and solutes, enabling a more comprehensive assessment. Chapter 6 focuses specifically on the modeling of the ASR system in Hoorn, integrating all relevant factors and processes and a comparison with measurements. Chapter 7 assesses the potential of the ASR system in Hoorn, analyzing the influence of clay layers and exploring alternative approaches to improve the performance of the ASR system. The report concludes with Chapter 8, which provides overall conclusions and recommendations based on the findings and insights gained throughout the study.

2 Aquifer Storage and Recovery (ASR) system in a saline aquifer

This chapter aims to present key conditions in the design and location of the Aquifer Storage and Recovery (ASR) system. First the ASR system in general is explained in Section 2.1. The chapter continues with main boundary conditions as lateral flow (Section 2.2), dispersive mixing (Section 2.3), density driven flow (Section 2.4) and the aquifer type (Section 2.5).

2.1 Introduction

An ASR system consists of a pumping well injecting and extracting water to an aquifer. This happens in a cycle of four phases; injection, storage, recovery and rest. The first phase is when water is injected in an aquifer through a well, shown on the left side of figure 2.1. The injection phases usually takes place during times when there is enough water available. The injected water displaces ambient groundwater and creates an interface or mixing zone (Luo et al., 2014). The storage phase is shown in the middle of figure 2.1, neither water is extracted nor injected during this phase. The right side of figure 2.1 is showing the recovery phase. Stored water will be pumped out of the aquifer when water is needed, for example during scarcity. After these three phases the ASR system is at rest which completes the ASR cycle.

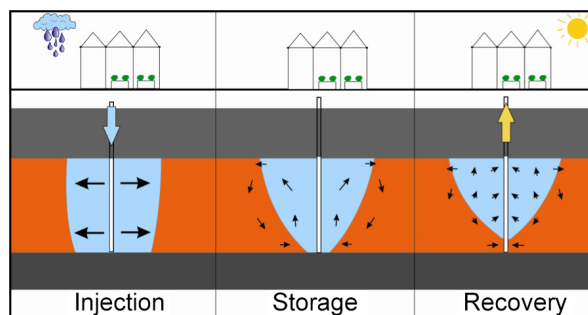


Figure 2.1: *Three operational phases of the ASR system (Zuurbier, 2016).*

An ASR system offers a few advantages over above ground storage. One of these benefits is the elimination of the need for above ground space, which is becoming increasingly scarce. In addition, the water is protected from external influences. This means that there is no evaporation, no undesired deposition and less temperature fluctuations compared to above ground reservoirs. The water quality remains consistent over time, except for the edges where injected water undergoes mixing (detailed further in Section 2.3), providing two notable advantages. First, there is no need for advanced post treatment. Secondly, it is possible to store water for longer periods (Zuurbier et al., 2013).

The separation between the injected drinking water and the surrounding groundwater is crucial for the functioning of an ASR system. In a saline aquifer, this separation occurs primarily due to density differences between the two water types (Cooper et al., 1964). The injected drinking water, being fresher (lighter), is less dense than the surrounding groundwater, which is saltier (heavier). However, the exact location of this separation depends on various factors. These factors include those influencing the movement of the interface, such as lateral flow, as well as factors affecting the thickness of the interface, such as dispersion. Additionally, natural barriers like clay layers play a role in the separation process by restricting the movement of water through them (Cooper et al., 1964).

In saline aquifers it is impossible to reach a recovery efficiency of 100% (Zuurbier, 2016). Lateral flow, density-driven flow and dispersive mixing are major processes causing a decrease in recovery efficiency. It is hard to predict to what extent these processes influence the amount of recoverable water, since they are site specific and depends on operational settings (Ward et al., 2009). The subsequent sections provide a more detailed explanation of the primary influential losses.

2.2 Lateral Flow

Lateral flow is caused by presence of a background hydraulic gradient. The phases in an ASR system (injection, storage, recovery and rest) influence the hydraulic gradient, which might cause a change in direction and magnitude of lateral flow (Ward et al., 2009). Figure 2.2 is an example showing the change of lateral flow in an ASR system. Without a well, groundwater is flowing from left to right, indicated as "regional flow" in the figure. On the sides of the figure change of magnitude and/or direction of lateral flow (black arrows) clearly shows differences between phases. It is however important to note that every phase independently influences lateral flow in an aquifer (Ward et al., 2009). Lateral flow causes transport of injected water away from the well. This leads to a reduction of the recovery efficiency since injected water will be partially or fully inaccessible (Ward et al., 2009).

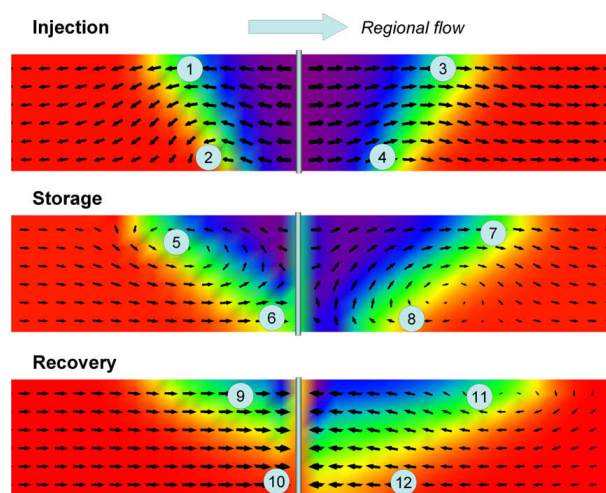


Figure 2.2: Lateral flow, indicated with black arrows, during an ASR cycle (Ward et al., 2009).

2.3 Mixing

During an ASR cycle inevitable reduction of recovery efficiency is caused by mixing of injected water with ambient groundwater. As shown in figure 2.3 this mixing only happens at the edges of injected water, creating a transition zone (Ward et al., 2009). There are two distinct processes involved in mixing the two types of water: diffusion and mechanical mixing.

Diffusion occurs when there is a gradient in the concentration of a substance between two points within an aquifer. In this process, molecules of the substance naturally migrate from regions of higher concentration to regions of lower concentration. This movement persists until equilibrium is attained, effectively spreading the substance through the groundwater (Langevin et al., 2022a).

Mechanical mixing refers to the spreading of solutes in groundwater due to variations in flow velocity and direction. It occurs for example when groundwater flows through heterogeneous or non-uniform porous media, such as aquifers with varying permeability or geological formations with irregularities. As water moves through these complex pathways, the flow velocity may change, causing the groundwater to travel at different speeds and directions (Langevin et al., 2022a). Mechanical mixing and diffusion together are referred to as hydrodynamic dispersion, which is described as follows (Negm & Eltarabily, 2017):

$$D = \alpha|v| + D_f \quad (2.1)$$

where D is the hydrodynamic dispersion, α is the dispersivity, v is the velocity and D_f is the diffusion coefficient. Both diffusion and mechanical mixing contribute to the transition zone. When this mixed water is not recovered, the size of this zone increases with multiple cycles. The concentration gradients that drive diffusion gradually decrease over time, resulting in reduced diffusion. As the transition zone expands, the boundary of the ambient groundwater moves farther away from the well. Flow velocities at the boundary are lower compared to close to the well. This means that mechanical mixing is also lower at the edge. In combination with the enlargement of the transition zone, the influence of mechanical mixing diminishes (Zuurbier, 2016).

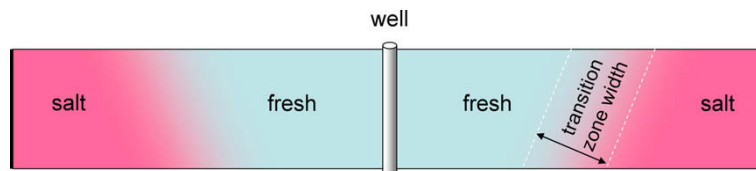


Figure 2.3: *Dispersive mixing causing a transition zone (Ward et al., 2009).*

2.4 Density driven flow

Brackish or saline groundwater has a higher density than injected (fresh) water. In an ASR system this difference in density causes lighter freshwater to float above more dense brackish or saline water, which flows down and inwards. This process is called the buoyancy effect and even small differences in density could cause this effect (Ward et al., 2009). As shown in figure 2.4, the buoyancy effect causes lifting of fresher water into a conical shape. During the recovery phase this leads to earlier extraction of (poor quality) ambient groundwater.

The thickness of the transition zone has a major impact on how fast buoyancy effects takes place in the aquifer (Ward et al., 2009). A large zone means a smoother transition in density from injected drinking water to denser ambient groundwater, creating more resistance against buoyancy effects.

The magnitude of the buoyancy effect in an aquifer is heavily influenced by both the absolute value and the ratio of horizontal to vertical hydraulic conductivity. A lower absolute value of the vertical hydraulic conductivity will result in a slower vertical movement of water, making the buoyancy effect more prominent. Similarly, a higher ratio of horizontal to vertical hydraulic conductivity (i.e., a more anisotropic medium) will lead to a reduced buoyancy effect, as water prefers to flow in the direction of higher hydraulic conductivity (Ward et al., 2009).

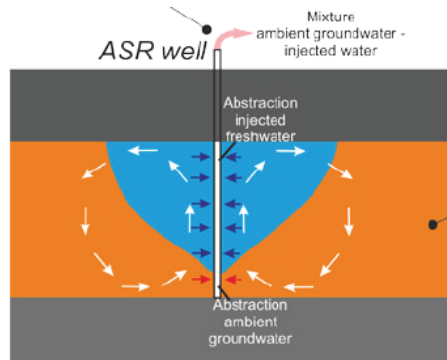


Figure 2.4: *Transport of injected water due to the buoyancy effect (Zuurbier, 2016).*

2.5 Aquifer type

It is not possible to achieve a 100% recovery efficiency because there is no location where none of the mentioned processes (lateral flow, density-driven flow, and dispersive mixing) occur (Ward et al., 2009). However, there are some characteristics with a positive effect on the recovery efficiency. Examples are a small density difference between the injected fresh water and ambient groundwater, anisotropic aquifer, small background flow rate, closure of the target aquifer and a small aquifer thickness (Zuurbier, 2016).

The confinement of the aquifer creates a hydraulic barrier that reduces the potential for injected water to move outside the aquifer. Additionally, in a confined aquifer, the injected water tends to remain close to the ASR well due to the increased pressure of ambient groundwater. Confined aquifer systems thus allow better management of injected water resulting in a higher recovery rate compared to unconfined systems (Martin & Dillon, 2002).

In some cases, aquifers may not be fully confined, resulting in changes in the water table during injection and recovery in shallower aquifers. However, this effect is less significant in deeper aquifers, making them better suited for storing larger quantities of water (Martin & Dillon, 2002).

3 Pilot ASR system in Hoorn

This chapter aims to present important properties of the pilot ASR system in Hoorn with respect to this study. It starts with a small introduction elaborating on site characteristics, and the purpose of the ASR system in Section 3.1. It continues with the composition and properties of the surrounding soil in Section 3.2. Moving forward, the design of the pumping well is described in Section 3.3. Relevant aspects of water quality and types of measurements are described in Section 3.4 and Section 3.5 respectively. Finally, this chapter presents the pilot cycles performed by PWN in Section 3.6.

3.1 Introduction

PWN decided to locate the ASR system on a grass field next to pumping station at Hoorn (see figure 3.1). Around this area there are no other registered extractions of groundwater by other users (Borst, 2020). Variations in groundwater levels are directly related to natural processes and the ASR, which helps easier monitoring the influence of the ASR.

It has been found that the hydraulic head in an area about 2.5km is not varying that much (Borst, 2020), meaning there is almost no lateral flow in the aquifer. Taking into consideration the thick low permeable clay layer on top of the aquifer, this results in little variations of the ground water table at the surface (Borst, 2020).

As mentioned in Section 1, the purpose of the ASR system is to use it during a calamity, big maintenance and covering daily peaks. A maximum capacity of 1000 m³/h is necessary for a maximum of three weeks (Spierenburg & Borst, 2020a) to ensure adequate supply. PWN estimated that achieving this capacity would require around 8 to 12 wells in the surrounding area.



Figure 3.1: *The location of the ASR (left) and pumping station (right) at exit 9 of the E22 towards Hoorn North. (Borst, 2020).*

3.2 Aquifer properties

Based on historical data, various borehole drilling, and a sieve analysis, important aquifer properties were estimated around the ASR system. Figure 3.2 shows the soil profiles based on borehole drilling at the pump well location (19FNPHO01), 8.3 m away from the pump well (19FNW012), and 12.3 m away from the pump well (19FNW004). In the borehole drilling of 19FNW004, a sieve analysis was also conducted, providing an initial estimation of aquifer properties.

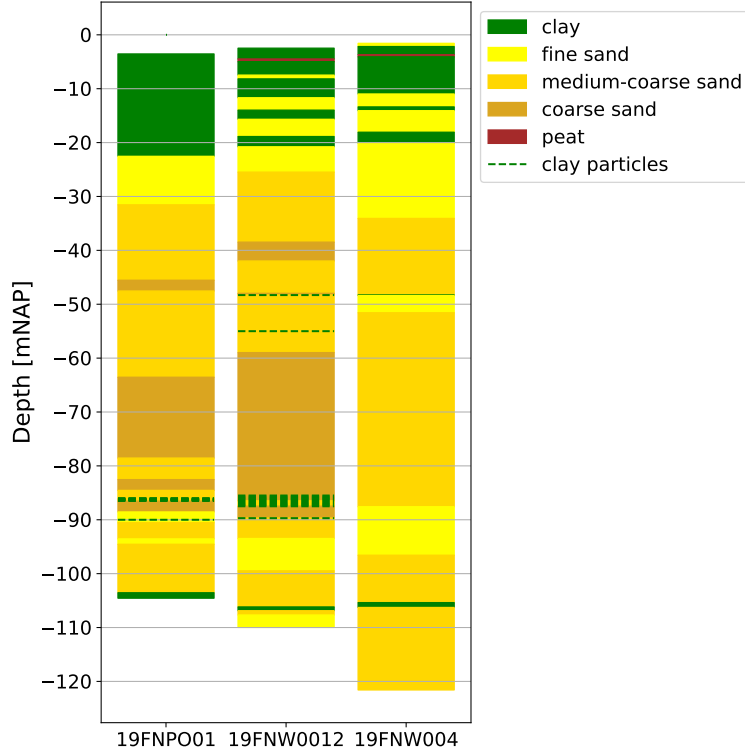


Figure 3.2: *Regional soil composition based on borehole drilling in the pumping well (19FPHO01) and observation wells (19FNW012 and 19FNW004).*

Up to a depth of approximately -20 mNAP, the soil consists of a Holocene cover layer. The heterogeneity of the soil composition in this layer is mainly caused by the fact that the area used to be a peatland with a high altitude with a lot of small rivers which are filled with sand over time (Spierenburg & Borst, 2020a). Following are sandy layers varying in coarseness up to a depth of approximately -48 mNAP. Around this depth, a thin clay layer has been discovered. It is unclear how permeable this clay layer is. Below this clay layer, coarse and medium-coarse sand layers have been found down to a depth of approximately -90 mNAP. Historical data indicates that these sediments are deposits from the River Rijn (Borst, 2023). As shown in Figure 3.2, clay layers have also been found in this package at both the pumping well and observation well 19FNW012, at approximately -85 mNAP and -90 mNAP, which were not found in observation well 19FNW004. The spatial presence of these clay layers is unclear. Beneath these layers, the soil consists of fine, medium-coarse, and coarse sand layers down to a depth of approximately -105 mNAP, where a clay layer of about 1 to 1.5 meters is present. Historical data indicates that the heterogeneity of these clay and sand layers is due to deposits from strongly meandering rivers that existed in the environment of the ASR in the distant past. The influence of these strongly meandering rivers can be traced down to a depth of -285 mNAP, where the Maassluis formation is found. This formation consists of shallow-marine sands and clay (Borst, 2023).

Table 3.1 presents initial estimates of the transmissivity for the different sand layers and the resistance of the clay layers. These values are based on Spierenburg et al. (2020) and Zuurbier et al. (2018). Additionally, values from these reports are used as initial estimates for the porosity and specific storage coefficient. This means a porosity of approximately 0.35 and a specific storage

coefficient between 10^{-6} m^{-1} and 10^{-8} m^{-1} are assumed for the sand layers. Meanwhile, a porosity of about 0.2 and a storage coefficient between 10^{-3} m^{-1} and 10^{-6} m^{-1} are assumed for the clay layers.

Table 3.1: *Estimated transmissivity, resistance and main soil type of different layers.*

Top	Bottom	Soil type	T	c
[mNAP]	[mNAP]	[-]	[m ² /d]	[d]
0	-20	Clay		800-2000
-20	-48	Sand	500-1000	
-48	-48.5	Clay		2-10
-48.5	-85	Sand	1500-2500	
-85	-87	Clay		?
-87	-89	Sand	1500-2500	
-89	-90	Clay		0-1
-90	-105	Sand	1500-2500	
-105	-106	Clay		50-1000
-106	-285	Sand	8000-10000	

3.3 Design of the pumping well

The pumping well has a depth of -105 mNAP from which water is pumped from the second aquifer (i.e., between -48.5 mNAP and -105 mNAP) using two different pumps that operate at different filter depths. The shallow filter is situated roughly between -50 mNAP and -80 mNAP, while the deep filter is found between -90 mNAP and -100 mNAP. The Multi-Partially Penetrating Well (MPPW) concept is employed, where injection occurs at both depths, and only shallow extraction is carried out, as illustrated in Figure 3.4 (Spierenburg et al., 2020). The deeper filter helps to slow down the movement of the fresh-salt interface towards the shallow filter, which is caused by buoyancy effects (Zuurbier et al., 2013). It has been demonstrated that Multiple Partially Penetrating Wells (MPPWs) result in higher recovery efficiency (Zuurbier, 2016).

3.4 Water quality

3.4.1 Recovered water quality

PWN assessed the groundwater quality in the vicinity of the ASR by analyzing water samples collected from observation wells as described in Section 3.5.5. Two guidelines were employed for this analysis: the first being the Dutch drinking water standard, and the second being the target values set by PWN. The latter guidelines are more stringent as they take into account distribution of drinking water, which might influence the drinking water quality (Stuyfzand & Borst, 2022). For two main reasons, PWN wishes that the extracted water from the ASR does not require extensive post-treatment. Firstly, due to the cost involved, and secondly, due to the quick deployability of the extracted water, as the ASR will be used during calamities.

The analysis of PWN has revealed that the standards for oxygen, methane, total hardness, iron, manganese, ammonium, and arsenic are not met after recovery (Spierenburg & Borst, 2023). By adding an aeration step after extraction, the target values for oxygen and methane can still be achieved. In addition, target values for total hardness, iron, arsenic, and manganese can be achieved by mixing recovered water with drinking water stored in the pumping station adjacent

to the ASR system, shown on the right in Figure 3.1. However, the target values for ammonium cannot be achieved, which means that only a dilution of 1% with ambient water is permitted (Stuyfzand & Borst, 2022).

It is important to map the boundary of the injected drinking water in the aquifer so the amount of recoverable water can be estimated. In this study, Electrical Conductivity (EC) and temperature were used for this purpose. These are both parameters that can easily be measured accurately and serve as tracers for tracking the movement of water. Both parameters are described in the following sections.

3.4.2 Temperature

Changes in soil temperatures mainly occur up to a depth of 10 meters. Beyond this depth, the temperature of the soil remains relatively stable. The temperature of the soil (e.g. ambient groundwater temperature) is around 10.5 °C to 11 °C. Conversely, the temperature of infiltrating water varies seasonally due to its source, the IJsselmeer, which experiences seasonal fluctuations. In winter, the temperature can drop to 5 °C, whereas in summer, it can rise to 20 °C (Stuyfzand & Borst, 2022). The initial conditions of the temperature in the soil were determined using Distributed Temperature Sensing (DTS) measurements (explained in Section 3.5.2). Figure 3.3 is showing the initial temperature of this analysis.

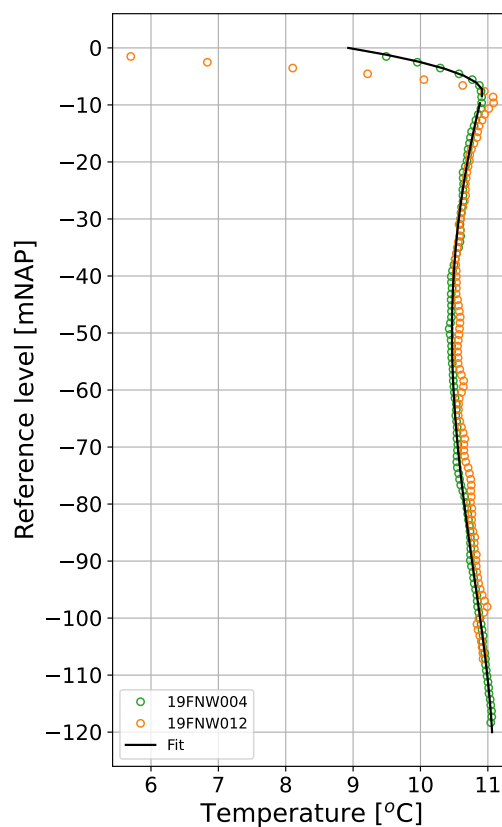


Figure 3.3: Initial temperature (black line) is based on DTS measurements before any pumpig activities were present.

3.4.3 Electrical Conductivity

The electrical conductivity (EC) is a measure of the ability of a material to conduct electric current. In water, dissolved salts conduct current by releasing free ions. As a result, the conductivity of water increases with higher salt concentrations (Chadd, 2023). This property makes the EC an important measure for determining the salinity (Rhoades, Kandiah, & Mashali, 1992). Saline Agriculture Worldwide (2023) has developed an estimation for different water types based on their salinity levels, which is presented in Table 3.2.

Table 3.2: Estimation for different water types based on their salinity levels (Saline Agriculture Worldwide, 2023).

Classification	Electrical Conductivity [$\mu\text{S}/\text{cm}$]
Fresh water	800
Slightly brackish	1700
Medium brackish	1700 - 8000
Brackish	8000 - 25000
Strong brackish	25000 - 58000
Sea water	58000

Based on measurements, the conductivity of groundwater around the ASR has been determined. Figure 3.4 depicts the measured EC in the soil. Until a depth of approximately -65 mNAP, the EC is relatively low, indicating the presence of relatively fresh water. As discussed in Section 2.4, fresh water has a lower density compared to saltwater. Drinking water is also fresh, and as discussed in this section, small differences between the injected water and the ambient groundwater have a positive influence on the recovery efficiency. From around -65 mNAP, the water becomes saltier, and therefore denser. It is expected that buoyancy effects will play a more significant role in this region, as the differences between the injected water and the ambient groundwater also increase.

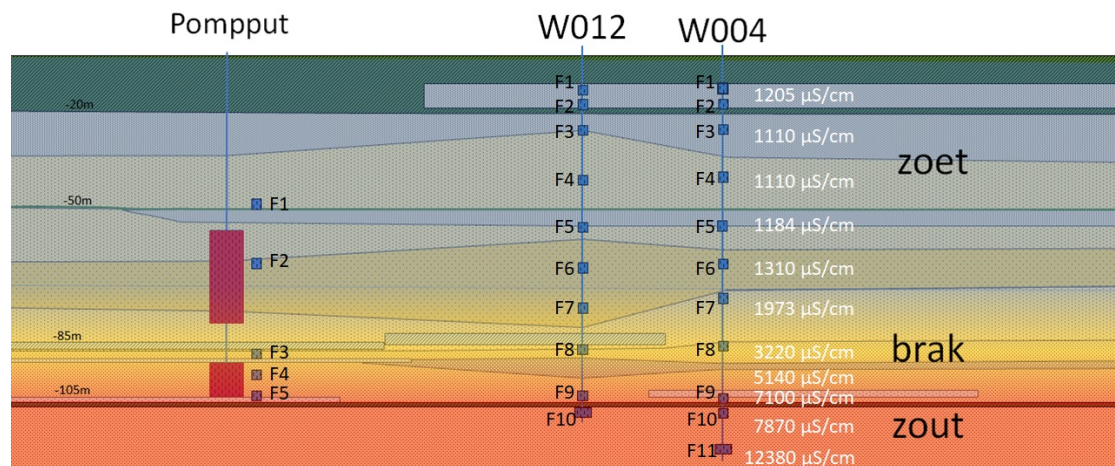


Figure 3.4: Sketch of the cross-section showing the filters from where water is pumped on the left side in red, the filters in the pumping well and observation wells where measurements are taken in blue, and on the right side, the measured EC values across the depth (Borst, 2022).

The injected drinking water has a different temperature than the ambient water. The temperature affects the ion activity of the water and thus the EC. A high temperature of water means higher EC and vice versa. Since the temperature can vary between the injected water and ambient water, measurements are corrected. This has been done by correcting each EC measurement to a temperature of 20 °C.

3.5 Types of measurements

The performance of the ASR is monitored by using different types of measurements. In this study, measurements from the pumping well (19FNPHO01) and an observation well at a distance of 8.3 m (19FNW012) and an observation well at a distance of 12.3 m (19FNW004) were used. These measurements include Distributed Temperature Sensing (DTS), borehole logging, data loggers and sampling (Spierenburg & Borst, 2020b). Both the pumping well and the two observation wells have different filters where measurements are taken, which are represented in blue in Figure 3.4. Table 3.3 shows the approximate depths at which these filters are located. Depending on desired information different measurements types are performed in these observation wells. For this research temperature, electrical conductivity and hydraulic head are important measured parameters. This section will elaborate on the methods used to measure these specific parameters.

Table 3.3: *Filter depths for the pumping well (19FNPHO01) and observation wells (19FNW012 and 19FNW004) and the distance of these wells relative to the pumping well (r).*

Well Code	Depth of different filters [mNAP]											r [m]
	1	2	3	4	5	6	7	8	9	10	11	
19FNPHO01	-46	-63	-86	-97	-103							0.0
19FNW004	-12	-17	-24	-38	-52	-64	-74	-88	-104	-108	-120	12.3
19FNW012	-12	-17	-24	-38	-52	-64	-76	-88	-104	-108		8.3

3.5.1 Online monitoring in the pumping well

The pumping well (19FNPHO01) is equipped with different types of sensors that perform measurements at 15-minute intervals. Both the deep and shallow filters (represented in red in Figure 3.4) measure flow rates as well as temperature and electrical conductivity (EC) (Stuyfzand & Borst, 2022). This online monitoring system in the pumping well serves as a valuable source of data, providing insights into the quality of the injected and extracted water. Because the EC values are temperature-dependent, PWN has corrected them to 20 °C. As discussed in Section 3.4.3, this is necessary to have comparable measurements.

In this study, these measurements are used on a daily basis. The measured temperature and EC values were recorded at the time of injection. The temperature of the injected water can vary between approximately 5 °C and 25 °C. These are also the extreme limits within which the model results should fall. The measured EC values serve as a minimum threshold in the study, as the maximum EC of the ambient groundwater has a higher value than the injected water. Since the measurements are taken by sensors, they are assumed to be reliable. However, due to the conversion of EC measurements, a small margin of error is taken into account in the corrected EC measurements.

3.5.2 Distributed Temperature Sensing

The Distributed Temperature Sensing (DTS) system provides temperature measurements along the entire length of a optic fibre cable. The system offers a high level of spatial resolution. DTS measurements need to be calibrated to ensure the accuracy and reliability of the temperature data. Calibration is necessary because various factors can influence the measurements, such as variations in cable characteristics, signal attenuation, and environmental conditions. By calibrating the DTS system, corrections can be applied to account for these influences and improve the accuracy of the temperature readings (Tombe, 2016).

PWN has installed fiber optic cables along the pump well to a depth of approximately -100 mNAP, observation well 19FNW012 to a depth of approximately -110 mNAP, and observation well 19FNW004 at -120 mNAP depth. Measurements are taken with a minimum frequency of once per hour and taken around every one meter depth. Additionally, they have calibrated these measurements. This technique offers continuous measurements, making it an important source of information for the temperature around the pumping well (Stuyfzand & Borst, 2022).

However, there are some uncertainties to consider. The placement of the cables may not be in a straight line along the wells but slightly entangled, which could cause minor deviations. Additionally, PWN states that the conversion of cable depths to ground surface level in the calibration process may have some discrepancies. This can significantly impact this study. Therefore, the DTS measurements are compared with temperature measurements obtained by CTD Divers (Section 3.5.4), and the results can be found in Appendix E. Based on this comparison, the DTS measurements in the pump well are adjusted downward by 3 meters, the measurements in observation well 19FNW012 are adjusted downward by 2 meters, and the measurements in observation well 19FNW004 are also adjusted downward by 2 meters.

3.5.3 Borehole logging

Borehole logging is carried out over the entire depth in the pumping well, observation well 19FNW012 and observation well 19FNW004 (Borst, 2022). These measurements are carried out to monitor the spread of injected drinking water. Gamma, Long, and Short Normal measurements are used to measure the resistance of layers at specific depths. These provide insight into the conductivity of the soil, where lithology, water quality, and water temperature play a role. The constant lithology enables the initial knowledge of water conductivity, as determined through an initial borehole logging. Consequently, the influence of lithology is established, allowing for the deduction of the Electrical Conductivity of water (Stuyfzand & Borst, 2022).

Borehole logging were conducted at specific moments. These moments were chosen to provide as much information as possible about the distribution of the injected water in the aquifer. Additionally, borehole logging provide values at every 5 cm depth, giving a continuous profile over the depth.

The measurements are quite precise and accurate, but they require various corrections for conversion to EC values. These corrections include adjusting for the formation factor of the soil and compensating for temperature variations. The formation factor differs for each measurement point and is not necessarily constant. This study did not consider the formation factor and temperature correction of borehole measurements. Therefore, these measured values were not used as absolute values, but rather as an indication of the flow of injected water in the aquifer.

3.5.4 Data loggers in observation wells

Each of the observation wells, mentioned in Table 3.3, has at least one Temperature Depth (TD) data logger installed to obtain continuous measurements (Spierenburg & Borst, 2020a). It should be noted that the loggers measure at a specific depth in a particular observation well. The hydraulic head can be derived from the hydrostatic pressure and depth, which are measured by the data logger. Conductivity Temperature Depth (CTD) data loggers were placed in specific filters of the pumping well and observation wells. These loggers measure the conductivity, temperature and hydraulic head at filter depth (Stuyfzand & Borst, 2022).

The measurements of hydraulic head exhibit a yearly fluctuation influenced by the seasons. However, this study focuses on the changes specifically caused by pumping activities. To isolate the effects of pumping, PWN conducted a time series analysis to remove the seasonal fluctuations from the data, resulting in a dataset that captures the pumping influences. The hydraulic head changes in filters 2 to 9 of the two observation wells (see Figure 3.4 and Table 3.3) were included in this study (see Appendix D). The data is recorded with a precision of 5 cm, but it is important to note that larger deviations may occur due to the application of the time series analysis.

In this study, temperature and EC measurements from loggers are used at the depths within the aquifer where the pumps are active. In the pumping well, measurements are available in filter 2, in observation well 19FNW012 in filters 6 to 9, and in observation well 19FNW004 in filters 5 to 8 (see Figure 3.4 and Table 3.3). Both components are measured with reasonable accuracy using the loggers. However, for EC measurements, a conversion step to 25 °C was applied, which may introduce a small margin in the interpretation of these measurements. The results on temperature measurements can be found in Appendix E, while the results on EC measurements can be found in Appendix F.

Furthermore, the data is retrieved by reading out loggers. This is done in the field, where the logger is removed from the well and reinserted after reading. It is possible that a logger is not placed back in the correct position, which can make the measurements unreliable or require correction. The magnitude of this error depends on how the logger is reinstalled. This means that these errors can be easily noticeable, with unexpected jumps in measurement values, but they can also be difficult to detect when the logger is slightly misaligned. It is also important to note that loggers have a limited lifespan, which means that over time, the quality of the loggers deteriorates, impacting the reliability of the measurements.

3.5.5 Sampling and field measurements

During the pilot, water samples were taken. These samples included samples of injected and recovered drinking water, taken at the pumping well, and samples taken at observation wells. At the pumping well, the quality of the injected and extracted water was examined. Samples taken at the observation wells were taken at different filter depths. The samples were analysed at Het Waterlaboratorium (HWL), an external party (Stuyfzand & Borst, 2022).

EC is one of the parameters measured using these samples. The values have been adjusted to 25 °C, and it should be noted that a slight margin is accounted for when interpreting these measurements. The samples are collected at specific time intervals and specific filter depths. For this research, EC measurements taken in filters 2 to 5 of the pumping well and filters 5 to 9 in both observation wells are used. Since not every filter in the wells is equipped with a data logger, these field measurements serve as an additional valuable data source. These measurements can also be found in Appendix F

3.6 Pilot cycles

The ASR cycle consists of four phases: (1) injection, (2) storage, (3) recovery, and (4) rest. For each phase, the processes discussed in Section 2.2, Section 2.3 and Section 2.4 have a different contribution to a reduction in recovery efficiency. Mechanical dispersion is the dominant process during injection and extraction. In contrast, diffusion and buoyancy effects are dominant during the storage and rest phases. As described in Chapter 2, these effects can be reduced by establishing a transition zone that is created during subsequent cycles (Spierenburg & Borst, 2020a).

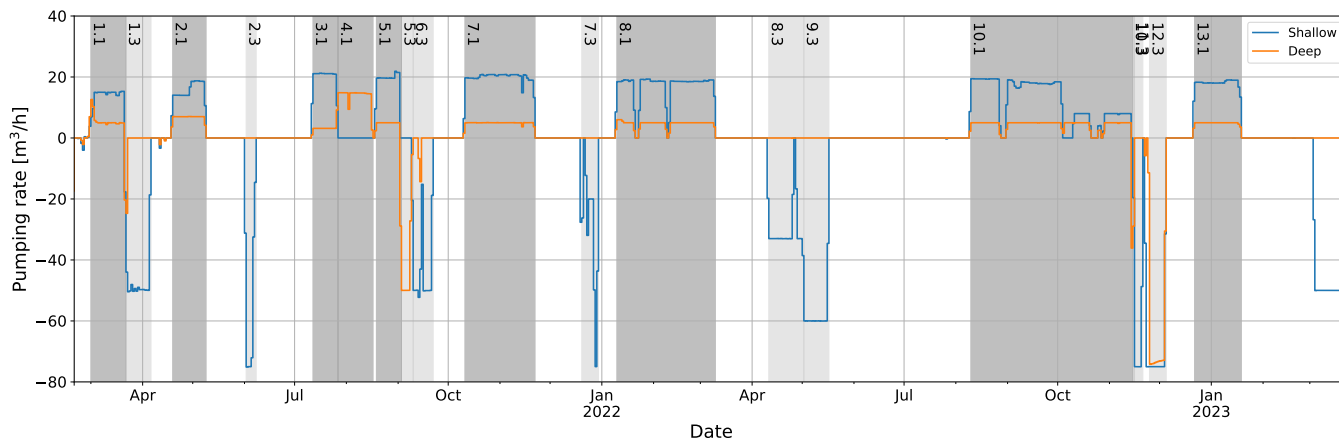


Figure 3.5: Measured pumping rates during different cycles of the ASR system, with injection periods (+) in dark grey and recovery periods (-) in light grey.

During the pilot, PWN conducted multiple cycles with the aim of better understanding the system and ultimately achieving the highest possible recovery efficiency. Figure 3.5 illustrates the cycles performed until March 2023. As depicted in the figure, a mostly constant flow rate is maintained during the injection phase. The shallow well typically injects at rates ranging from 15 m³/h to 20 m³/h, while the deeper well varies between 5 m³/h and 15 m³/h. The main differences observed during the injection phases are time-related. Cycle 4 stands as an exception since only deep injection is performed, which was done to push out the ambient groundwater.

The recovery phases have a shorter duration compared to the injection phases. Additionally, the extraction rates are higher than the injection rates. As mentioned earlier, the deeper well is not utilized during the recovery phase. However, to observe the effects of using this well, it is employed for water extraction in cycle 5. The extraction rates vary between 20 m³/h and 75 m³/h. From cycle 1 to 6, these rates remain constant, but in cycles 7 and 8, they fluctuate within the recovery period. Appendix A provides a table summarising important values regarding the pilot cycles conducted by PWN.

4 Modeling groundwater flow

This Chapter presents the accuracy of a groundwater flow model by testing it against analytical solutions. It starts with an introduction in Section 4.1. It continues with the analytical solutions and radial models in Section 4.2 and Section 4.3. Section 4.4 presents a test case, which is used to examine the performance of the groundwater flow model. Finally, the performance of the model is compared to analytical solutions in Section 4.5.

4.1 Introduction

PWN requires a reliable and efficient ASR system that can be utilised quickly during calamities and handle daily peaks. Additionally, the system should be cost-effective, so entail minimal post-treatment. A maximum of 1% mixing between the injected water and the ambient groundwater is permissible to comply with these criteria. Therefore, assessing the performance of the numerical model is crucial for this study. This requires a accurate flow model, discussed in this chapter, and a reliable transport model, which is discussed in Chapter 5.

Two commonly used numerical models for simulating groundwater flow are SEAWAT and MODFLOW 6, both developed by the United States Geological Survey (USGS). SEAWAT combines the MODFLOW code for groundwater flow with the MT3DMS code for solute transport. This allows SEAWAT to simulate both the interaction of saltwater and freshwater and the dispersion of dissolved substances in groundwater.

A key feature of both numerical models is their modular structure. The model is divided into different modules that model specific aspects of groundwater flow, such as the grid, time, groundwater flow and transport packages, boundary conditions, and other processes. This modular approach enables customisation or addition of specific functionalities. The model uses a cell-centered grid, where the properties and variables of groundwater are assigned to the cells of the grid. In this study, an assessment was conducted to determine which of these numerical models is best suited for the final numerical model for ASR.

It is important to incorporate key processes such as mechanical dispersion, diffusion, retardation, and buoyancy as effectively as possible, to accurately model the separation between injected water and ambient groundwater in the ASR system. Understanding and capturing these processes is a complex task, requiring numerous model calculations and iterations. Given the one-dimensional flow of the pumping well, a radially symmetric model can be employed. The advantage of such a model is significantly reduced computation time compared to a two-dimensional model. In this study, the radially symmetric model developed by Langevin (2008) was chosen. This method offers a straightforward interpretation and allows for the inclusion of stratification, which is prevalent as discussed in Section 3.2. However, a limitation of this method is that it can only accommodate homogeneous layers (Langevin, 2008), meaning that the heterogeneity of the layers described in Section 3.2 cannot be fully accounted for.

In order to ensure the accuracy of the radial model within the strict 1% groundwater mixing boundary, a systematic testing process is necessary. A simple case is employed to achieve this, and the model is compared with analytical solutions. A step-by-step approach is adopted, in which various aquifer properties, such as hydraulic conductivity and storage, are evaluated. The comparison process starts by examining the horizontal hydraulic conductivity, using a one-layered model in a steady state. Then, the model is expanded to a two-layered model with a low permeable layer on top of the aquifer to test the vertical hydraulic conductivity. Finally, a transient solution is studied to assess the storage component. The following sections provide a detailed explanation of both the analytical solutions and the radial model.

4.2 Analytical solutions

4.2.1 Confined flow in steady state

In situations where a pumping well extracts water from a confined aquifer located beneath a thick impermeable layer, the predominant flow within the aquifer is predominantly horizontal. Figure 4.1 shows an example of such a situation, where the pumping well has no influence on the groundwater level at a distance where head is known ($r=r_0$). The steady-state drawdown in this system is described by Thiem's equation (Thiem, 1906) and is used to test the horizontal hydraulic conductivity of the numerical model.

$$h(r) = \frac{Q_w}{2\pi T} \ln\left(\frac{r}{r_0}\right) + h_0 \quad (4.1)$$

$$T = kD \quad (4.2)$$

where $h(r)$ is the head at distance r from the pumping well, Q_0 is the pumping rate, T is the transmissivity of the aquifer, r is the distance to the well, r_0 is the distance where head is known, h_0 is the head at distance r_0 from the pumping well, k is the hydraulic conductivity and D is the aquifer thickness.

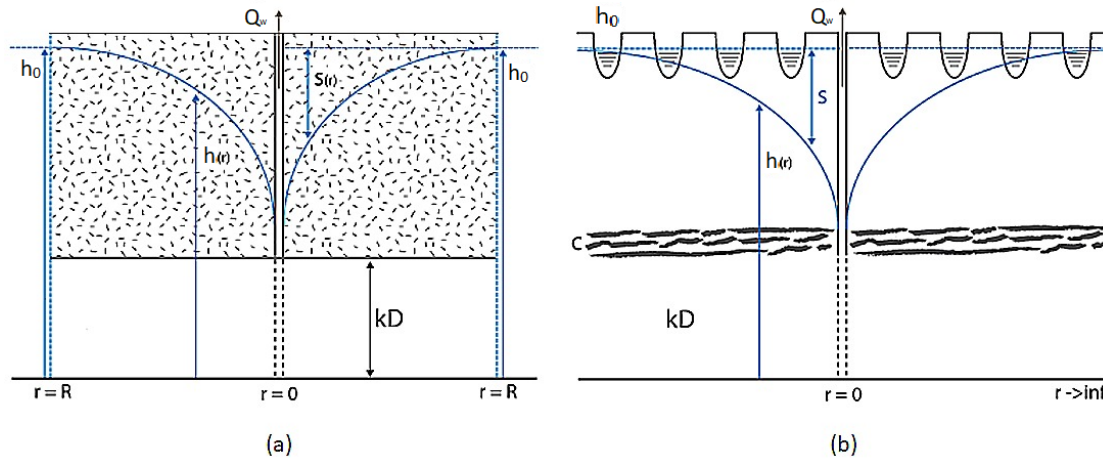


Figure 4.1: Extraction from (a) an aquifer layer beneath a clay layer or (b) an aquifer below a low permeable covering layer (Grondwaterformules, 2023).

4.2.2 Semi confined flow in steady state

When a pumping well extracts water from beneath a (low) permeable layer, groundwater recharge occurs. Figure 4.1 shows this situation. This recharge causes vertical flow, which affects the hydraulic head in the aquifer. This situation is described by de Glee's formula (de Glee, 1930):

$$h(r) = \frac{Q_w}{2\pi T} K_0\left(\frac{r}{\lambda}\right) + h_0 \quad (4.3)$$

where K_0 is the Bessel function (0^{th} order) and λ is the leakage factor given as:

$$\lambda = \sqrt{Tc} \quad (4.4)$$

where c is the resistance of the covering layer. The leakage factor is a measure of how far the impact of a pump's extraction will be noticeable. If the distance between the well and any point of interest is greater than 5 times the leakage factor, then the effects of the extraction on that point will be negligible (Maas & Veling, 2010).

4.2.3 Semi confined transient flow

The system does not immediately reach its steady state. Under the same conditions as described above, reaching this situation depends on the storage in the aquifer. Time-dependent flow is described using the Hantush well function (Hantush & Jacob, 1955), which is used to test storage in the numerical model.

$$h(r) = -\frac{Q_w}{4\pi T} \int_u^\infty \frac{1}{\tau} \exp\left(-\tau - \frac{r^2}{4\lambda^2\tau}\right) d\tau \quad (4.5)$$

where u is defined as:

$$u = \frac{Sr^2}{4T(t-t_0)} \quad (4.6)$$

where S is storage coefficient, t is time and t_0 the initial time.

4.3 Radial model

In this research, the modeling of a groundwater system was done using SEAWAT and MODFLOW 6 software programs, which both use Cartesian coordinates to divide the cells. When there are homogeneous conditions, a pumping well can be thought of as a one-dimensional flow that works radially from the well. It is necessary to convert the Cartesian coordinate system into a radial coordinate system to model this type of flow, as shown in Figure 4.2.

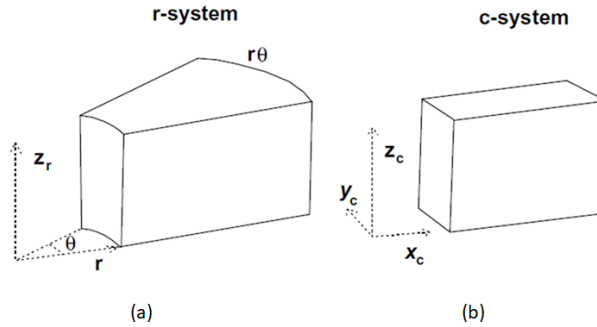


Figure 4.2: Coordinate systems with (a) Cylindrical and (b) Cartesian system (Samani et al., 2004).

With a angle (θ) of 2π , the numerical model is schematised as shown in Figure 4.3. In this system, each cell has an area of a shell times the thickness of that shell. In reality, the model calculates a single row of cells, making this numerical model many times faster than a two-dimensional discretisation. To achieve this in the model, the hydraulic conductivity and specific storage must be adjusted as follows (Langevin, 2008):

$$k_h^* = r\theta k_h \quad (4.7)$$

$$k_v^* = r\theta k_v \quad (4.8)$$

$$S_s^* = r\theta S_s \quad (4.9)$$

where k_h^* is the horizontal hydraulic conductivity in radial coordinates, k_v^* is the vertical hydraulic conductivity in radial coordinates and S_s^* is the specific storage in radial coordinates.

According to Thiem (Equation 4.1), the change in hydraulic head is a function of distance. When $r \rightarrow R$, it holds that $\Delta h \rightarrow 0$, meaning the influence of the pumping well on the hydraulic head is mainly significant in the vicinity of the well. In the numerical model, it is desirable to include small cells around the well to obtain more accurate results around the well. As mentioned, the pumping well has a noticeable effect up to five times the leakage factor of the aquifer, but its influence decreases significantly before that. Since a large number of cells result in longer calculation times, it was decided to increase the cell size further away from the well. This way, the numerical model remains significant around the well, and the calculation time remains sufficiently low.

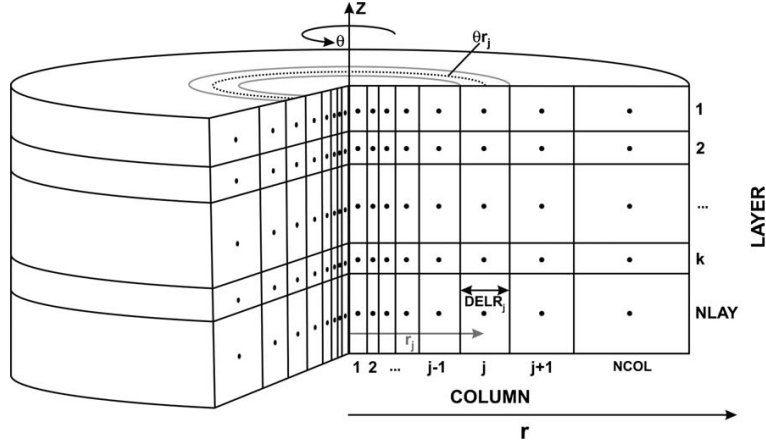


Figure 4.3: Profile of the radial symmetric model (Langevin, 2008).

4.4 Test case

A test case was used to evaluate the numerical models, wherein 30 days of infiltration were followed by 30 days of extraction, as depicted in Figure 4.4, using time steps of 1 d. The flow rate for both processes was set at $500 \text{ m}^3/\text{d}$. The test case represents a complete cycle in which the recovery phase and resting phase are both 0 days. After 60 days, the same amount of water has been infiltrated as extracted, so theoretically it is in balance.

As described in Section 4.1, three methods have been analyzed to test various parameters. Two types of systems were used for this purpose. The first system consists of one layer and the second system consists of two layers. Both systems have an aquifer thickness of 20 m, but the two-layer system has an additional layer on top of it that is 1 m thick with a resistance of 1000 d. The third method is based on the two-layer system and uses a specific storage of 0.005 m^{-1} .

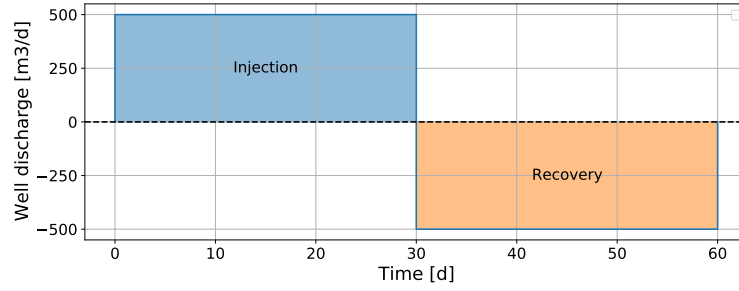


Figure 4.4: Well pumping rates used in the test case.

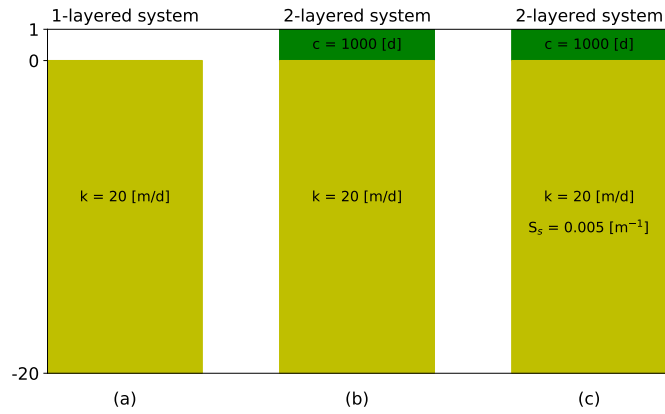


Figure 4.5: Layer layouts used in case (a) confined flow in steady state, (b) semi confined flow in steady state and (c) semi confined transient flow.

Figure 4.5 provides an overview of the layout of the three methods and Table 4.1 shows the cell sizes used for the radial symmetric models.

Table 4.1: Cell sizes of the columns.

From	To	r	Number
[m]	[m]	[m]	[-]
0	60	0.1	600
60	100	1	40
100	150	5	10
150	300	10	15
300	700	20	20
700	2000	50	26
2000	3000	100	10

4.5 Results

4.5.1 Confined flow in steady state

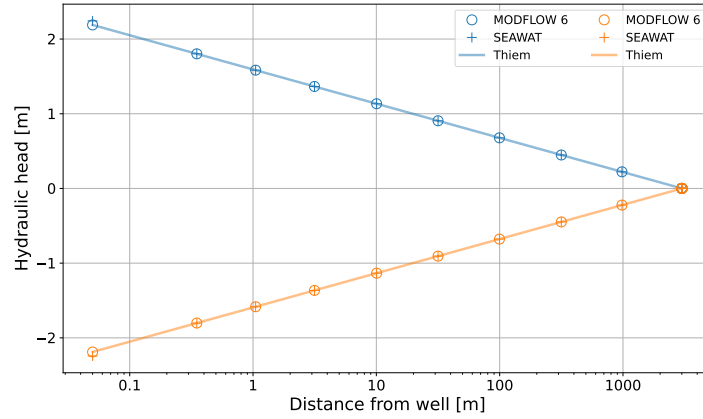


Figure 4.6: The hydraulic heads steady state response for a single-layered confined system during injection (shown in blue) and recovery (shown in orange) as distance increases.

The boundary condition in this scenario is the assumption that the pumping well far away no longer has an influence on the hydraulic head. In the numerical model, this is incorporated by assuming a constant head in the cell farthest away from the pumping well. At the well and sides of each column, there is a no flow boundary. Figure 4.6 shows the result with the analytical solution according to Thiem (Equation 4.1) and the radially symmetric models in SEAWAT and MODFLOW 6, using Equation 4.7. Both models demonstrate that they are accurate enough to model this case with $T = 400 \text{ m}^2/\text{d}$.

4.5.2 Semi confined flow in steady state

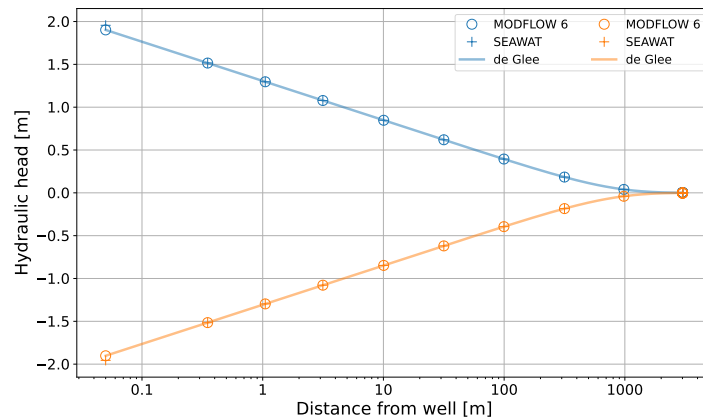


Figure 4.7: The hydraulic heads steady state response for an aquifer that has a permeable layer on top, during injection (represented by blue) and recovery (represented by orange) as the distance increases.

In reality, it is difficult to determine exactly where the aforementioned boundary condition lies. This boundary condition can be replaced by adding a (low) permeable layer above the aquifer. Vertical flow occurs from the (low) permeable layer, which feeds the aquifer. Depending on the resistance of this layer, the thickness of the aquifer, and the hydraulic conductivity, the pumping well has an impact on the hydraulic head. As mentioned in Section 4.2, this influence extends up to 5 times the leakage factor. For this scenario, it is approximately 3000 m, which is how the numerical models have been discretized. The impact of adding the poorly permeable layer is clearly visible in Figure 4.7. Hydraulic head rises more quickly due to vertical groundwater supply. The result also shows that the numerical models accurately reflect the situation with both vertical and horizontal flow.

4.5.3 Semi confined transient flow

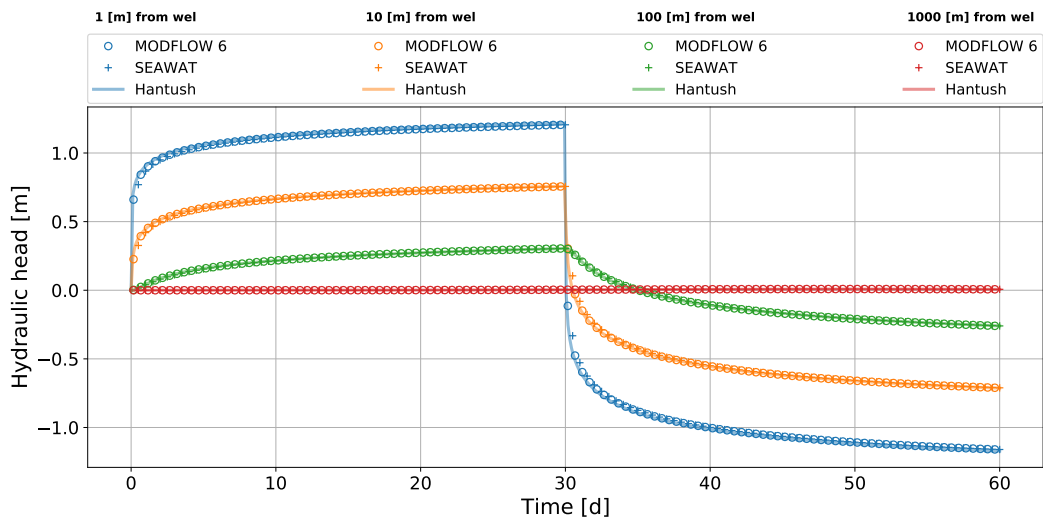


Figure 4.8: *The hydraulic heads variation over time is presented for different distances from the well in an aquifer that has a permeable layer on top.*

After a pumping well is turned on, it may take some time for it to reach steady state. This depends on the storage in the aquifer. A transient solution can be computed by adding this component. Figure 4.8 shows this expansion compared to the analytical method of Hantush (Equation 4.5) in comparison to the steady state numerical model. For different distances, the model shows the ability to calculate the actual hydraulic heads accurately.

5 Modeling transport of heat and solutes in an ASR system

The objective of this chapter is to demonstrate the performance of a radial symmetric model in SEAWAT and MODFLOW 6 to simulate the mixing zone between injected water and ambient groundwater. In Section 5.1 an introduction is given whereafter the method is presented in Section 5.2. The results are presented in Section 5.3.

5.1 Introduction

To model transport of solutes and heat in an ASR system, processes such as flow, dispersive mixing, and density-driven flow described in Chapter 2 are important for this research. These processes operate independently, but can also influence each other. The differential equation that describes heat transport is analogous to the differential equation that describes solute transport. Therefore, to understand the transport model, a general numerical model is tested using the same test case as used in Section 4.4. A distinction between heat and solute transport will be made in Chapter 6.

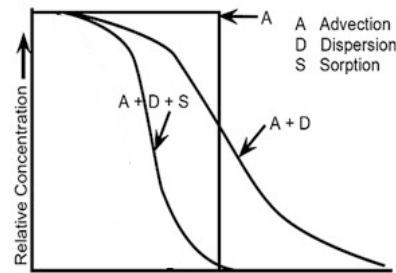


Figure 5.1: *Important processes modeling an ASR (Negm & Eltarabily, 2017)*

Advection describes the transport of water without any mixing or other influences, such as buoyancy. As shown in Figure 5.1, water spreads around the pumping well with a sharp front purely through advection. However, in reality, water undergoes mixing due to processes as dispersion and diffusion, resulting in the formation of a transition zone, as seen in Figure 5.1. Furthermore, the water interacts with both the surrounding groundwater and the soil it flows through, leading to a certain delay in the spreading of the front. This effect is represented as sorption in Figure 5.1. In addition to these processes, buoyancy effects are significant in an ASR system. Since these processes are important in an ASR system, they are evaluated individually in this chapter.

When modeling an ASR system, advection and mechanical dispersion are the most important components during injection and recovery, because they depend on the flow rate in the aquifer. During the storage and resting phase, diffusion and buoyancy will be most noticeable. This mainly occurs at the boundary between the injected water and groundwater.

5.2 Method

Modelling transport of solutes and heat in Modflow 6 and SEAWAT has already been tested for various situations in the past (Langevin, Provost, Panday, & Hughes, 2022b). Therefore, it is reasonable to assume that numerical models are accurate enough. However, this study uses a radially symmetric model, the performance of which still needs to be tested. This has

been done based on a comparison with a two-dimensional model. The two-dimensional model consists of 305 columns and 305 rows, with cell sizes shown in Table 5.1. The pumping well is located in the first cell ($x=0$, $y=0$). For testing the groundwater transport model, the same pumping schedule as described in Section 4.4 was used. To assess the functioning of the various components, a single-layer system is considered (Figure 4.5 (a)). In this process, the change over time is important and therefore a transient model is performed.

Table 5.1: Cell sizes used for the two-dimensional model.

From	To	$\Delta x = \Delta y$	Number
[m]	[m]	[m]	[-]
0	100	1	100
100	150	1	50
150	300	5	30
300	700	10	40
700	2000	20	65
2000	3000	50	20

For the radial symmetrical model the porosity (η) is adjusted according to the method described by Langevin (2008) with the angle (θ) and distance to the pumpin well (r):

$$\eta^* = r\theta\eta \quad (5.1)$$

After adjusting the porosity, advection was added to the model. For SEAWAT, the Hybrid Method of Characteristics (HMOC) was used, which combines the forward and backward methods of characteristics. This method is a particle based, numerical technique for solving partial differential equations in physical problems (Axelsson & Marinova, 2014). In Modflow 6, this method is currently not available and therefore the Total Variation Diminishing (TVD) method was used instead. This method is implicit and since the problem is dominated by advection, needs a finer discretization (Langevin et al., 2022b). Because advection is one of the most important processes in modeling an ASR system, it is also tested based on an analytical solution. This is based on the fact that during injection and extraction, under pure advection, the injected water grows and shrinks like a cylinder. The injected water is present in the pores and is calculated using a mass balance:

$$V_w = V_p = Q_w t \quad (5.2)$$

where V_w is the volume of injected water, V_p is the pore volume, Q_w is the pumping rate and t is the time. The pore volume however is part of the total volume which is computed by:

$$V_t = \frac{V_p}{\eta} \quad (5.3)$$

where V_t is the total volume and η is the porosity of the aquifer. By using the total volume and the geometry of a cylinder, the distance of the water reach can be computed with Equation 5.4 and Equation 5.5.

$$A = \frac{V_{total}}{H} \quad (5.4)$$

$$r = \sqrt{\frac{A}{\pi}} \quad (5.5)$$

Following the assessment of advection, the model incorporates hydrodynamic dispersion (Equation 2.1) in two steps. The first step involves mechanical mixing, assuming one-dimensional flow where the longitudinal and transverse dispersivity coefficients are equal. The second step involves examining diffusion by introducing a diffusion coefficient.

In the groundwater models, sorption refers to adsorption/desorption of solutes into/from solid surfaces in the aquifer. This process can affect the transport of contaminants by altering their movement and potentially retarding their migration through the subsurface. In this research it is used to quantify the retardation (R), which it is commonly associated with. This process depends on the porosity (η), bulk density ρ_b (a measure of how closely packed the individual particles of a material are within a given volume) and an adsorption coefficient K_d (a measure of how solutes or heat are adsorbed by the soil):

$$R = 1 + \frac{\rho_b K_d}{\eta} \quad (5.6)$$

For the radial model, the bulk density requires adjustment (Langevin, 2008), which is performed as follows:

$$\rho_b^* = r\theta\rho_b \quad (5.7)$$

where ρ_b is the bulk density of the solid.

Lastly, buoyancy is also examined, which is another significant process in an ASR system. However, testing buoyancy requires a different approach than the other transport mechanisms. Instead of the extraction period, a storage phase is used. Moreover, it is necessary to divide the aquifer into multiple layers. In this case, the layer shown in Figure 4.5 (a) is divided into three equal layers.

5.3 Results

5.3.1 Advection

The results of the models run with only advection are shown in Figure 5.2. This shows the situation for four different time steps, with the top two graphs during injection and the bottom two during extraction. For both the SEAWAT and MODFLOW 6 models, the radially symmetric model corresponds to the 2D model. For three out of four moments, the SEAWAT model is very accurate compared to the analytical solution. However, this is not the case for the MODFLOW 6 model. In this model, the median (e.g., 0.5 concentration) appears to match the analytical solution well, but the concentration spreads over an increasing number of cells and therefore a greater distance over time. This is a result of limitations of the TVD solver in the model and has a similar effect as hydrodynamic dispersion. This error is called numerical dispersion, and in advection-dominated problems, it becomes a serious problem because these problems have a sharp concentration front (Zheng & Wang, 1999). In an ASR system, advection is of great importance, which is why numerical dispersion is further studied in Section 5.3.3.

5.3.2 Dispersion

As the hydrodynamic dispersion increases (Equation 2.1), it means that the concentration spread becomes larger. Mechanical dispersion plays a role in this process, which depends on the water flow velocity (v) and a dispersivity coefficient (α). Additionally, diffusion (D_f) takes place. This is the process in which mixing occurs between injected water and groundwater, independent of the water flow velocity. Figure 5.3 shows the result for a situation with a dispersivity coefficient

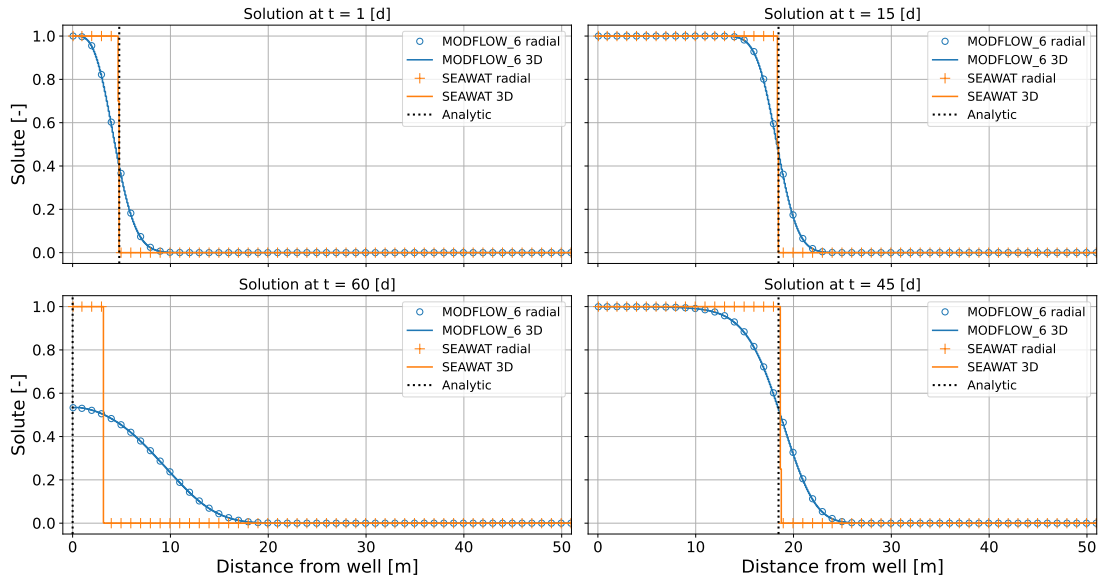


Figure 5.2: Results of models to simulate advection in an ASR cycle with a porosity of 0.35.

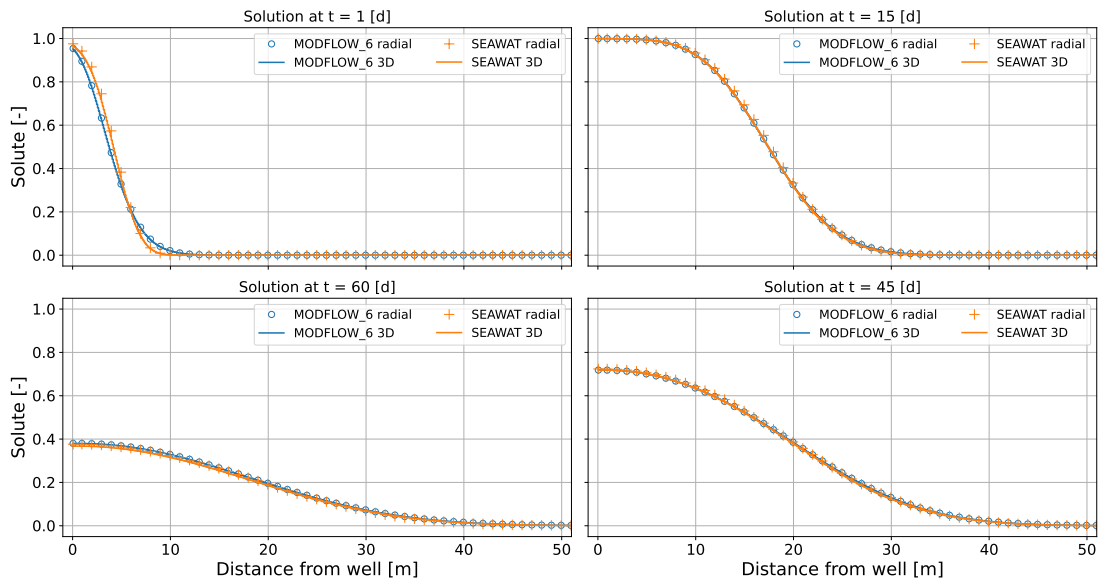


Figure 5.3: Results of models to simulate advection and dispersion ($\alpha=1$ m, $D_f=1$ m²/d) in an ASR cycle.

of 1 m and a diffusion coefficient of 1 m²/d. The radially symmetric models closely match the 2D models. In this analysis, multiple coefficients were used to map the effect of dispersion. It is evident that as the coefficients increase, the MODFLOW 6 models tend to converge towards the SEAWAT solution. This is due to the numerical dispersion in the MODFLOW 6 result, which decreases as dispersion dominates more (Zheng & Wang, 1999). The following section will delve

further into this topic.

5.3.3 Numerical Dispersion

This section further discusses the numerical dispersion that occurs in a MODFLOW 6 model with advection only (Section 5.3.1). To quantify the error of numerical dispersion, the deviation of the MODFLOW 6 model is examined based on the Gaussian cumulative density function (Dekking et al., 2005):

$$f(x) = \frac{1}{\sigma\sqrt{2\pi}} e^{-\frac{1}{2}\left(\frac{x-\mu}{\sigma}\right)^2} \quad (5.8)$$

$$F(x) = \int_{-\infty}^x f(t) dt \quad (5.9)$$

where μ is the mean of the distribution representing the central value around which the solute concentration is symmetrically distributed and σ is the standard deviation, which is a measure of the spread of the concentration quantifying the deviation from the mean.

Figure 5.4 shows the results of this analysis. For three different time steps, model results and their corresponding Gaussian functions are shown during injection (top left figure) and recovery (bottom left figure).

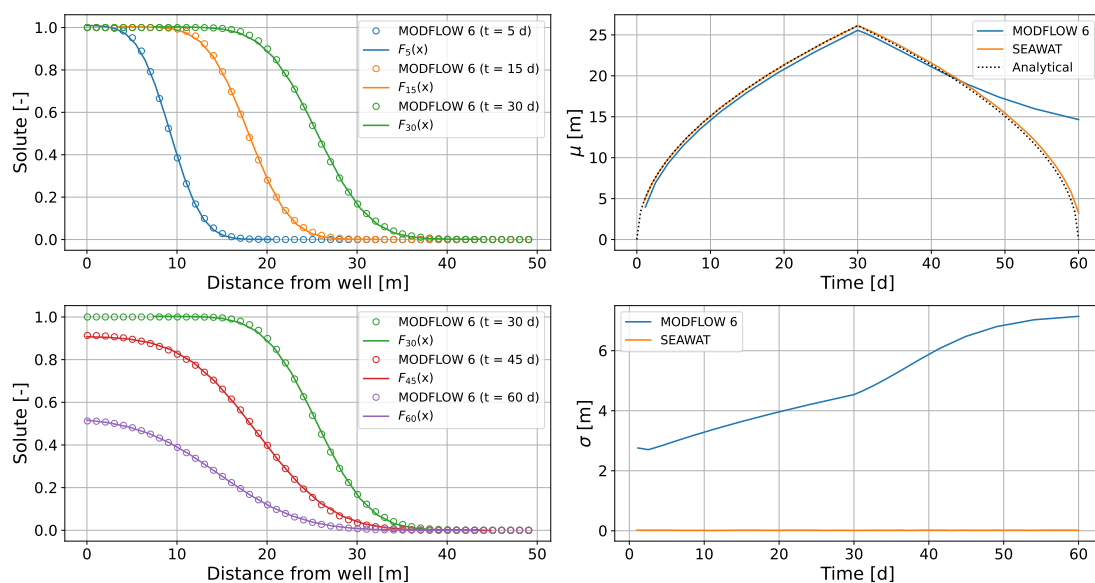


Figure 5.4: Development of numerical dispersion during injection (top left), recovery (bottom left). The average distance (top right) and standard deviation (bottom right) based on Gaussian analysis.

As described in Section 5.2, the injected and extracted water behaves like a cylinder (i.e., sharp front) when only advection is considered. This sharp front, calculated using Equation 5.5, is compared to the mean value of the model results (top right figure). During injection, they are comparable, but during recovery, the model deviates significantly after 45 d.

The influence of extraction is also evident when comparing time steps of 15 days and 45 days. In both cases, there is 7500 m³ of drinking water in the aquifer. Using the analytical solution

(Equation 5.5), the sharp concentration front would be around 18.5 m from the pumping well. The difference in variation indicates that extraction further increases the growth of numerical dispersion. This visual observation is further confirmed when the standard deviation is calculated for each time step in the test cycle using Equations 5.8 and 5.9. The bottom right figure shows that the standard deviation increases significantly over time.

As a result of numerical dispersion, the MODFLOW 6 model exhibits a significant average deviation and significant standard deviation after completing a cycle. In this analysis, it is also apparent that the SEAWAT model is very accurate. The deviation at the 60-day time step in Figure 5.2 is simply a matter of one time step.

As advection becomes less dominant, the numerical dispersion decreases. Since advection plays a crucial role in an ASR system, it is essential to determine when the influence of numerical dispersion decreases. To investigate this, the study compares the numerical dispersion in MODFLOW 6 to the dispersion in SEAWAT, which can simulate sharp fronts. The analysis indicates that a dispersivity value of approximately 0.2 m in SEAWAT corresponds to the numerical dispersion in MODFLOW 6, as shown in Figure 5.5. Therefore, if the actual dispersivity is higher than 0.2 m, MODFLOW 6 can be used. To account for numerical dispersion, it needs to be subtracted from the dispersion in the MODFLOW 6 model. However, it is worth noting that as advection becomes less dominant, the role of numerical dispersion also diminishes. This trend can be observed in Figure 5.3, where both MODFLOW 6 and SEAWAT yield similar results for a dispersivity value of 1 m.

It is important to mention that the analysis considered different flow rates that are reasonable for this research. Additionally, the influence of cell size on numerical dispersion was examined and found to have no significant impact. The complete analysis can be found in Appendix B.

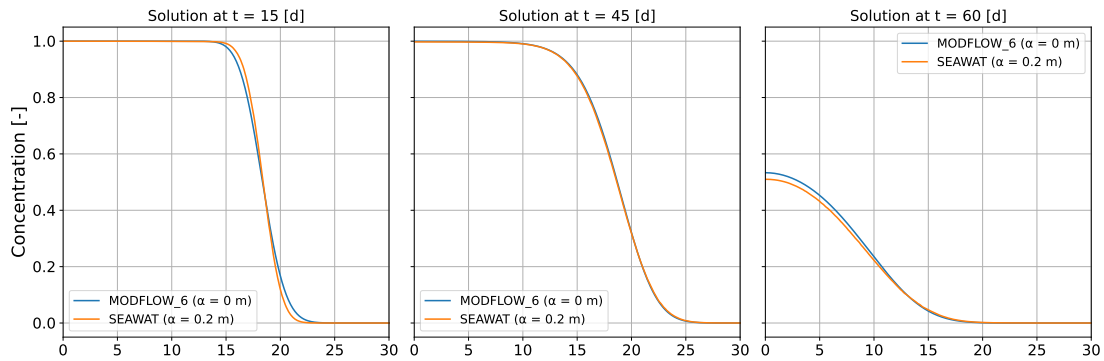


Figure 5.5: Comparison between a MODFLOW model with only advection and its associated numerical dispersion and a SEAWAT model with dispersion.

5.3.4 Sorption

As mentioned earlier, sorption is used to model retardation. When this process is added to the model along with advection and dispersion (Figure 5.3), you can observe the retardation particularly in the result after 15 d (Figure 5.6 top right). Without retardation, the injected water reaches approximately 30 m, whereas with retardation, it only reaches around 25 m. Both the SEAWAT model and the MODFLOW 6 model yield the same result, indicating their performance.

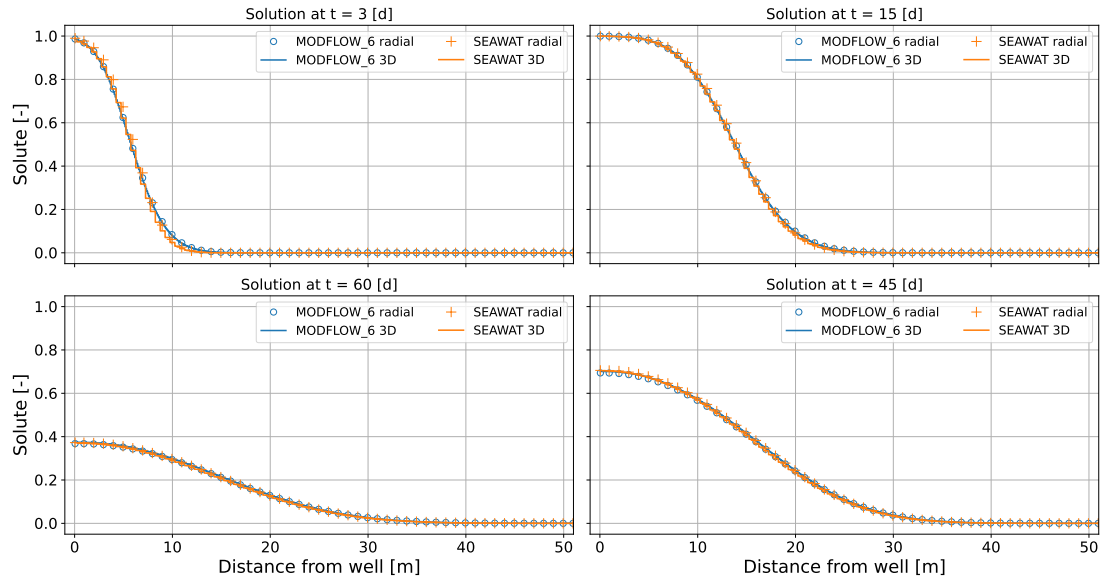


Figure 5.6: Results of models to simulate advection, dispersion ($\alpha = 1$ m, $D_f = 1$ m²/d) and sorption in an ASR cycle.

5.3.5 Buoyancy

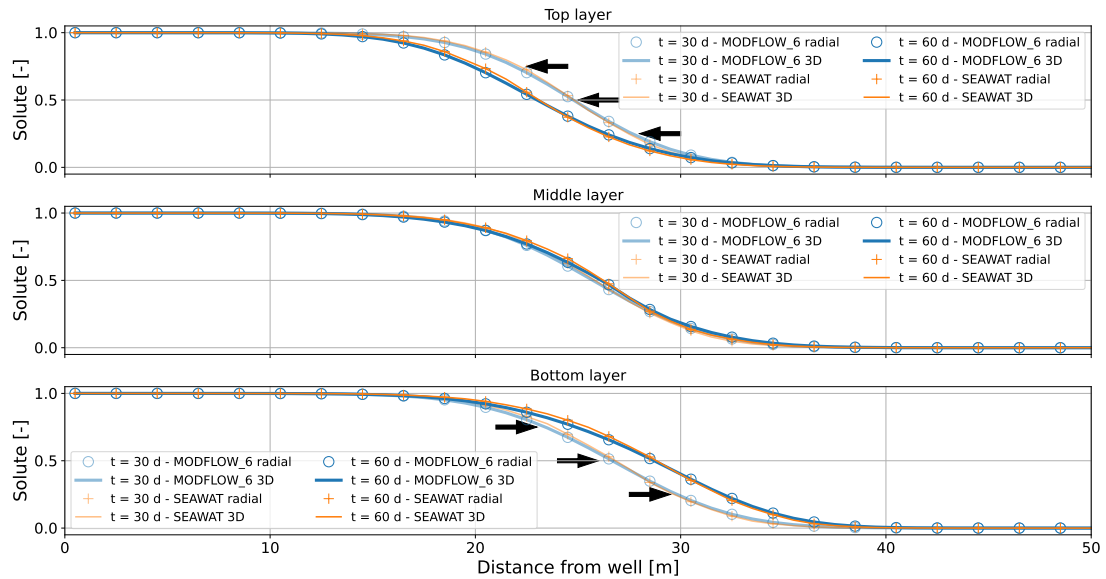


Figure 5.7: Concentration front in the upper layer of the aquifer, the middle of the aquifer, and the lower layer of the aquifer after injection (30 d) and at the end of the subsequent storage phase (60 d). The buoyancy effects are depicted with arrows.

For this analysis, the 20 m aquifer was divided into three equal parts (upper, middle, lower). In Figure 5.7, the concentration front is shown in each layer after 30 days of infiltration and an additional 30-day storage phase. In this case, the injected water is denser and sinks below the lighter ambient groundwater. This can be observed in the figure with the shifting of the front, where it flows away from the well in the deep part and towards the well in the shallow part, as indicated by the arrows. Both radial models correspond with the 2D models.

5.3.6 Computation times

When designing a model, there is always a trade-off between computation time and the level of detail in the model. Even in a relatively simple models, such as the one used in this section, there are significant differences in computation times. Computation times for radially symmetrical models range from seconds (in MODFLOW 6) to a few minutes (in SEAWAT). For 2D models, there is greater variation, with computation times in MODFLOW 6 ranging from five to ten minutes, but in SEAWAT, they can take a few hours. These differences are primarily due to the chosen solution methods, as described in Section 5.2. Because advection is an important process in an ASR system and a radially symmetrical model in SEAWAT provides fairly accurate results, it is used to for the simulations in Chapter 6.

6 Modeling the ASR system in Hoorn

This chapter discusses the final numerical model for the ASR system in Hoorn. This model was developed based on insights gained from previous chapters and comparisons with measurements. The methodology used for this purpose is described in Section 6.1. Subsequently, the model is presented in Section 6.2. Finally, in Section 6.3, the performance of the model is discussed, including a critical examination of discrepancies between the model and measurements.

6.1 Method

A radial symmetric model was used to simulate ASR in Hoorn. The initial numerical model is based on properties described in Section 3.2, Section 3.3, and Section 3.4. The model was then improved by comparing it with relevant hydraulic head measurements, temperature measurements, and EC measurements, as described in Section 3.5. In the improvement process, the model progressed from coarse estimation to increasingly fine estimation. This section further explains this progression.

6.1.1 Estimation of the horizontal hydraulic conductivity

The most important factors for the hydraulic heads are the pumping rates and hydraulic conductivity in the aquifer. Both factors influence the hydraulic heads in the aquifer. These heads have been measured at various depths in the soil using data loggers (see Table 3.3). For the horizontal hydraulic conductivity, the values from Table 3.1 were initially assumed. Using the hydraulic head measurements, an improved estimation of the horizontal hydraulic conductivity within the aquifer and the resistance of clay layers was obtained. Sand layers in the soil were divided into intervals between the loggers, where the soil composition, as described in Section 3.2, has also been taken into account as accurately as possible.

Different values for the parameters were iteratively tested for each of these layers to approximate the measurements.

6.1.2 Estimation of the retardation in heat transport

Through continuous measurements of temperature with DTS (over time and depth, see Section 3.5.2), it is possible to compare temperature measurements with the numerical model at the same depths as the hydraulic heads. As described in Section 3.5.4, continuous logger measurements were also taken at various depths. The determination of retardation is based on the distribution coefficient (K_d). Initially, a distribution coefficient of $2.4 \cdot 10^{-4} \text{ m}^3/\text{kg}$ was assumed for heat transport (Tombe, 2016). The heat transport breakthroughs were compared, which led to an estimation of the retardation of heat transport (Equation 5.6), but also verification of the estimated hydraulic conductivities. Both, hydraulic conductivities and retardation affect the arrival times of heat and the rate at which heat travels.

6.1.3 Refining horizontal hydraulic conductivity and heat retardation

After the estimation of the horizontal hydraulic conductivity and retardation, a finer estimation was made based on temperature profiles. In this process, the continuous measurements with DTS were compared to the model results. Instead of using coarse layers between the loggers, smaller layers of approximately 0.3 m to 2 m thickness were used around the pumping zone. Since DTS measures at every meter depth, a deviation of 3 m depth in the comparison between measurements and model results are acceptable.

6.1.4 Estimation of the porosity

The initial assumption for the porosity in the soil were a value of 0.35 for sand and a porosity of 0.2 for clay. The porosity affects the flow velocity at which the water flows as described by the following formulas:

$$v_r = \frac{q_r}{\eta} \qquad v_z = \frac{q_z}{\eta} \qquad (6.1)$$

where v_r is flow velocity of the water in radial direction, v_z is flow velocity of the water in depth direction, q_r is specific discharge in radial direction, q_z is specific discharge in depth direction, η is the porosity. Based on logger measurements at different filter depths, as described in Section 3.5.4, adjustments in porosity are made to improve the performance of the model. The outcomes of this model were further compared with borehole logging measurements (Section 3.5.3) to assess the overall agreement between the numerical model and these measurements.

6.1.5 Estimation of the buoyancy

The numerical model calculates density differences based on the salinity using a conversion factor. Standard values according to Langevin et al. (2008) are used for this purpose. From the comparison with borehole logging measurements, it is observed that buoyancy plays a significant role in the deep aquifer. To account for this, an attempt was made to enhance buoyancy by reducing the difference between horizontal and vertical hydraulic conductivity at these depths.

6.1.6 Estimation of dispersion

Dispersion occurs at the boundary between the injected water and ambient groundwater, and simulating it accurately requires measurements at the interface between the infiltrated water and ambient groundwater. Since the observation wells may not necessarily be located around the interface, accurately mapping it becomes challenging. Therefore, an estimation is made for dispersion, considering a single value for the entire depth range. As mentioned in Section 2.3, dispersion decreases after several cycles, playing a lesser role in an ASR system.

6.2 Model design

6.2.1 Discretization

The model consists of 101 layers, 1 row, and 121 columns. The row has a width of 1 m, and the ground level is at -1.55 mNAP. Table 6.1 provides an overview of the cell sizes. The model starts at 2021-02-19 and ends on 2023-03-24, with time steps of 1 day, corresponding to the data described in Section 3.6.

Table 6.1: Cell sizes of the columns (left) and layers (right).

From	To	r	Number	From	To	z	Number
[m]	[m]	[m]	[-]	[mNAP]	[mNAP]	[m]	[-]
0	100	1	100	-1.55	-120	0.3 - 2	78
100	200	10	10	-120	-160	5	8
200	500	50	6	-160	-260	10	10
500	1000	100	5	-260	-284	1.8 - 8	5

6.2.2 Aquifer properties

Initially, ten different layers were considered based on Table 3.1, each with an initial estimate of hydraulic conductivity. Porosity was differentiated only between sand and clay, and a single value was assumed for the adsorption coefficient. The initial situation is depicted on the left side of Figure 6.1.

Based on the method described in Section 6.1, the porosity (η), horizontal hydraulic conductivity (k_h), vertical hydraulic conductivity (k_v) and adsorption coefficient for heat transport (K_d) were iteratively estimated. Appendix G demonstrates this iterative process. The analysis has led to the differentiation of 19 layers, involving adjustments of 16 values for hydraulic conductivity, 7 values for the adsorption coefficient in heat transport, and 5 values for porosity compared to the initial estimates. In the middle of Figure 6.1, the parameters that have been adjusted from the initially assumed values are displayed. The resulting values from these analyses are shown in Table 6.2. This table also indicates the soil types, with sand layers displayed in yellow and clay layers in green. Additionally, the initial values for EC and temperature over depth are provided in the table.

The layered system can be explained based on the borehole drillings described in Figure 3.2. The right hand side of Figure 6.1 illustrates how they overlap with each other. A strong resemblance is observed between the various layers from the analysis and these borehole descriptions together.

Table 6.2: *Aquifer properties over depth, including the initial conditions for EC and temperature.*

Top	Bot		η	k_h	k_v	EC	K_d	T
[mNAP]	[mNAP]		[-]	[m/d]	[m/d]	[mS/cm]	[m ³ /kg]	[°C]
-1.55	-21.75		0.20	0.01	0.001	1.25	2.40E-04	9.80
-21.75	-30.23		0.35	30	15	1.25	2.40E-04	10.70
-30.23	-36.03		0.35	15	7.5	1.25	2.40E-04	10.60
-36.03	-49.15		0.35	25	12.5	1.25	2.40E-04	10.60
-49.15	-50.65		0.20	1	1	1.25	2.40E-04	10.50
-50.65	-58.65		0.40	70	35	1.38	1.90E-04	10.50
-58.65	-64.65		0.35	90	45	1.38	2.40E-04	10.60
-64.65	-78.65		0.40	70	35	1.98	2.40E-04	10.60
-78.65	-82.66		0.35	60	30	3.38	1.90E-04	10.70
-82.66	-85.89		0.40	60	30	3.38	1.90E-04	10.70
-85.89	-87.89		0.20	0.2	0.2	3.40	2.40E-04	10.80
-87.89	-89.89		0.35	30	15	3.40	2.40E-04	10.80
-89.89	-90.89		0.20	0.02	0.02	4.40	2.40E-04	10.80
-90.89	-97.89		0.40	30	30	5.40	2.40E-04	10.90
-97.89	-101.89		0.30	90	90	6.90	1.90E-04	11.00
-101.89	-103.89		0.35	70	70	7.70	2.40E-04	11.00
-103.89	-104.89		0.35	20	20	8.10	2.90E-04	11.00
-104.89	-105.89		0.20	0.1	0.1	8.50	2.40E-04	11.00
-105.89	-261.99		0.35	60	60	17.80	2.40E-04	11.00
-261.99	-283.82		0.20	0.001	0.001	28.75	2.40E-04	11.00

In terms of dispersivity, SEAWAT only allows for a single coefficient that applies to both solute and heat transport. The same dispersivity value was used for both types of transport. According to the report by Zuurbier et al. (2018), a dispersivity of 0.1 m is considered representative. Additionally, this report recommends specific storage coefficients of 10^{-8} m^{-1} for sand and 10^{-3} m^{-1} for clay. SEAWAT does offer the ability to differentiate diffusion. In this study, the diffusion coefficient is set to $0.143 \text{ m}^2/\text{d}$ for heat transport (Tombe, 2016) and $8.64\text{E-}5 \text{ m}^2/\text{d}$ for solute transport (Pauw et al., 2015).

The consideration of buoyancy and viscosity is based on standard values provided by Langevin et al. (2008). Within the model, densities are calculated based on EC concentrations, and the viscosity is internally calculated based on temperature (Langevin et al., 2008).

6.2.3 Model features

All cycles described in Section 3.6 are incorporated into the model. The pumping rates are distributed among the layers in which they operate based on the thickness and hydraulic conductivity of each layer. The initial temperature and EC concentrations from Table 6.2 are used as boundary conditions in the model.

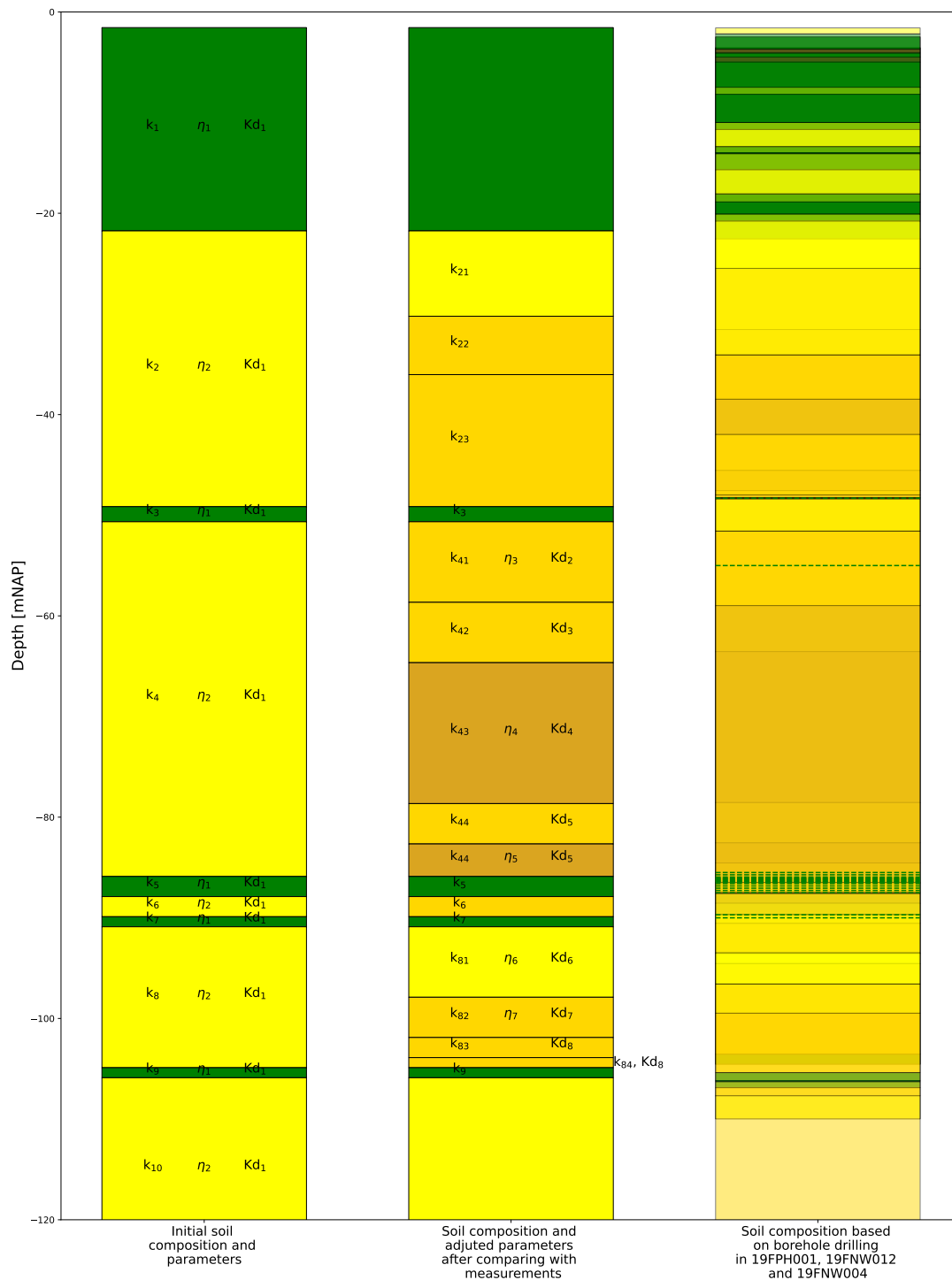


Figure 6.1: Initial soil composition and parameters (left), final estimated soil composition and adjusted parameters (hydraulic conductivity (k), porosity (η) and adsorption coefficient for heat transport (K_d)) in the middle and an overlap of the borehole drillings 19FPH001, 19FNW012 and 19FNW004 on the right.

6.3 Results

6.3.1 Hydraulic head change

As described in Section 6.1, measurements of hydraulic head were used to estimate the hydraulic conductivity. Figure 6.2 presents the final results for two filter depths (2 and 7) in observation wells 19FNW012 (8.3 m distance from the ASR well) and 19FNW004 (12.3 m distance from the ASR well). The measurements have an accuracy margin of 5 cm. The figure indicates injection periods in dark gray and recovery periods in light gray, along with their corresponding cycle numbers and phases (as described in Section 3.6).

At a depth around -17 mNAP, no pumping occurs, but the influence of the ASR system is still noticeable. However, the hydraulic head changes less rapidly compared to the aquifer where pumping takes place, such as at a depth of -74 mNAP. The model aligns well with the measurements, indicating that groundwater flow is reasonably represented. The complete results with hydraulic heads for filters 2 to 9 can be found in Appendix D.

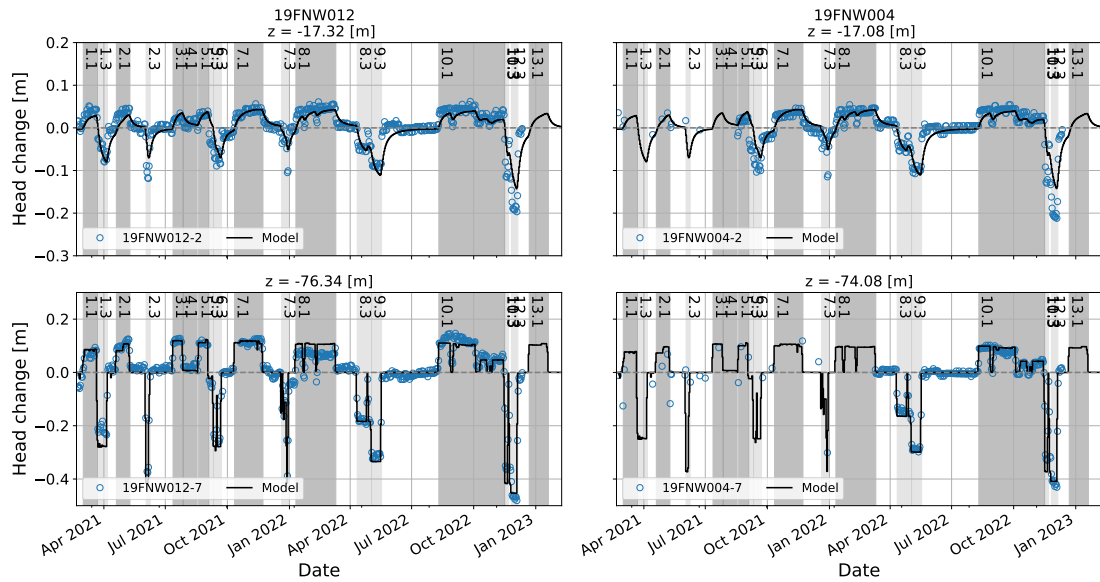


Figure 6.2: The changes of hydraulic head measured in filters 2 and 7 of observation wells 19FNW012 and 19FNW004 is depicted with model results. The injection periods are indicated in dark gray, while the recovery periods are shown in light gray, along with their corresponding cycle and phase numbers.

6.3.2 Heat transport

Multiple filters are present in both the pumping well (19FNPHO01) and the observation wells within the aquifer, measuring at approximately six different depths. Not every depth has a CTD or TD logger measuring temperatures. However, DTS measurements are available at each of these depths. Both kinds of measurements were used to make an initial estimation of retardation. Figure 6.3 shows the results for depths around -64 mNAP and -97 mNAP. The former represents the result of the pump that operates in the shallow part of the aquifer, while the latter represents the pump that operates at the deeper part of the aquifer. Periods of injecting cold water (i.e., colder than the natural groundwater temperature) are shown in blue, while periods of injecting warm water (i.e., warmer than the natural groundwater temperature) are shown in red, with their respective cycle and phase numbers. Again, the light gray areas represent the recovery periods. The complete results can be seen in Appendix E

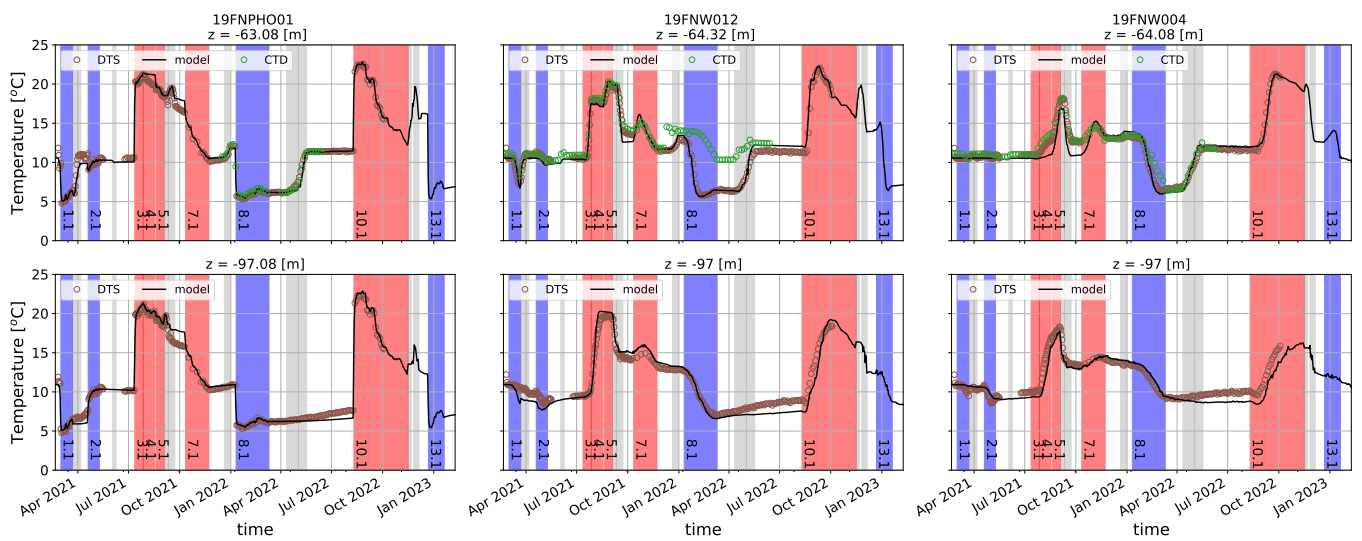


Figure 6.3: Changes in temperature during the pilot in the pumping well (19FNPHO01) and two observation wells (19FNW012 and 19FNW004) at two different depths are depicted. Periods shown in blue indicate when cold water is injected, periods in red indicate the injection of warm water, and the light gray areas represent the recovery periods.

The model closely matches both types of measurements, with a few exceptions. At depths around -87 mNAP and -97 mNAP, as well as specifically in observation well 19FNW012 at -64 mNAP, there are deviations. The first exception is related to clay layers at the same depth, which will be further discussed in Section 7.2. At -97 mNAP, the model agrees with the DTS measurements until after the injection period of cycle 8. After that, pumping ceases in this part of the aquifer, yet the temperature continues to rise according to the DTS measurements. This can also be observed at a depth around -104 mNAP, where the model aligns with the measurements. This discrepancy suggests that the water between these layers may be saltier than initially assumed, amplifying buoyancy effects. Another possibility is that dispersion at this depth is higher, which would also lead to a flattening of the peaks observed in the model.

A specific deviation is observed at -64 mNAP in observation well 19FNW012. After the injection period in cycle 7 (7.1), the CTD measurements deviate from both the model and the DTS measurements. Notably, there is a temperature jump of approximately 3 °C during a

period when pumping is not taking place. These are typical issues that can occur in this type of measurement. It is plausible that during this period, the diver was removed from the observation well for data retrieval but was not repositioned at the correct depth, resulting in a temperature jump.

After this analysis, the model was compared with the DTS measurements taken throughout the entire depths of the pumping well and two observation wells. This allowed for a more accurate estimation of the retardation and small differences in horizontal hydraulic conductivities. Figure 6.4 presents the model's results for four different dates, along with the corresponding DTS measurements. It is important to note that the entire tubing in the pumping well is affected by water flow during pumping. The left side of the figures illustrates the subsurface profile, with yellow representing sand and green representing clay. Additionally, the locations of both filters in the pumping well are indicated, and the arrows provide an indication of pumping activity.

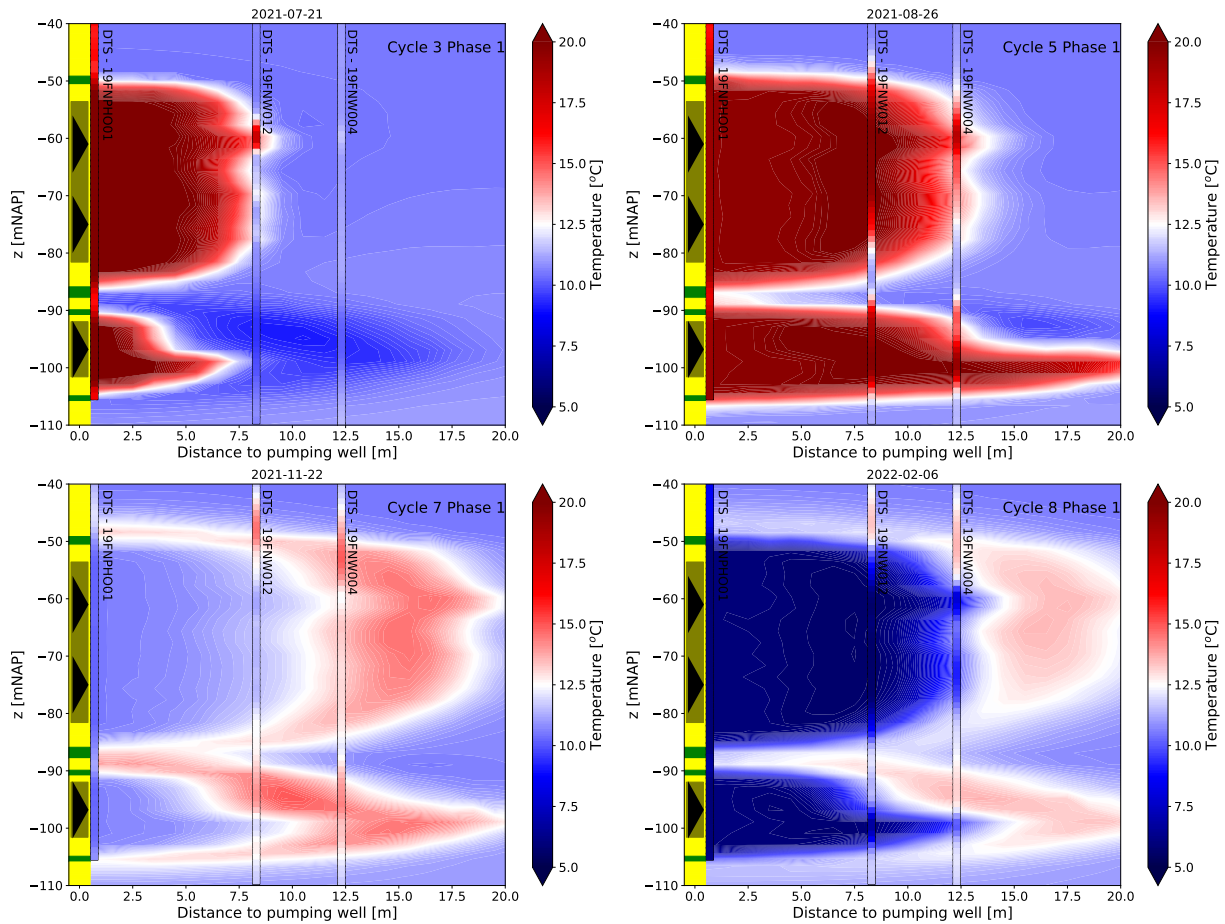


Figure 6.4: The contour plot illustrates the model's results and DTS measurements for four different dates, depicting the distribution of subsurface temperatures. The left side of the figures shows the geologic profile, with sand depicted in yellow and clay in green. The positions of the filters in the pumping well are marked, and the arrows indicate pumping activities.

The arrival of the injected water in the shallow part of the aquifer (e.g., -50 mNAP to -85 mNAP) is clearly visible in the top two figures of Figure 6.4. The lower two figures depict the arrival of the injected water in the deep part of the aquifer (e.g., -90 mNAP to -105 mNAP). In both cases, the left figure indicates the arrival at observation well 19FNW012, while the right figure represents the arrival at observation well 19FNW004. Two notable depths are around -60 mNAP and -100 mNAP, where the water flows noticeably faster compared to other depths. Additionally, the injected water just above the clay layer at -85 mNAP is slightly lifted. This effect is a combination of increased resistance from this layer, causing slower movement of injected water, and buoyancy effects.

The lower figures in Figure 6.4 also show the effect of dispersion. The model seems to capture this effect quite well, validating the assumption of homogeneous dispersion. However, there are still some local differences observed. For instance, in the lower two figures, it is noticeable that the dispersion around -50 mNAP is lower than initially assumed.

6.3.3 Solute transport

The following step involved examining the porosity by comparing the model with EC measurements. This comparison was based on measurements taken with CTD loggers and field measurements conducted by HWL in the pumping well and observation wells 19FNW012 and 19FNW004. These measurements were taken at various filter depths. It should be noted that not every filter depth had a diver installed. Figure 6.5 illustrates these measurements along with the model results at depths around -64 mNAP and -104 mNAP. Dark gray areas indicate injection periods, while light gray areas represent recovery periods. The results for all depths are presented in Appendix F.

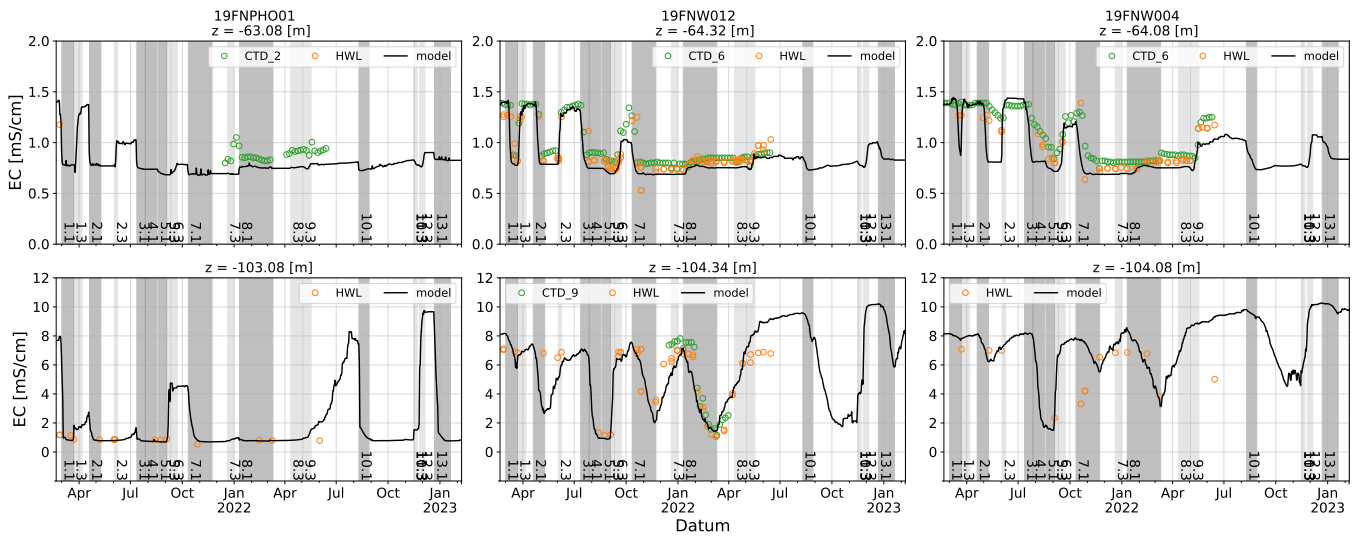


Figure 6.5: Changes in EC during the pilot in the two observation wells (19FNW012 and 19FNW004) at two different depths are depicted. Periods shown in dark gray indicate when water is injected and the light gray areas represent the recovery periods.

The model agrees well with both measurements, except at a depth of -87 mNAP. As mentioned earlier, this is due to the presence of clay layers around this depth, which will be further discussed in Section 7.2. Buoyancy effects are clearly visible during periods without pumping activities around a depth of -75 mNAP and -104 mNAP. The water in these areas becomes saltier than the initial values after the recovery of cycle 9 (9.3). This saline water comes from deeper layers where the ambient groundwater is saltier.

Small differences between the limits of EC values can be due to the temperature correction of EC. Both types of measurements are corrected to 25°C, whereas the EC values used in the model are corrected to 20°C, as mentioned in Sections 3.5.4, 3.5.5 and 3.5.1.

Local differences between measurements and the model also exist. At a depth of -64 mNAP in observation well 19FNW004, the injected water arrives earlier in the first 5 cycles according to the model, whereas the measurements show agreement in later cycles. In cycle 4.1, gradually fresher water is measured at this location. Since only deep infiltration occurs during this phase, it means that the increase in freshness during this period is not caused by the injection. This could be due to the water having difficulty flowing into the observation well at this point or higher dispersion at this depth.

Local heterogeneities can also play a role in differences between the model and measurements. This can be observed, for example, in phase 7.1 at a depth of -104 mNAP. In observation well 19FNW012, both the model and measurements show a freshwater trend, but in contrast, measurements at observation well 19FNW004 indicates saltier water than the model suggests. It is possible that locally injected drinking water has become trapped in local clay particles in previous cycles and is subsequently flushed out of the well during phase 7.1.

The final step is the comparison between the model and borehole logging measurements (BGM). Figure 6.6 presents the model results for four different dates along with the BGM measurements. It should be noted that reliable measurements are not available throughout the entire depth of observation well 19FNW004. This is due to measurement disturbances caused by a metal cable getting stuck during installation. The left side of the figures illustrates the subsurface profile, with yellow representing sand and green representing clay. Additionally, the locations of both filters in the pumping well are indicated, and the arrows provide an indication of pumping activity.

In the top-left panel of the figure, the initial situation is depicted, where a clear difference is observed between the measurements and the model. This discrepancy is attributed to the conversion of these measurements, as described in Section 3.5.3, which was not performed in this study. However, the measurements do provide a good indication of the approximate boundaries of the interface and the arrival of drinking water in the observation wells. Similar to the DTS measurements, there is a margin of 3 m in the interpretation of the measurements, as the measurement values are presented per meter, while the layers of the numerical model have a thickness of 2 m.

In the top-right panel, it is evident that the injected water first arrives at depths of -60 mNAP and -100 mNAP. Based on the measurements in the pumping well and observation well 19FNW012, the bottom two panels demonstrate that the model can simulate the interface accurately both at deeper and shallower depths. However, in the deeper section, at observation well 19FNW004, this simulation is somewhat less accurate due to the absence of clay layers at -85 mNAP and -90 mNAP. The influence of these clay layers is further discussed in Section 7.2.

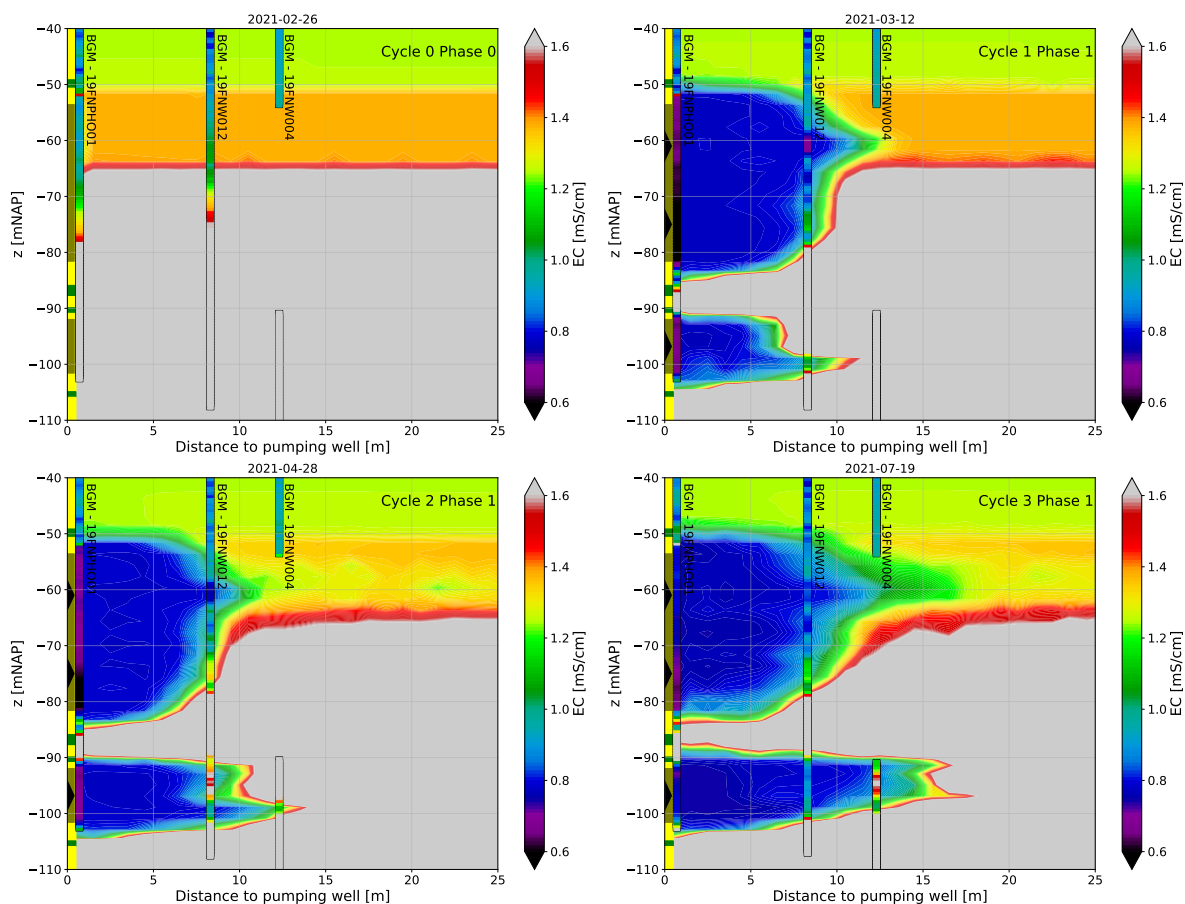


Figure 6.6: The contour plot illustrates the model's results and borehole logging measurements (BGM) for four different dates, depicting the distribution of solutes. The left side of the figures shows the geologic profile, with sand depicted in yellow and clay in green. The positions of the filters in the pumping well are marked, and the arrows indicate pumping activities.

In this study, the transition zone has been mentioned several times. Looking at the model results in Figure 6.6, it can be observed that the transition zone expands as multiple cycles are completed. The decrease in gradient is also evident. However, it should be noted that mechanical dispersion causes more mixing at depths where water flows faster, such as at -60 mNAP and -68 mNAP. During pumping, water flows faster in these areas, potentially allowing the mixed water to reach the pumping well more quickly.

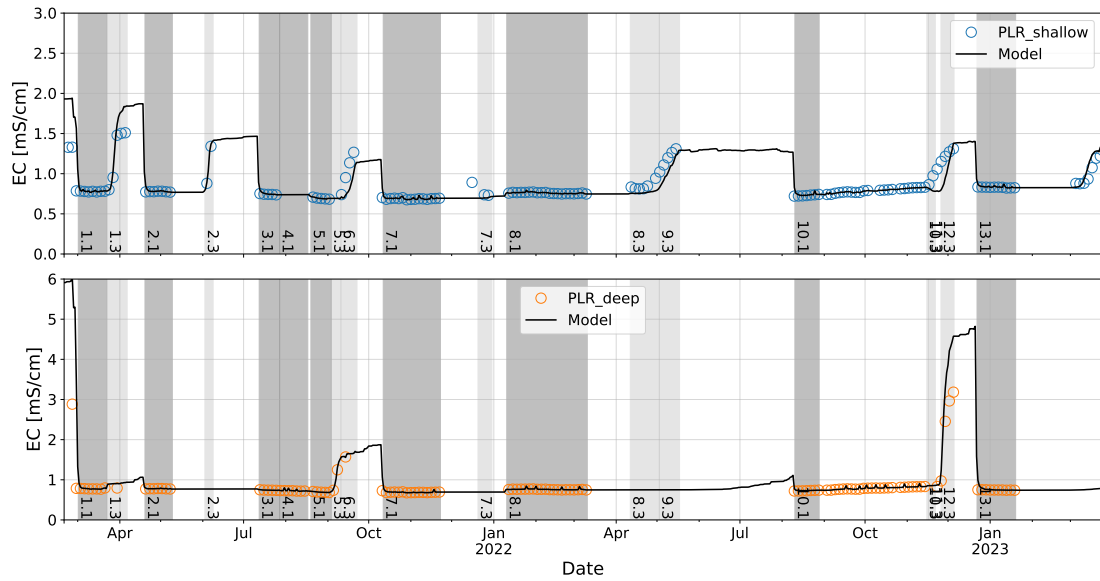


Figure 6.7: *The measured and modelled EC of extracted water.*

The amount of water that can be extracted needs to be determined to assess the performance of the ASR system. In this study, the EC values have been used as a quality parameter for the extracted water. Figure 6.7 shows the EC measurements for the shallow and deep filters in the pumping well (see Section 3.5.1), indicated by the blue and orange lines, respectively. Additionally, the modelled EC values of the extracted water are represented by the black line. In both cases, the model aligns well with the measurements. Using these figures, the recovery efficiency was then calculated. According to the model, a recovery efficiency of 32% is achieved, which is slightly higher than the recovery efficiency based on measurements, which is 30%.

7 The potential of the ASR system in Hoorn

This chapter aims to explore the possibility to increase the recovery efficiency of the ASR system in Hoorn. Section 7.1 provides an overview of the approach taken. Subsequently, Section 7.2 discusses the impact of clay layers situated between the two filters where is being pumped. In this section, findings that emerged during previous analyses but have not yet been discussed are addressed. Additionally, the heterogeneity of these clay layers remains unclear. Local heterogeneity cannot be accounted for in the current model. However, an examination was conducted to understand the functioning of the system in the absence of clay layers or with only one clay layer. These scenarios could occur when a new well is drilled. Subsequently, options for enhancing the current system were explored. Two scenarios were examined: the first involves injecting water around these clay layers (Section 7.3), while the second scenario investigates the use of a check valve (Section 7.4). These sections provide valuable insights to optimise the ASR system's performance.

7.1 Introduction

The assessment of the potential of ASR in Hoorn involves evaluating the current situation. First, the influence of the presence or absence of clay layers around -85 mNAP and -90 mNAP is discussed. This requires an explanation of the findings based on the model and measurements. Next, the design is evaluated by examining how it would perform with a single clay layer at -85 mNAP. In the initial design of the ASR, no consideration was given to the presence of these clay layers. Therefore, the current design is also tested in a scenario where none of these clay layers are present.

After understanding the impact of these clay layers, the focus shifted to optimising the current design. Two scenarios were examined. The first scenario involves placing a filter around the clay layer and injecting water between and just above the clay layers. The second scenario is the use of the shallow filter with a check valve. This allows infiltration across the entire filter and recovery of water from a portion of it.

For the implementation of Section 7.3 and Section 7.4, a flow rate of 20 m³/h was used for shallow injection and 5 m³/h for deep injection. Only shallow extraction was considered with a flow rate of 60 m³/h. These values are based on the flow rates used in the pilot study (see Section 3.6). Additionally, it was assumed that the injected water has a constant quality and temperature. While this assumption facilitates the interpretation of the results, small deviations from these results may occur in reality. The recovery efficiency is calculated using the following formula:

$$RE = \frac{V_{out,DW}}{V_{in}} \quad (7.1)$$

where RE is the recovery efficiency, V_{in} is the injected volume in a cycle and $V_{out,dw}$ is the recovered volume of drinking water in a cycle. The volume is computed according to:

$$V = Q \cdot t \quad (7.2)$$

where Q is the discharge of the pump and t is the time of pumping. Whether the recovered water meets the required drinking water quality standards is determined as:

$$\begin{cases} V_{out,DW} : & 0 \geq EC_R - EC_{max} \\ V_{out,PW} : & 0 < EC_R - EC_{max} \end{cases} \quad (7.3)$$

where $V_{out,DW}$ is the volume of water that meets the required drinking water quality, $V_{out,PW}$ is the volume of water which does not meet the required drinking water quality, EC_R is the EC of the recovered water and EC_{max} is the maximum allowed EC of recovered drinking water so it meets the required drinking water quality, which is computed as:

$$EC_{max} = 1\% \cdot (EC_{AGW} - EC_{DW}) + EC_{DW} \quad (7.4)$$

where 1% is the maximum allowed mixing of drinking water with ambient groundwater, EC_{AGW} is the initial EC of ambient groundwater and EC_{DW} is the EC of injected water. It should be noted that salt concentrations may vary, and this is taken into account by determining the maximum electrical conductivity (EC_{max}) for each layer where water is being pumped.

7.2 Influence of the clay layers between the two pump filters

7.2.1 Current situation

In Chapter 6, the influence of clay layers around -85 mNAP and -90 mNAP were already introduced. The analysis with temperature revealed that these layers cause separate flow of the injected water in the aquifer. Due to the relatively high diffusion of heat (compared to solute transport), it eventually spreads through these clay layers.

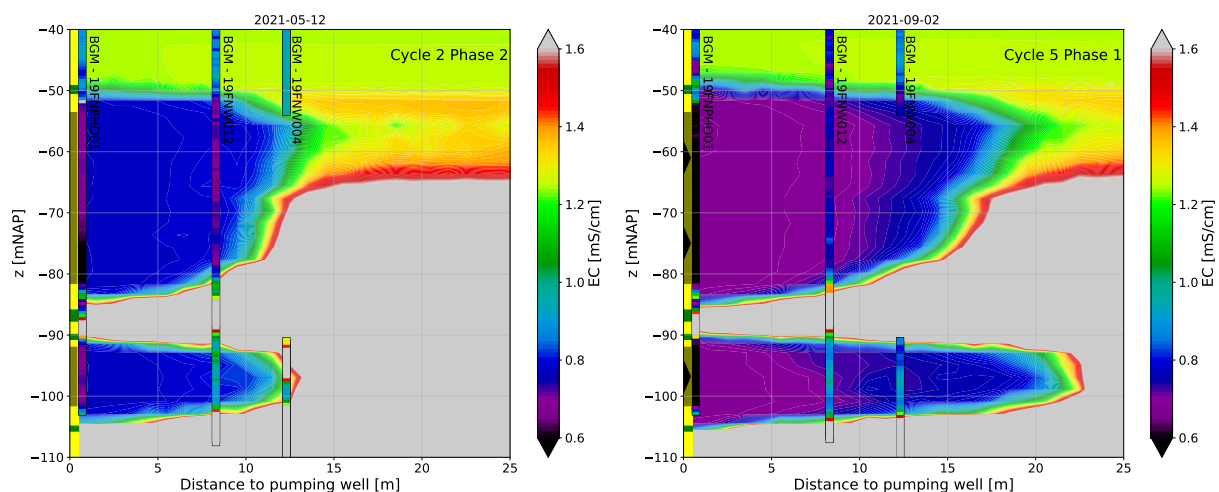


Figure 7.1: The contour plot illustrates the model's results for solute transport in the aquifer along with the background groundwater measurements for three different dates. The left side of the figures shows the geologic profile, with sand depicted in yellow and clay in green. The positions of the filters in the pumping well are marked, and the arrows indicate pumping activities.

The separating effect of these layers becomes more apparent when looking at the EC measurements combined with the model (Figure 7.1). Borehole logging (BGM in the figure) of the pumping well (19FNPHO01) and two observation wells (19FNW012 and 19FNW004) are shown. It should be noted that reliable measurements are not available throughout the entire depth of observation well 19FNW004. This is due to measurement disturbances caused by a metal cable getting stuck during installation. The conversion of these measurements to EC values requires considerations such as lithology, temperature, and formation factor. This conversion is not conducted in this study. Therefore, the BGM has been used as a rough indication to understand

the flow of injected water in the aquifer. On the left side of the figures, the sand layers (yellow) and clay layers (green) are depicted, along with the filters where water is pumped.

As shown in Figure 7.1, both the model and the BGM in the pumping well and observation well 19FNW012 clearly indicate that the injected water flows between the clay layers around -90 mNAP and -105 mNAP. Interestingly, there is a difference observed in observation well 19FNW004. In the left panel, fresher water is measured at a depth of approximately -90 mNAP. This water must originate from the injected water in the deeper part of the aquifer since the interface of the injected water has not reached this distance in the shallower part of the aquifer yet. Due to the absence of the clay layers around -85 mNAP and -90 mNAP at observation well 19FNW004, it appears that the water flows to these depths. This is also evident in the right panel. The interface at -90 mNAP is visible in observation well 19FNW012 but not in observation well 19FNW004, indicating that the water has flowed upward in this region.

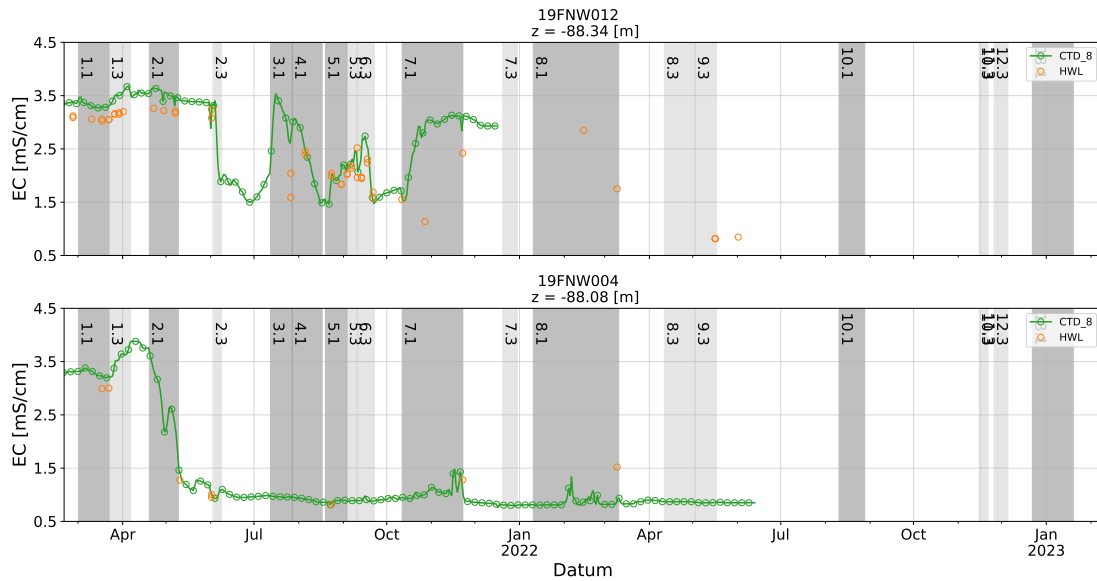


Figure 7.2: Changes in EC during the pilot in the two observation wells (19FNW012 and 19FNW004) around -88 mNAP are depicted. Periods shown in dark gray indicate when water is injected and the light gray areas represent the recovery periods.

The influence of this upward flow was further examined based on the EC measurements at a filter depth around -88 mNAP (Figure 7.2). In observation well 19FNW012, the measurement is between the clay layers. The flow of water is most evident during cycle 2. After the infiltration period (2.1), it can be observed that the water in observation well 19FNW012 remains saline, while it becomes fresh in observation well 19FNW004. This is the upward flow around this well, as described earlier. During the extraction phase in this cycle (2.3), only the shallow part of the aquifer is pumped. As a result of this extraction, the water at -88 mNAP in observation well 19FNW012 becomes fresher. As mentioned before, this water can only come from the deeper part of the aquifer. This means that due to this extraction, deep injected water ends up between the clay layers.

Figure 7.3 depicts a sketch of the findings described above. In the left panel, an injection period is shown. Due to the presence of saltier (heavier) water in the deeper part of the aquifer and the absence of intermediate clay layers, the injected freshwater (lighter) tends to flow upward.

The water in this region is less salty (and lighter), offering an easier path with less resistance. In the right panel, a recovery period is depicted. The flow is directed towards the well (e.g., to the left). Due to the absence of clay layers, this flow seems to push the water that infiltrated deeper into the aquifer between the clay layers.

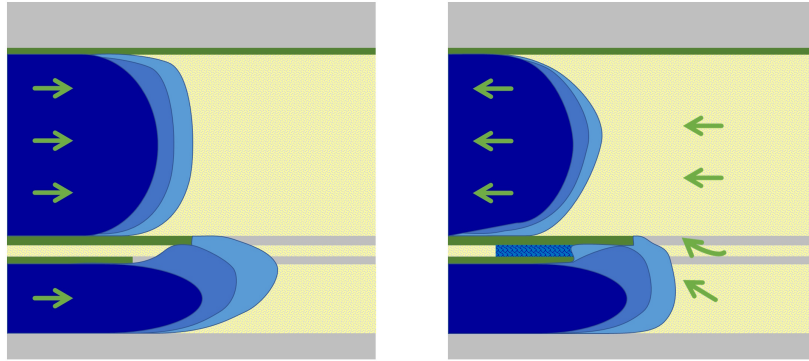


Figure 7.3: Sketch illustrating the process of freshwater moving between the clay layers.

7.2.2 Single clay layer

In the current situation, there are two clay layers (-85 mNAP and -90 mNAP) between the filters where water is injected. Examining a situation with a single clay layer further helps us understand the influence of a clay layer in an ASR system. This helps to identify the general impact of an intermediate clay layer. Figure 7.4 clearly demonstrates this influence. Regardless of random pumping schedules, the resistance of a clay layer creates a saline water plume between the shallow and deep injected water. Such an ASR system will not function effectively, requiring a critical assessment of the pump used in the deeper part of the aquifer.

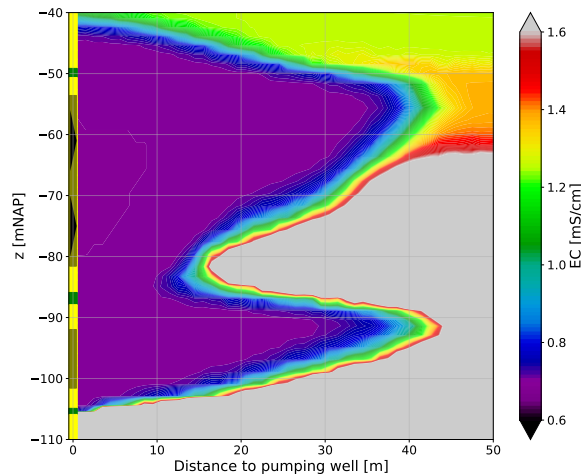


Figure 7.4: The contour plot displays the result of the influence of a single clay layer between the pumping filters. The left side of the figures shows the geologic profile, with sand depicted in yellow and clay in green. The positions of the filters in the pumping well are marked.

7.2.3 No clay layer

The pilot was designed under the assumption that there would be no clay layers present around -85 mNAP and -90 mNAP. In the future, if multiple ASR wells are to be installed in the vicinity, it is possible that these clay layers may not exist in other locations. To ensure proper coordination among these wells, it may be necessary to use the same filter depths for pumping in those areas. Therefore, the performance of the current system when no clay layers are present around -85 mNAP and -90 mNAP is examined.

In this situation, it is important to create a water bubble without a saline tongue between the pumping filters. This means that the area between these filters needs to be initially filled. This can be achieved by injecting water at a deep level, as shown in the upper left part of Figure 7.5. Subsequently, this water rises to the appropriate depths (see upper middle part of Figure 7.5). Once the intermediate zone is filled, both pumps can inject water, resulting in a single bubble formation (see upper right part of Figure 7.5). Now that this bubble is created, the ASR system can be operated, as shown in the lower figures of Figure 7.5. It should be noted that shortly after a recovery period, water replenishment needs to occur relatively quickly to maintain the intermediate section filled with injected water.

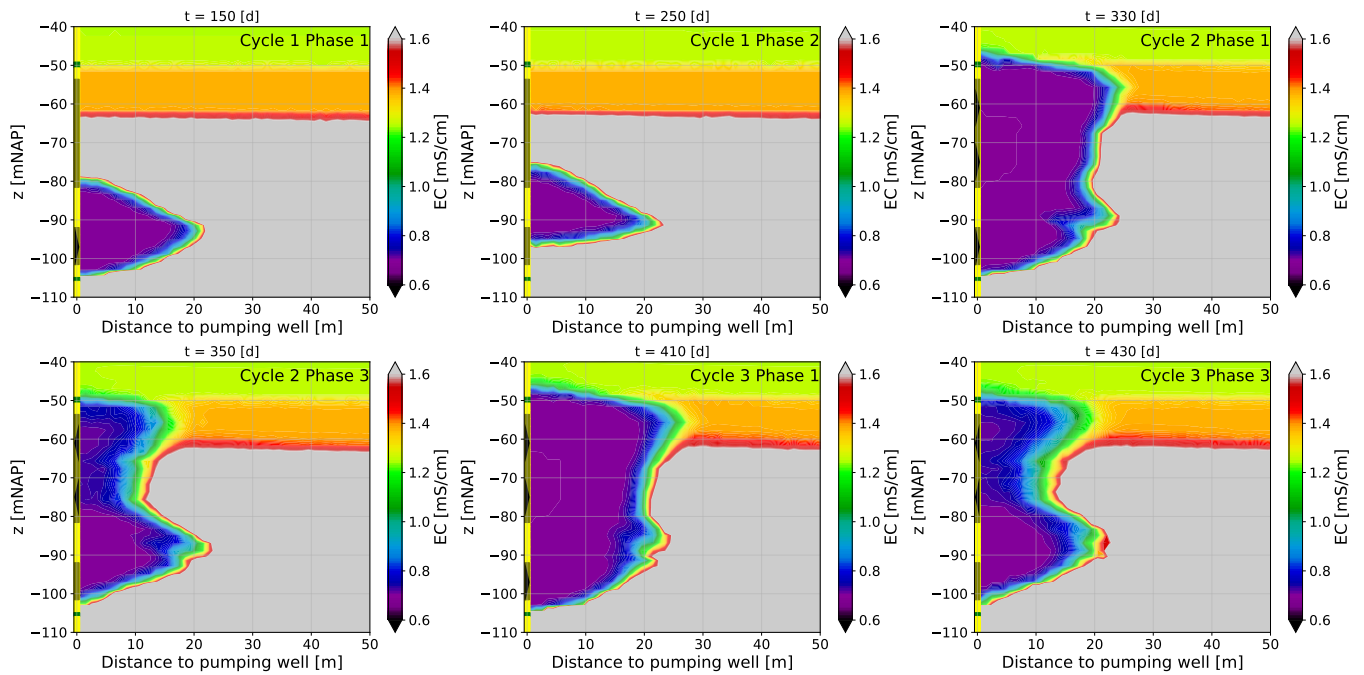


Figure 7.5: The contour plot displays the result of a possible pumping scheme in the case without a clay layer between the pumping filters. The left side of the figures shows the geologic profile, with sand depicted in yellow and clay in green. The positions of the filters in the pumping well are marked.

7.3 Pumping water around the clay layers between the two pump filters

An exploration was conducted to improve the current ASR system by considering the possibility of utilising a filter to inject water between the clay layers around -85 mNAP and -90 mNAP, as well as just above these clay layers. The objective is to flush out the natural water between the clay layers and create a freshwater bubble directly above these clay layers.

Three pumping schemes have been studied. In the first scheme, injection occurs initially around the clay layers, followed by injection in both filters in the pumping well (left in Figure 7.6). In the second scheme, injection takes place first in the shallow filter of the pumping well, and then both filters are used for injection (middle in Figure 7.6). In the last scheme, injection occurs simultaneously at both depths (right in Figure 7.6). For all three pumping schemes, the situation is shown after 55 days and after 100 days. It is already evident that such a system results in high mixing around these clay layers. Pumping in or around these clay layers will not improve the functioning of the ASR system.

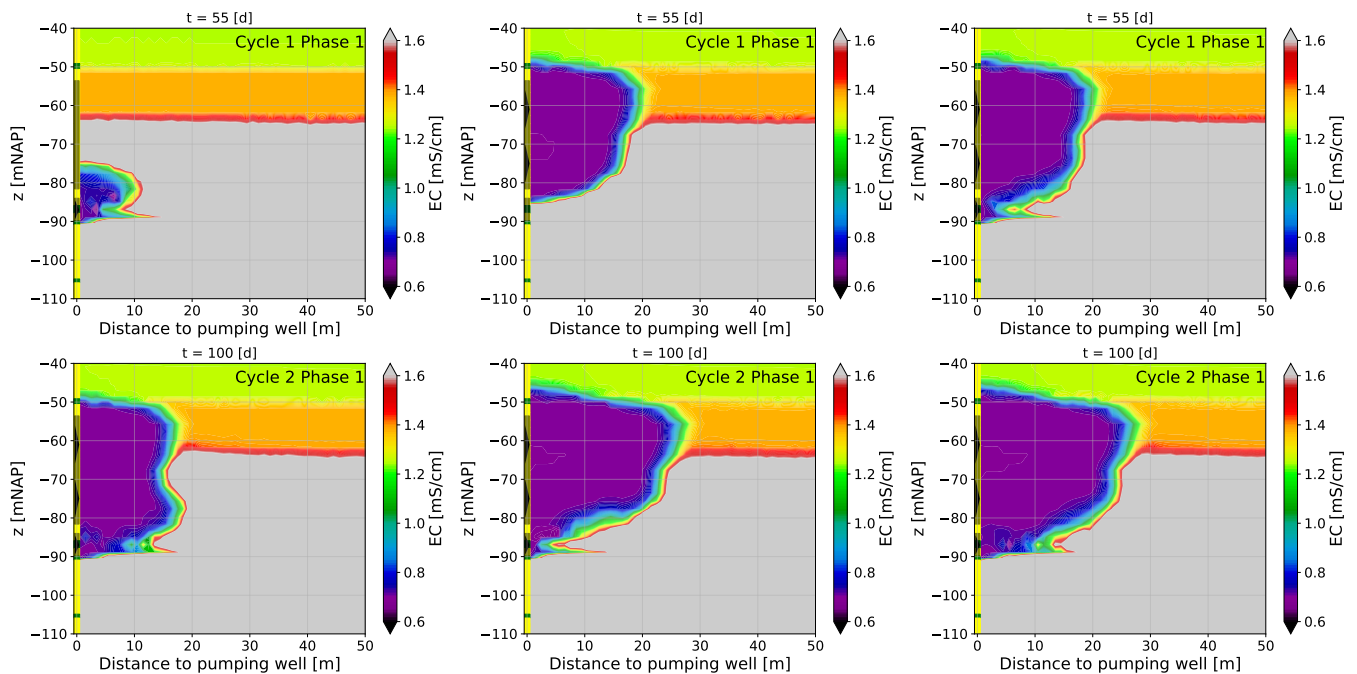


Figure 7.6: Comparison of three injection strategies: (left) injection around the clay layers followed by injection in both filters, (middle) injection in the shallow filter before using both filters, and (right) simultaneous injection at both depths.

7.4 Using a check valve

Based on the previous analyses, it is concluded that using a deeper filter for water injection does not yield the desired results. Therefore, an investigation was conducted to explore the possibility of improving the ASR system by utilising only the shallow filter. This involved examining the potential of implementing a check valve.

A check valve is a mechanism used to allow fluid flow in one direction and prevent back-flow. It consists of a valve that opens when the flow is in the desired direction and closes when the flow is reversed. This check valve can be utilized to enable water injection across the entire filter and during recovery, allowing a portion of the filter to be used for water retrieval.

An investigation was conducted to determine the depth at which the check valve can be placed to achieve the highest recovery efficiency, calculated using Equation 7.1. In this analysis, injection was carried out for a duration of 60 days, followed by extraction until the water quality reached an insufficient level, as described by Equation 7.3. This process was repeated until the recovery efficiency reached a constant value.

When a smaller part of the filter is used for recovery, the mixed water reaches the shallow part of the extraction filter faster. Conversely, when a larger part of the filter is used for recovery, the mixed water first reaches the deep part of the extraction filter. This is clearly visible in Figure 7.7, where the left image shows the check valve at 60% filter depth, while the right image shows it at 70% filter depth. The recovery efficiency for both designs is presented in Table 7.1.

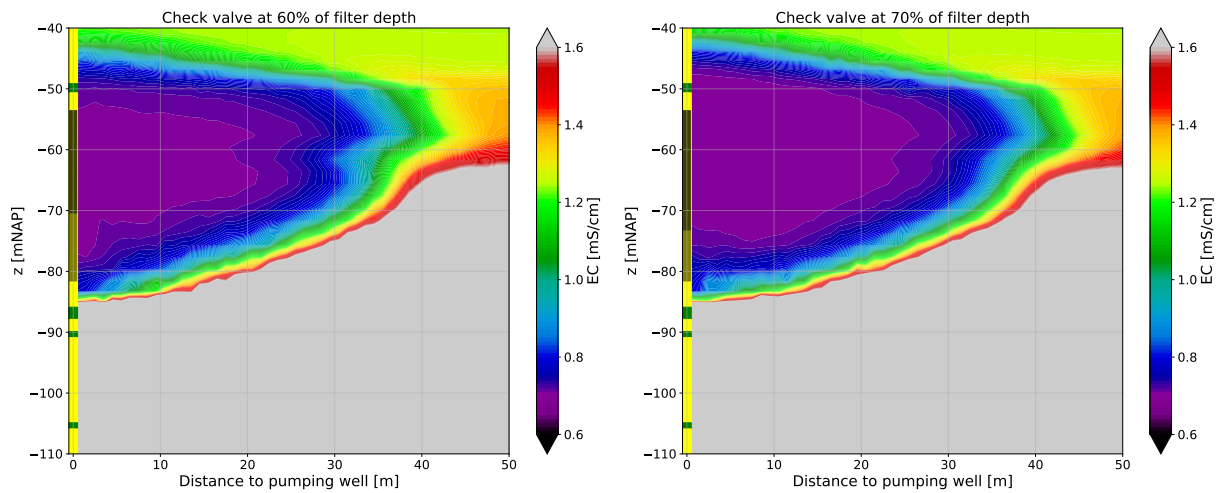


Figure 7.7: Arrival of the mixed water during recovery with a check valve at 60% and 70% filter depth. The left side of the figures shows the geologic profile, with sand depicted in yellow and clay in green. The positions of the filters in the pumping well are marked.

Table 7.1: Cycles performed using a check valve to close part of the filter during recovery.

Cycle	Phase	Discharge	Duration	RE	Duration	RE	Duration	RE
		[m ³ /d]	[d]	[%]	[d]	[%]	[d]	[%]
1	1	-480	60	15	60	25	60	25
	3	1440	3		5		5	
2	1	-480	60	60	60	60	60	55
	3	1440	12		12		11	
3	1	-480	60	75	60	75	60	70
	3	1440	15		15		14	
4	1	-480	60	75	60	80	60	70
	3	1440	15		16		14	
5	1	-480	60	75	60	80	60	70
	3	1440	15		16		14	
Check valve at:			60% of the pump filter	65% of the pump filter	70% of the pump filter			

The maximum achievable recovery efficiency is obtained by placing the check valve at a depth between the depths described above, as shown in Table 7.1. When the check valve is positioned around 65% depth, a recovery efficiency of 80% is achieved after three cycles. Figure 7.8 illustrates the results for this design at the beginning of cycle 4 (left), end of injection (middle), and end of recovery (right). A remark regarding this analysis is that buoyancy effects have not been taken into account. When this effect occurs, the injected water may slightly rise, which could result in a small deviation from the calculated recovery efficiency. Based on this analysis, it is recommended to place the check valve between 60% and 65% filter depth.

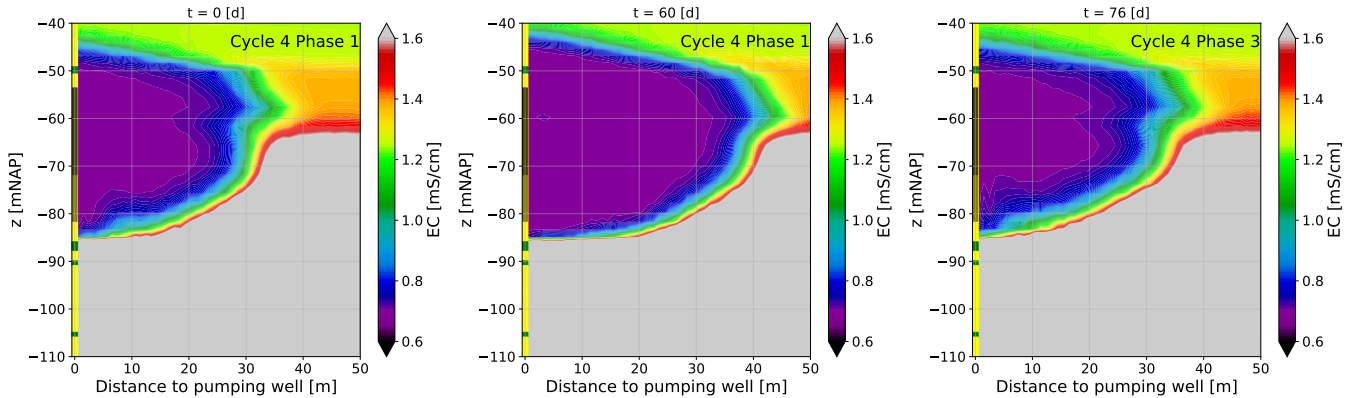


Figure 7.8: The results of the model with a check valve at 65% filter depth during cycle 4 are shown, with the start of injection on the left, the end of the injection period and the start of the recovery period in the middle, and the end of the recovery period on the right. The left side of the figures shows the geologic profile, with sand depicted in yellow and clay in green. The positions of the filters in the pumping well are marked.

8 Conclusions and recommendations

8.1 Conclusions

The objective of the research is to investigate how the recovery efficiency of the Aquifer Storage and Recovery (ASR) system in Hoorn can be improved. The recovery efficiency is defined as the amount of water that can be recovered compared to the amount of infiltrated water. An important requirement is that the recovered water is of such quality that it can be used almost immediately. It is required that the extracted water in the ASR system can not exceed a 1% dilution ratio with the ambient groundwater. Conservative solute transport and heat transport were used to estimate the interface between injected water and ambient groundwater in order to achieve this goal.

8.1.1 Key processes resulting in losses of recoverable water of the ASR system

The key processes responsible for losses in the ASR system in Hoorn are lateral flow, mechanical dispersion, diffusion, and buoyancy. In the chosen environment, the hydraulic gradient is very small, resulting in minimal impact from natural lateral flow on the ASR system once water has been injected.

Mechanical mixing occurs due to differences in flow velocities and directions, resulting in the mixing of injected water with the surrounding groundwater. This leads to the formation of a transition zone where the water gradually increases in salinity away from the injected water.

Mixing of water also occurs due to concentration differences between the injected water and the surrounding groundwater. This process is known as diffusion and also contributes to the formation of the transition zone. For both mechanical mixing and diffusion, their impact decreases as the size of the transition zone increases.

The last process that significantly affects the performance of the ASR system is buoyancy, where heavier water flows beneath lighter water. Drinking water is lighter than the saltier ambient groundwater in Hoorn. Placing the ASR system in a confined aquifer helps mitigate the buoyancy effect and keeps the drinking water in place. Additionally, a Multi Partially Penetrating Well (MPPW) can be used, where infiltration occurs over the entire depth but only extraction occurs from shallower depths. The deeper filter is intended to delay buoyancy effects.

8.1.2 Modeling the ASR system using heat and conservative solute transport

In order to ensure accurate modeling of the ASR system, the precision of a radially symmetric model using SEAWAT and MODFLOW 6 was assessed. This started by comparing groundwater flow with analytical solutions as Thiem, de Glee and Hantush. Subsequently, the radially symmetric model was evaluated by comparing its performance with 2D models in capturing essential processes related to conservative solute transport and heat transport, including mechanical dispersion, diffusion, retardation, and buoyancy.

The presence of numerical dispersion in the solution methods for the transport equation in MODFLOW 6 prohibits the use of MODFLOW 6. This issue arises in advection-dominated problems like the ASR, making it insufficiently accurate for this research. The spread of the concentration significant increases during an ASR cycle due to numerical dispersion, even with finer discretization. Based on relevant pumping rates, the numerical dispersion in MODFLOW 6 is equivalent to a dispersivity of 0.2 m in a numerical model without dispersion, such as SEAWAT. It is important to note that as the dominance of advection diminishes, the numerical dispersion also decreases.

Model results were compared with measurements of hydraulic head, temperature, and electrical conductivity (EC). The analysis has led to the differentiation of 19 layers, involving adjustments of 16 values for hydraulic conductivity, 7 values for the adsorption coefficient in heat transport, and 5 values for porosity compared to the initial estimates. The parameters were adjusted manually to achieve the closest possible agreement with the measurements.

In general, the model shows good agreement with measurements of hydraulic head, temperature, and electrical conductivity (EC). However, there are a few significant differences observed at a depth of approximately -87 mNAP, which can be attributed to the presence of two heterogeneous clay layers in that area. In this study, a single dispersivity value was used, and based on temperature measurements, this seems reasonable. However, minor differences can be observed, such as at a depth of -50 mNAP, where the dispersivity is lower.

8.1.3 Modeling the recovery efficiency of the ASR system

The model was used to determine the arrival of mixed water at the filter where water is extracted in order to calculate the recovery efficiency. The current system is able to achieve a recovery efficiency of 30%. The scenarios were initially qualitatively assessed to determine if they had the potential to achieve a high recovery efficiency. When a scenario showed potential for high recovery efficiency, it was also quantitatively evaluated. In this evaluation, the 1% threshold values were calculated based on the electrical conductivity (EC) values of the surrounding groundwater, which increase with depth, and the EC values of the drinking water in order to calculate the recovery efficiency of a scenario. Although the model can simulate the interface quite accurately, there are some uncertainties to consider, especially the heterogeneity of the clay layer is not accounted for. Additionally, there may be minor deviations in dispersivity.

8.1.4 Influence of the clay layers around -85 mNAP and -90 mNAP

The ASR system in Hoorn is designed as a Multi Partially Penetrating Well to delay buoyancy effects by injecting water into the deep filter. However, there are two clay layers between the deep and shallow filters in the pumping well, which significantly influence the functioning of the ASR system. Due to these clay layers, the system does not operate as a single entity; instead, it creates a distinct zone of infiltrated water below these clay layers and another zone above them. The shallow filter is only a few meters above one of the clay layers. As a result of buoyancy effects, the ambient groundwater quickly reaches the shallow filter during a recovery phase. This greatly impacts the operation of the ASR system, as the recovery efficiency remains low.

The clay layers between the filters in the pumping well are not present at a distance of 12.3 meters from the well. Due to this heterogeneity, it appears that the water that has infiltrated deeper at a distance of 12.3 m from the pumping well flows upward and reaches the space between these clay layers during the recovery phase. The radially symmetric model used in this study cannot account for this heterogeneity. To gain insight into the influence of their presence or absence, this study considered two scenarios: one with a single clay layer and one without a clay layer. In the scenario with a single clay layer, the water that infiltrates below the clay reaches the area above the clay. However, this requires injecting massive volumes of water, and the clay layer still hinders the proper functioning of the ASR system. In a situation where there is no clay layer between the two filters in the pumping well, the system performs more effectively. However, since the distance between the filters is 10 meters, the system's performance is strongly dependent on buoyancy effects. The section between the two filters needs to be filled first before the ASR system can function properly.

8.1.5 Improving the monitoring system of the ASR system

The current research is based on two observation wells that are almost aligned with the ASR well. This allows for the estimation of heterogeneity in the radial direction. However, due to the stringent quality requirement (1% mixing), the heterogeneity must be estimated in three dimensions. Positioning three or four monitoring wells in different directions around the ASR well is necessary to achieve this. The inclusion of these new observation wells also allow for a more precise estimation of dispersivity.

8.1.6 Improving the recovery efficiency of the ASR system in Hoorn

The clay layers between the deep and shallow filters in the pumping well pose the largest problem in the current system causing a maximum achievable recovery efficiency of 30%. Using only the shallow filter eliminates this influence. Water mixing is unavoidable, but conducting multiple cycles builds a transition zone that reduces its impact. The shallow filter remains constrained by clay layers, where infiltrated water resides. However, it is important to consider buoyancy effects that cause ambient groundwater to reach the pumping well.

The objective of the research was to investigate how the recovery efficiency of the ASR system in Hoorn can be improved. This can be achieved by using a check valve in the shallow filter of the pumping well. This allows the entire filter to be utilized for water injection, while only a part of the filter is used for water recovery. In this design, the deeper part of the filter is intended to delay buoyancy effects. The check valve should be placed so that 65% of the shallow filter is used for water recovery, achieving a recovery efficiency of 80% for the current system after 4 cycles. During the analysis, the effect of buoyancy was not investigated extensively as only injection and recovery periods were studied. In reality, there will also be periods without pumping activities. During these periods, water will rise, which causes a small deviation from the calculated recovery efficiency. Mainly the heterogeneities in the soil composition and model assumptions prevent the exact simulation of the 1% threshold. Taking into account the discussed uncertainties and reducing the effects of dispersion, diffusion, and buoyancy, it is therefore important to invest in the transition zone. As this zone becomes larger, the gradient decreases, resulting in a decrease in diffusion. Additionally, the flow velocity also decreases as this zone moves farther from the pumping well, leading to a reduction in mechanical dispersion. This means that a larger transition zone will result in a more reliable extraction of water that meets the required quality standards is ensured.

8.2 Recommendations

In an ASR system, dispersion is an important process. Although the influence of this process decreases after a few cycles, due to the build-up of a transition zone, it is still important to further study it. Based on the DTS measurements, a better estimate can be made for dispersion in heat transport. For solute transport, dispersion can be better assessed by utilising borehole measurements. However, it should be noted that interpreting borehole logging can be challenging due to lithology, temperature, and formation factors. Given the proven value of these continuous measurements in this research, it is crucial to delve deeper into borehole logging.

This research is based on results obtained from a radially symmetric model, which is based on the method proposed by Langevin (2008). One limitation of this method is that it assumes homogeneous layers and does not allow for incorporating heterogeneity. As mentioned, the clay layers around -85 mNAP and -90 mNAP influence the performance of the ASR system. For this purpose, the method prescribed by Louwyck et al. (2014) could be employed, as it enables the inclusion of heterogeneity in a radially symmetric model. Using this method, a closer examination

can be conducted on the upward movement of water from the deeper part of the aquifer at a distance of 12.3 m from the pumping well. Another possibility is to utilise a 2D model, as was already explored in this study.

This research has focused on improving the existing system to increase the recovery efficiency of the ASR system. However, the findings from this study can also be applied in the design of a new system. For instance, different filter depths can be chosen in the pumping well, or a design can be considered at a location 12.3 m away where no clay layer is present.

Ultimately, SEAWAT was chosen for the modeling because numerical dispersion in MODFLOW 6 was too large. The analysis of numerical dispersion was limited to situations relevant to this research and to a single-layer system. Further investigation is needed to investigate numerical dispersion by examining multi-layer systems and different types of flow (for example, recharge instead of pumping). Additionally, the relationship must be studied between the applied flow rates and numerical dispersion.

References

- Axelsson, O., & Marinova, R. S. (2014). A hybrid method of characteristics and central difference method for convection-diffusion problems. Retrieved from <https://www.researchgate.net/publication/228696072>
- Borst, L. (2020). MER aanmeldingsnotitie. (unpublished)
- Borst, L. (2022). ASR Hoorn, bijpraten Martine. (unpublished)
- Borst, L. (2023). ASR Hoorn Deelrapport bodem en grondwater en modellering. (unpublished)
- Chadd, M. (2023). De geleiding van stroom. Retrieved from <https://www.mrchadd.nl/academy/vakken/anw/de-geleiding-van-stroom#:~:text=Een%20gesmolten%20zout%20geleidt%20de,te%20groter%20de%20stroomgeleiding%20is.>
- Cirkel, G., Blokker, M., & Dorland, E. (2016). Toekomstig watergebruik en piekfactoren bij klimaatverandering. Retrieved from <https://www.kwrwater.nl/projecten/toekomstig-watergebruik-en-piekfactoren-bij-klimaatverandering/>
- Cooper, H. H., Kohout, F. A., Henry, H. R., & Glover, R. E. (1964). Sea water in coastal aquifers. *GEOLOGICAL SURVEY WATER-SUPPLY PAPER, 1613-C*.
- de Glee, G. (1930). Over grondwaterstromingen bij wateronttrekking door middel van putten (Tech. Rep.). Delft University. (PhD thesis)
- Dekking, F. M., Kraaikamp, C., Lopuhaä, H. P., & Meester, L. (2005). A Modern Introduction to Probability and Statistics. Springer.
- Drinkwaterplatform. (2022). Watervbruik in Nederland. Retrieved from <https://www.drinkwaterplatform.nl/themas/waterbesparing/cijfers-watervbruik/#:~:text=Piekverbruik%20bij%20warm%20en%20droog,de%20tuin%20krijgen%20extra%20water.>
- Grondwaterformules. (2023). Onttrekking in een dik freatisch pakket of in een watervoerend pakket onder een kleilaag. Retrieved from <http://grondwaterformules.nl/index.php/formules/onttrekking/dik-pakket-met-vaste-rand>
- Hantush, M. S., & Jacob, C. E. (1955). Non-steady radial flow in an infinite leaky aquifer. *Eos, Transactions American Geophysical Union*, 36(1), 95-100.
- Langevin, C. D. (2008, 7). Modeling axisymmetric flow and transport. *Ground Water*, 46, 579-590. doi: <https://doi.org/10.1111/j.1745-6584.2008.00445.x>
- Langevin, C. D., Provost, A. M., Panday, S., & Hughes, J. D. (2022a). Groundwater Transport Model: U.S. Geological Survey Techniques and Methods,. United States Geological Survey. doi: <https://doi.org/10.3133/tm6A61>.
- Langevin, C. D., Provost, A. M., Panday, S., & Hughes, J. D. (2022b). Groundwater Transport Model: U.S. Geological Survey Techniques and Methods. doi: <https://doi.org/10.3133/tm6A61>
- Langevin, C. D., Thorne, D. T., Dausman, A. M., Sukop, M. C., & Guo, W. (2008). SEAWAT Version 4: A Computer Program for Simulation of Multi-Species Solute and Heat Transport: U.S. Geological Survey Techniques and Methods Book 6, Chapter A22, 39 p. U.S. Geological Survey.
- Louwyck, A., Vandenbohede, A., Bakker, M., & Lebbe, L. (2014). Procédure modflow pour simuler l'écoulement axisymétrique dans des systèmes aquifères hétérogènes radialement et stratifiés. *Hydrogeology Journal*, 22, 1217-1226. doi: 10.1007/s10040-014-1150-0
- Luo, J., Georgakakos, A., Wang, J., Yao, H., & Deng, Y. (2014). AQUIFER STORAGE AND RECOVERY IN SALINE AQUIFERS (Tech. Rep.). Georgia Institute of Technology.
- Maas, K., & Veling, E. (2010). Een snelle benadering van de formule van Hantush (Vol. 16).
- Martin, R., & Dillon, P. (2002). Aquifer Storage and Recovery: Future Directions for South Australia (Tech. Rep.). The Department of Water, Land and Biodiversity Conserva-

- tion. Retrieved from https://www.researchgate.net/publication/288303894_Aquifer_storage_and_recovery_in_South_Australia
- Negm, A. M., & Eltarabily, M. G. A. (2017). Modeling of fertilizer transport through soil, case study: Nile Delta (Vol. 55). Springer Verlag. doi: https://doi.org/10.1007/698_2016_88
- Pauw, P. S., van Baaren, E. S., Visser, M., de Louw, P. G., & Essink, G. H. O. (2015, 11). Increasing a freshwater lens below a creek ridge using a controlled artificial recharge and drainage system: a case study in the netherlands. *Hydrogeology Journal*, *23*, 1415-1430. doi: <https://doi.org/10.1007/s10040-015-1264-z>
- PWN. (2022). Onboarding PWN. Retrieved from <https://eenpwn.pwn.nl/>
- Rhoades, J. D., Kandiah, A., & Mashali, A. M. (1992). The use of saline waters for crop production. Food and Agriculture Organization of the United Nations.
- Saline Agriculture Worldwide. (2023). Classification of saline water. Retrieved from <https://www.salineagricultureworldwide.com/classification-of-saline-water>
- Samani, N., Kompani-Zare, M., & Barry, D. A. (2004). Modflow equipped with a new method for the accurate simulation of axisymmetric flow. *Advances in Water Resources*, *27*, 31-45. doi: <https://doi.org/10.1016/j.advwatres.2003.09.005>
- Spierenburg, H.-J., & Borst, L. (2019). Beslisdocument Start definitiefase. pwnkia.sharepoint.com. (unpublished)
- Spierenburg, H.-J., & Borst, L. (2020a). Evaluatie van PWN's meetsysteem waterkwaliteit bij ASR pilot Hoorn. (unpublished)
- Spierenburg, H.-J., & Borst, L. (2020b). Programma van Eisen Pilot ASR Hoorn. (unpublished)
- Spierenburg, H.-J., & Borst, L. (2023). ASR Hoorn Syntheserapport technische haalbaarheid. pwnkia.sharepoint.com. (unpublished)
- Spierenburg, H.-J., Zuurbier, K., & Borst, L. (2020). ASR Hoorn watervergunning 2. (unpublished)
- Stuyfzand, P. J., & Borst, L. (2022). Kwaliteitsveranderingen van drinkwater tijdens PWN's ASR pilot Hoorn (Tech. Rep.). Stuyfzand Hydroconsult. (unpublished)
- Thiem, G. (1906). Hydrologische methoden. J.M. Gebhardt's Verlag, Leipzig.
- Tombe, B. F. D. (2016). Simulating heat transfer through the unsaturated zone of MAR systems With an application to the MAR system at PWN (Tech. Rep.). TU Delft.
- Ward, J. D., Simmons, C. T., Dillon, P. J., & Pavelic, P. (2009). Integrated assessment of lateral flow, density effects and dispersion in aquifer storage and recovery. *Journal of Hydrology*, *370*(1-4), 83-99. doi: <https://doi.org/10.1016/J.JHYDROL.2009.02.055>
- Zheng, C., & Wang, P. P. (1999). MT3D: A modular three-dimensional transport model for simulation of advection, dispersion and chemical reactions of contaminants in groundwater systems. Retrieved from <https://www.researchgate.net/publication/283742180>
- Zuurbier, K. (2016). INCREASING FRESHWATER RECOVERY UPON AQUIFER STORAGE A field and modelling study of dedicated aquifer storage and recovery configurations in brackish-saline aquifers (Tech. Rep.). Delft University of Technology. doi: <https://doi.org/10.4233/uuid:4631f3d2-14ff-4505-bcba-0c21956c460f>
- Zuurbier, K., Paalman, M., van Loon, A., & Stuyfzand, P. (2013). Aquifer storage and recovery (Tech. Rep.). <https://edepot.wur.nl/539553>: KWR.
- Zuurbier, K., Ros, S., & Stuyfzand, P. (2018). Verkenning inzet ASR voor opslag reinwater PWN. (unpublished)

Appendices

A Cycle operational values

Table A.1: *Flow rates used during the pilot.*

Cycle	Phase	Duration	Shallow		Deep	
			Qmean	Qmax	Qmean	Qmax
[-]	[-]	[d]	[m ³ /h]	[m ³ /h]	[m ³ /h]	[m ³ /h]
1	1 - Injection	21	14	15	6	13
	3 - Recovery	15	45	50	3	25
	4 - Rest	13				
2	1 - Injection	20	15	19	7	7
	2 - Storage	24				
	3 - Recovery	6	54	75	0	0
	4 - Rest	34				
3	1 - Injection	15	20	21	3	9
4	1 - Injection	21	0	0	14	45
	2 - Storage	2				
5	1 - Injection	15	19	22	5	5
	3 - Recovery	7	0	0	44	50
6	3 - Recovery	12	42	52	2	14
	4 - Rest	19				
7	1 - Injection	42	20	21	5	5
	2 - Storage	28				
	3 - Recovery	10	30	75	0	0
	4 - Rest	11				
8	1 - Injection	59	17	19	5	6
	2 - Storage	32				
	3 - Recovery	21	30	39	0	0
9	3 - Recovery	15	57	60	0	0
	4 - Rest	85				
10	1 - Injection	97	12	19	4	5
	2 - Storage	1				
	3 - Recovery	1	0	0	36	36
11	3 - Recovery	5	64	75	6	29
	4 - Rest	4				
12	3 - Recovery	10	75	75	67	74
	4 - Rest	17				
13	1 - Injection	28	18	19	5	5
	2 - Storage	20				

B Numerical dispersion

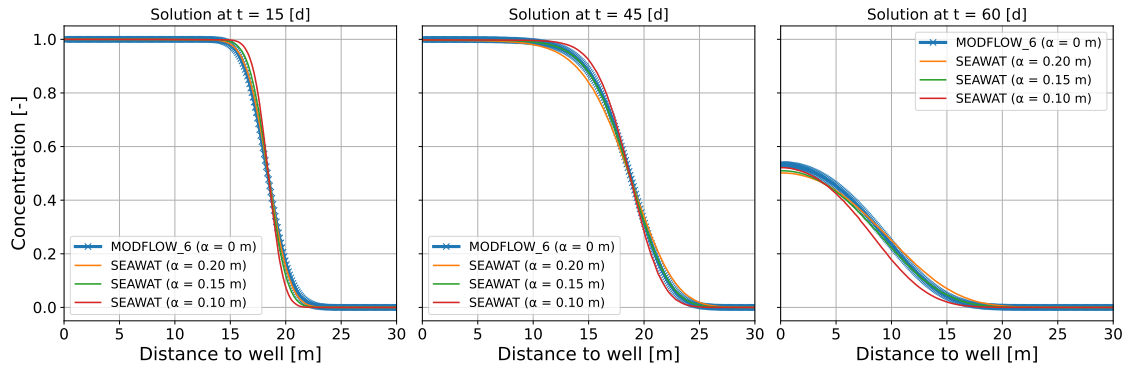


Figure B.1: Numerical dispersion of MODFLOW6 compared to SEAWAT results for different dispersion values.

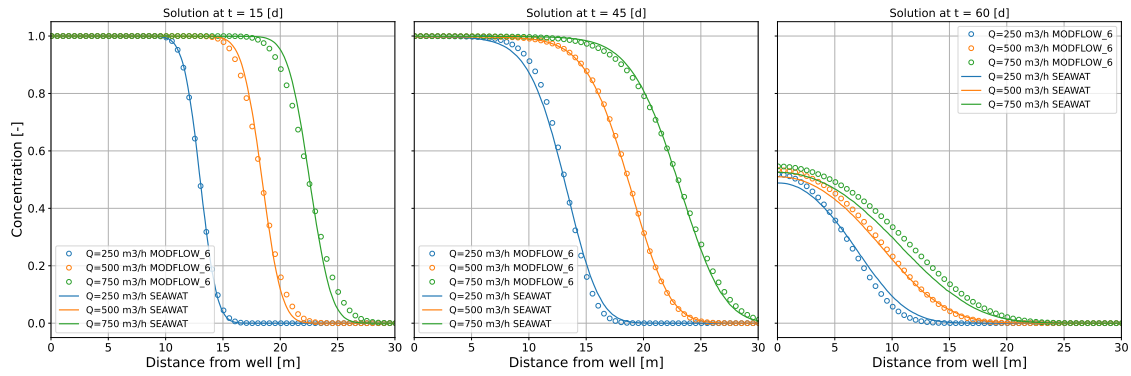


Figure B.2: MODFLOW6 advection model compared with a SEAWAT model with 0.2 m dispersion for different injection/recovery rates.

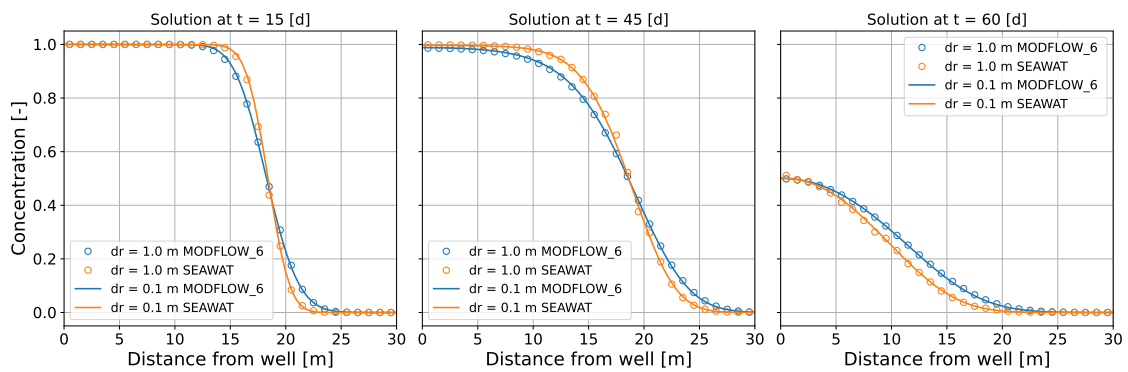


Figure B.3: MODFLOW6 advection model compared with a SEAWAT model with 0.2 m dispersion for different cell sizes used around the well.


C Borehole measurement at the ASR well

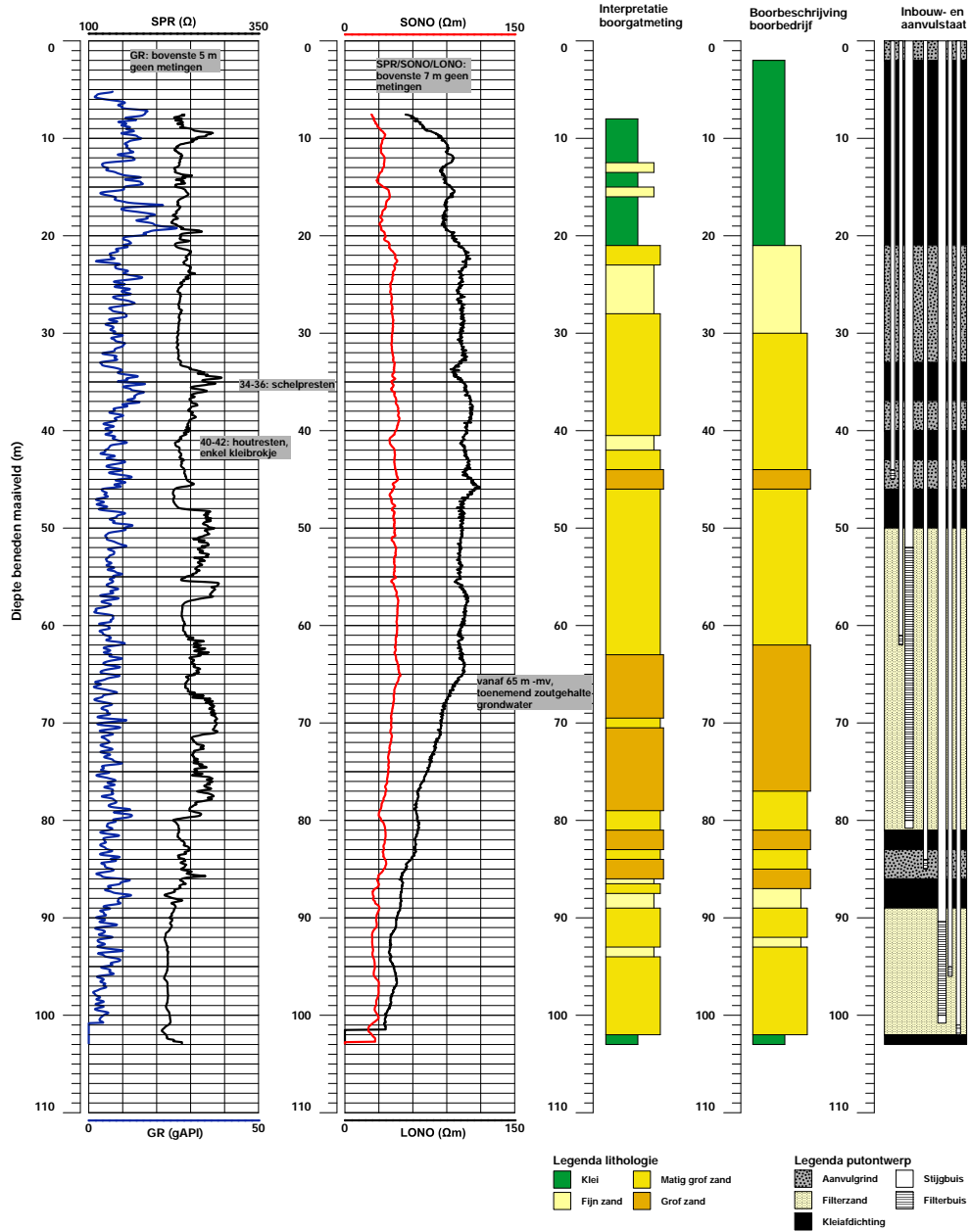


Bijlage 1

Plaatsnaam: Zwaag
 Straatnaam: Leekepad
 RD - coördinaten (m): X: 131280, Y: 520037
 Maaiveldhoogte: 1.6 m NAP
 Datum: 2020-10-27

Naam put: ASR Bron
 Opdrachtgever: PWN
 Boorbedrijf: Tjaden
 Boormethode: Zuigboren & luchtliften
 Diameter boorgat: 9.26 m - mv: 900 mm
 26-103 m - mv: 800 mm





D Hydraulic head change at filter depths in observation wells 19FNW012 and 19FNW004

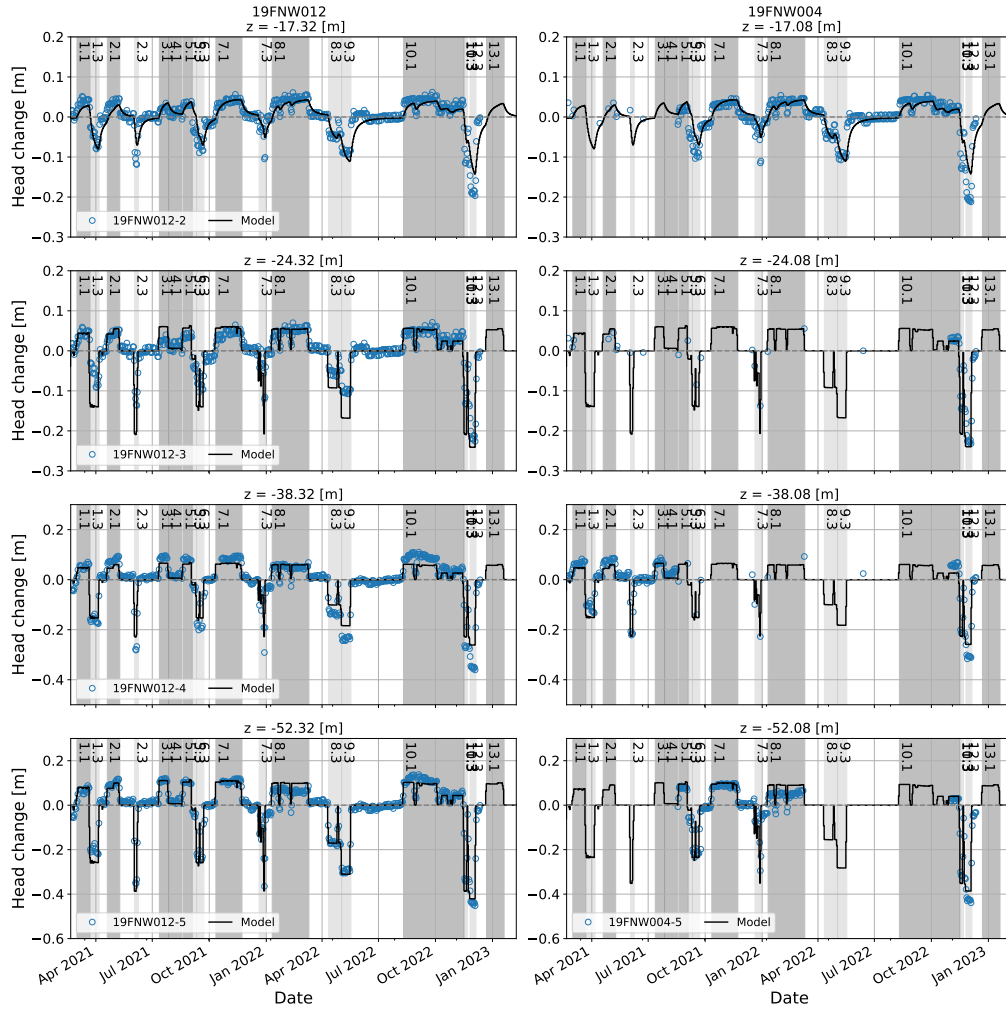


Figure D.1: The changes of hydraulic head measured at different filter depths of observation wells 19FNW012 and 19FNW004 is depicted with model results. The injection periods are indicated in dark gray, while the recovery periods are shown in light gray, along with their corresponding cycle and phase numbers.

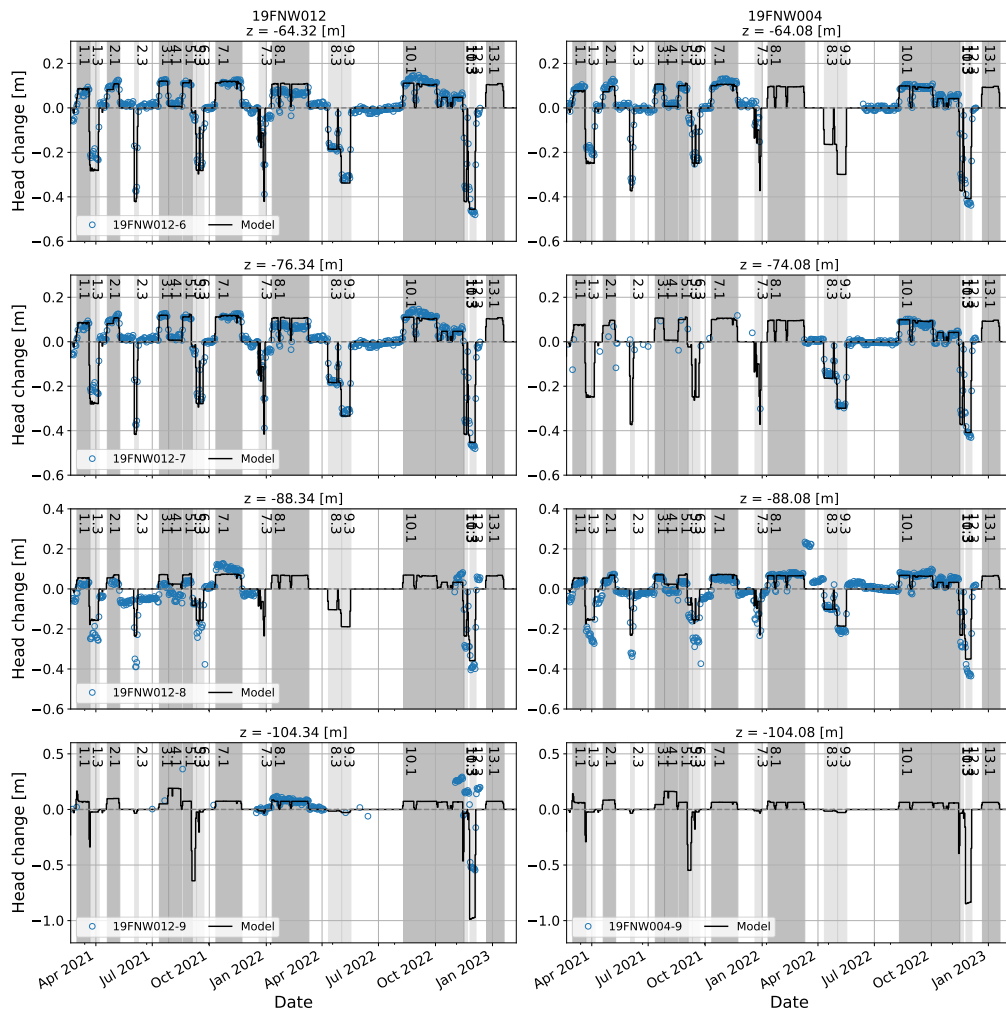


Figure D.2: The changes of hydraulic head measured at different filter depths of observation wells 19FNW012 and 19FNW004 is depicted with model results. The injection periods are indicated in dark gray, while the recovery periods are shown in light gray, along with their corresponding cycle and phase numbers.

E Temperature at filter depths in the pumping well and observation wells

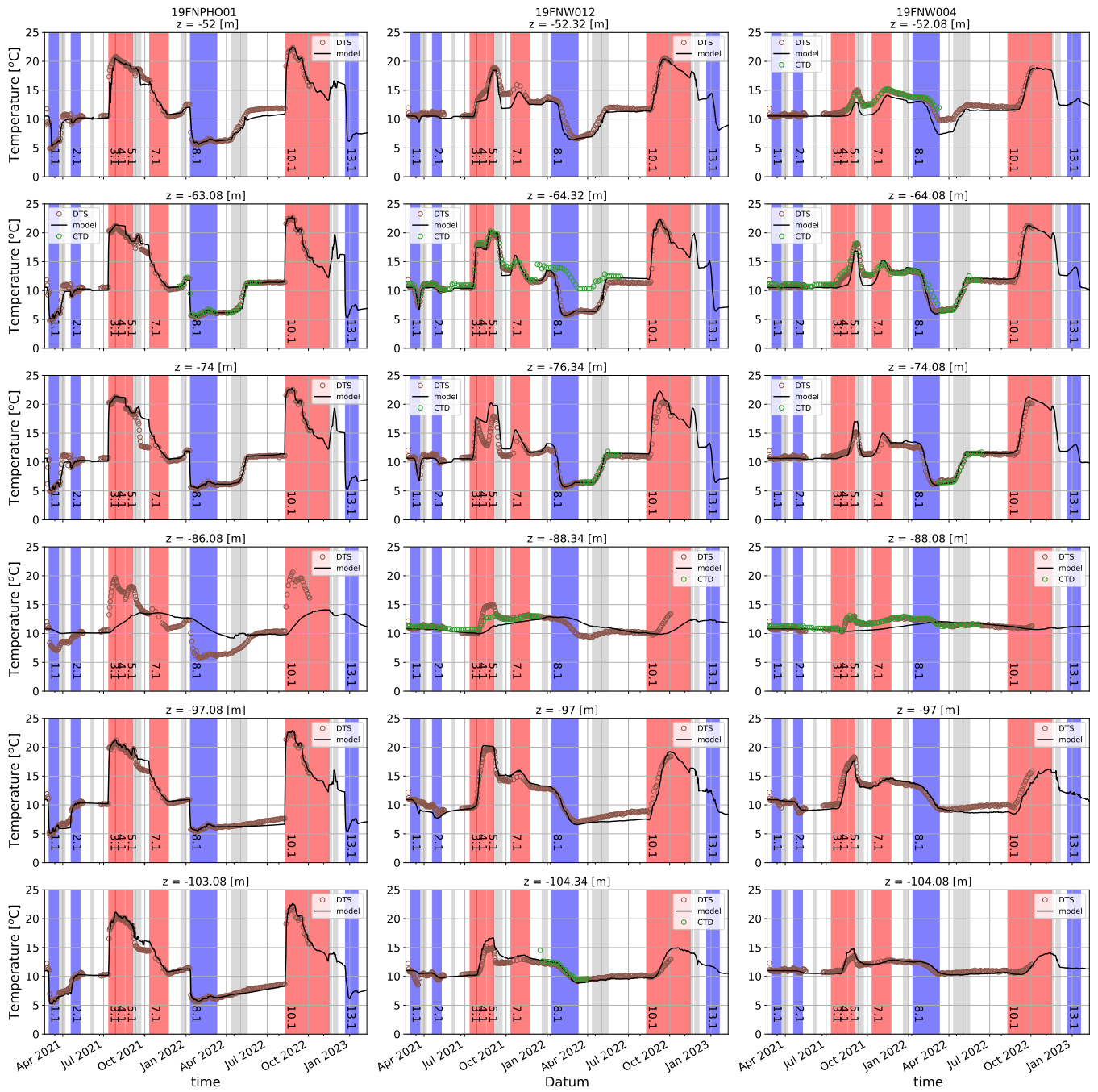


Figure E.1: Changes in temperature during the pilot in the pumping well (19FNPHO01) and two observation wells (19FNW012 and 19FNW004) at different filter depths are depicted. Periods shown in blue indicate when cold water is injected, periods in red indicate the injection of warm water, and the light gray areas represent the recovery periods.

F Electrical Conductivity at filter depths in the pumping well and observation wells

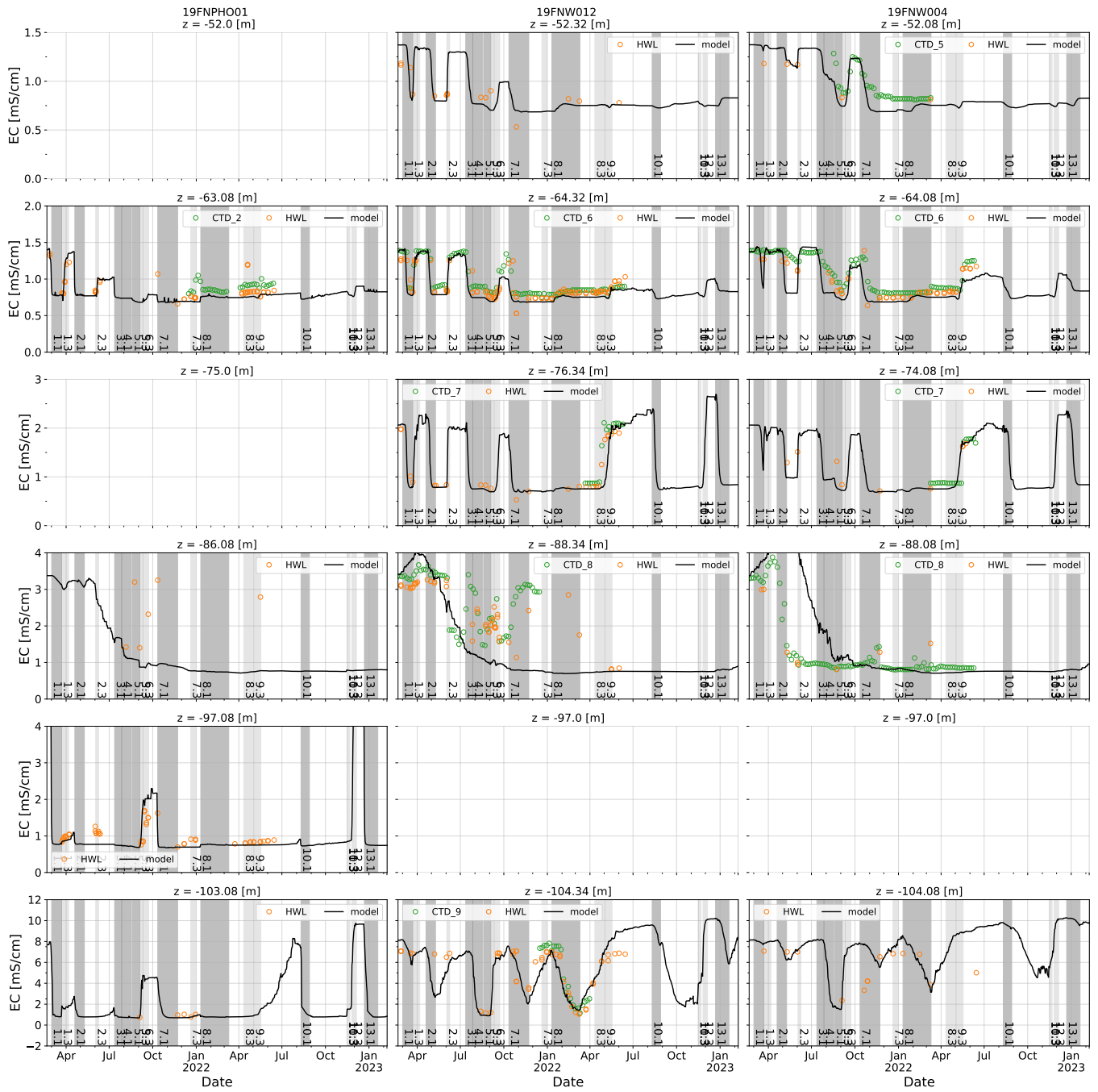


Figure F.1: Changes in EC during the pilot in the two observation wells (19FNW012 and 19FNW004) at different filter depths are depicted. Periods shown in dark gray indicate when water is injected and the light gray areas represent the recovery periods. Empty plots indicate that no CTD or HWL data was available.

G Iterative parameter estimation

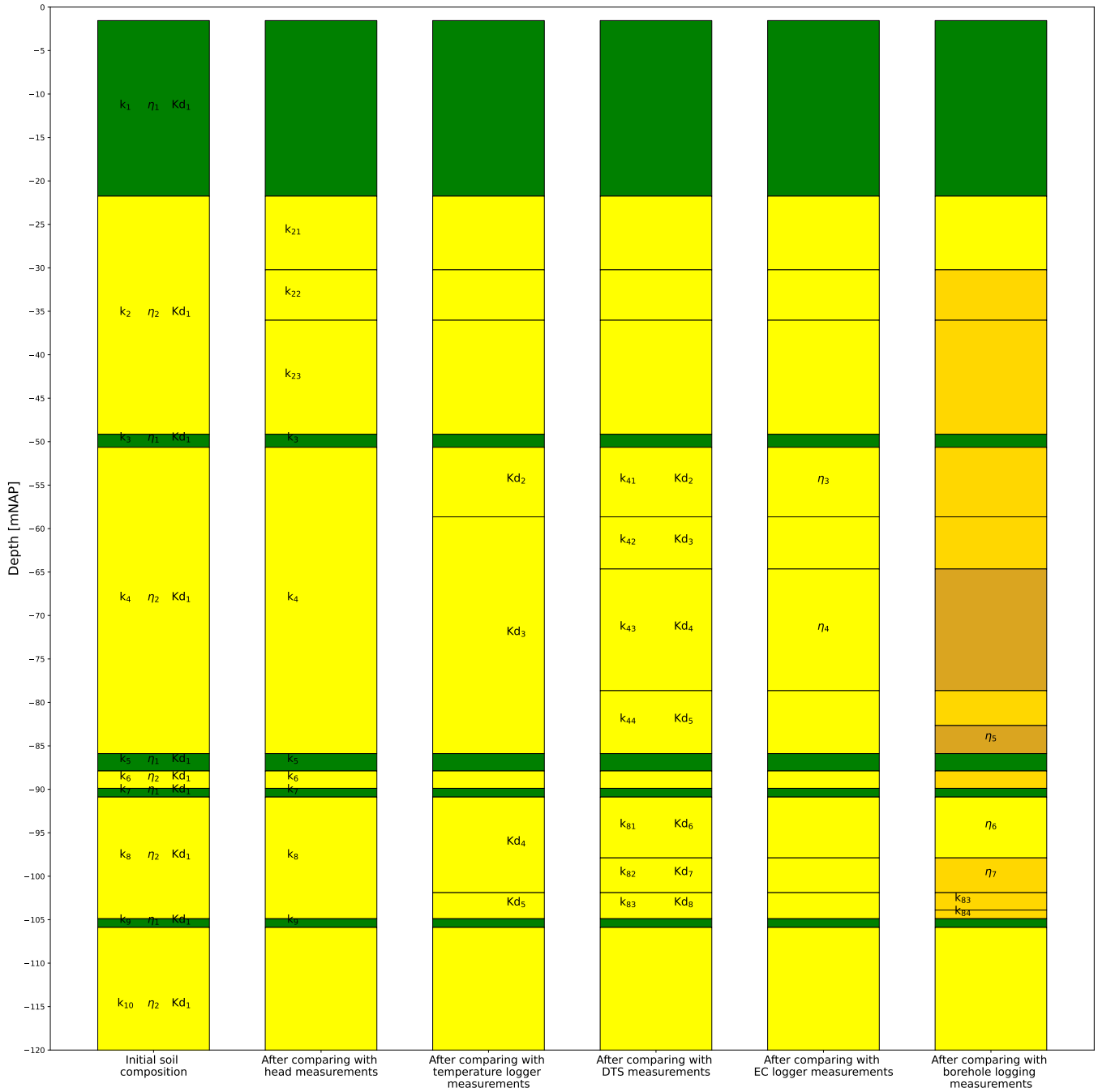


Figure G.1: Soil layers considered after comparing with measurements. Each step is showing the layers and adjusted parameters (hydraulic conductivity (k), porosity (η) and adsorption coefficient for heat transport (K_d)).

H Important python code

H.1 SEAWAT model

The SEAWAT model consists of a combination of modules from MODFLOW2005, MT3DMS, and SEAWAT. The code displaying the utilized modules for each of the three modules is presented below:

```
def setup_gwf_model(name):
    "0: Create model object:"
    gwf_name = 'gwf_' + name
    mf = mdf.Modflow(gwf_name, model_ws=f'data_{name}', exe_name=exe_gwf) #
    Instantiate the MODFLOW model

    "__# 1. Define solver:"
    pcg = mdf.ModflowPcg(mf, hclose=hclose, rclose=rclose, relax=relax, mxiter=
    nouter, iter1=ninner) # Pre-Conditioned Conjugate Gradient (solver)

    "__# 2. Discretization of the model__"
    dis = mdf.ModflowDis(mf, nlay=nlay, nrow=nrow, ncol=ncol, delr=delr, delc=delc
    , top=z[0], botm=z[1:],
                        nper=nper, nstp=nstp, perlen=perlen, tsmult=tsmult,
    itmuni=itmuni, lenuni=lenuni, steady=False)

    "__# 3. Properties of the aquifer__"
    lpf = mdf.ModflowLpf(mf, hk=kh, vka=kv, ss=Ss, sy=Sy, storagecoefficient=False
    , laytyp=icelltype) # layer property flow

    "__# 4. Basic model features__"
    bas = mdf.ModflowBas(mf, ibound=ibound, strt=ic_gwf) # Initial conditons &
    Constant head boundary

    "__# 5. Packages (aquifer features)__"
    wel = mdf.ModflowWel(mf, stress_period_data=welspd)

    "__# 6. Define output__"
    lmt = mdf.ModflowLmt(mf); # link mass transport
    package (for writing linker file)
    oc = mdf.ModflowOc(mf, save_every=1, savebud=True) # Output control

    return mf
```

```
def setup_gwt_model(gwf, name):
    "Setup mt3d model__"
    gwt_name = 'gwt_' + name
    mt = mt3d.Mt3dms(gwt_name, model_ws=f'data_{name}', exe_name=exe_gwt,
    modflowmodel=gwf)

    "Define solver:"
    gcg = mt3d.Mt3dGcg(mt, cclose=hclose, accl=relax, mxiter=nouter, iter1=ninner,
    ncrs=1); # GCG solver

    "Basic transport pakage:"
    timeprs = gwf.modeltime.totim # At which times concentration is saved
    nprs = len(timeprs) # Numper of timeprs
    btn = mt3d.Mt3dBtn(mt, obs=None, prsity=por, icbund=icbund, nprs=nprs,
    timprs=timeprs, nper=nper, nstp=nstp, perlen=perlen, ncomp=2, mcomp=2, sconc=
    sconcl, sconc2=sconc2, species_names=species_names,) # Add species

    "Packages (aquifer features)__"
    ssm = mt3d.Mt3dSsm(mt, stress_period_data=conc_spd) # source/sink mixing
```

```

adv = mt3d.Mt3dAdv(mt, mixelm=mixelm, dceps=dceps, nplane=nplane, npl=npl, np
=nph, npmin=npmin, npmax=npmax, nlsink=nlsink, npsink=npsink, percel=percel,
itrack=itrack, wd=wd, mxpart=30000000) # advection
dsp = mt3d.Mt3dDsp(mt, al=all, trpt=trpt1, trpv=trpt1, dmcoef=dmcoef1,
multiDiff=True, dmcoef2=dmcoef2) # Dispersion
rct = mt3d.Mt3dRct(mt, isothm=isothm, igetsc=0, rhob=rhoB, sp1=Kd1, sp2=None,
sp12=Kd2)
return mt

```

```

def setup_swt_model(gwf, gwt, name):
    "SEAWAT"
    swt_name = 'swt_' + name

    # Create model:
    msw = swt.Seawat(swt_name, modflowmodel=gwf, mt3dmodel=gwt, exe_name=exe_swt,
model_ws=f'data_{name}')

    vdf = swt.SeawatVdf(msw, mfnadvfd=mfnadvfd, iwtable=iwtable, denseref=denseref,
denseslp=denseslp, crhoref=crhoref, indense=indense, dense=dense,)
    vsc = swt.SeawatVsc(msw, mt3dmuflg=mt3dmuflg, viscref=viscref, nsmueos=nsmueos,
mtmuspec=mtmuspec, dmudc=dmudc, cmuref=cmuref, mtmutempspec=mtmutempspec,
visc=visc)
    return msw

```

In the end, the model is a combination of all the used modules. The coupling and execution of the model are done using the following code:

```

def run_models(name):
    mf = setup_gwf_model(name)
    mt = setup_gwt_model(mf, name)
    ms = setup_swt_model(mf, mt, name)

    mf.write_input()
    mf.run_model(silent=True)

    mt.write_input()
    mt.run_model(silent=True)

    ms.write_input()
    ms.run_model(silent=True)

    np.savetxt(f'data_{name}/distances.txt', r, delimiter=',')
    np.savetxt(f'data_{name}/dates.txt', df_spd.Date, delimiter=',')
    layerdata.to_csv(f'data_{name}/layerdata.csv') # layerdata used xl.io
    return mf, mt, ms

```

H.2 Model input

Following files are used:

- data_PLRdag_EXP - kopie_aangepast 3.xlsx
- ASRHoorn_params-dcd.xlsx (referred in code as layerdata)

H.2.1 Discretization

```
itmuni = 4 # 4 = days
lenuni = 2 # 2 = meters

"Layers:"
z = np.zeros(len(layerdata) + 1)
z[0] = layerdata['Top m+NAP'][0] # Top of first layer
z[1:] = layerdata['Bot m+NAP'] # Bottom of each layer
nlay = len(z) - 1 # Number of layers

"Columns and rows:"
delc = 1 # Row spacing in the column direction [m]
nrow = 1 # Number of rows

cell_sizes = [(0, 100, 1.0), # ~(from, to, cell_width)
              (100, 200, 10.0),
              (200, 500, 50.0),
              (500, 1000, 100.0)]

def func_cellBounds(cell_sizes):
    cellBounds = [0] # origin
    number = [ ]

    for rf, rt, cw in cell_sizes:
        interval = list(np.arange(rf, rt, cw) + cw)
        number += [len(interval)]
        cellBounds += interval

    global df_cellBounds
    df_cellBounds = pd.DataFrame()
    df_cellBounds['from'] = np.array(cell_sizes[:, 0])
    df_cellBounds['to'] = np.array(cell_sizes[:, 1])
    df_cellBounds['cell size'] = np.array(cell_sizes[:, 2])
    df_cellBounds['number'] = number

    return np.array(cellBounds)

cellBounds = func_cellBounds(cell_sizes)
delr = np.diff(cellBounds) # Cel width [m]
r = cellBounds[1:] - delr/2 # Middle of each cell [m]
ncol = len(delr) # Number of columns

"Temporal:"
# Start and end date of the spd:
strtDate_spd = PLRdata['datum'].values[0]
endDate_spd = PLRdata['datum'].values[-1]

# Other (changeable) input parameters:
steady = False # Take transient solution
nstp = 1 # Number of time steps in each stress period
perlen = 1 # Length of stress periods
tsmult = 1 # Time step multiplier
```

```

# Create dataframe:
df_spd = pd.DataFrame()

# Discharge data:
df_spd['Date'] = PLRdata['datum']
df_spd['Qdeep'] = -PLRdata['Debiet_Dieep'] / 24
df_spd['Qshallow'] = -PLRdata['Debiet_Ondieep'] / 24

# Set range:
df_spd.index = PLRdata['datum']
df_spd = df_spd[strtDate_spd:endDate_spd]

# Set index to stress period number:
df_spd.index = range(len(df_spd))
df_spd.index.name = 'nr'

# Number of stress periods:
nper = len(df_spd) # Number of stress period

```

H.2.2 Aquifer properties

```

"Type of aquifer:"
icelltype = 0 # Layer type: 0 confined, >0 convertible, <0 convertible unless
              the THICKSTRT option is in effect.

"Conductivity:"
kh_layers = layerdata['K_hor (m/d)'].values # [m/d] - Horizontal hydraulic
conductivity
kv_layers = kh_layers / layerdata['VANI'].values # [m/d] - Vertical hydraulic
conductivity

"Storage:"
Ss_layers = layerdata['Ss(-)'].values # [1/m] - Specific storage
Sy_layers = Ss_layers * abs(np.diff(z)) # [-] - Specific yield/storage
coefficient

"Porosity:"
por_layers = layerdata.Porosity.values # Porosity - [-]

"Size of the slice:"
theta = 2 * np.pi # Take whole cirkel

"Create array's with corresponding sizes:"
kh = np.zeros((nlay, nrow, ncol), dtype=float) # [m/d] - Horizontal hydraulic
conductivity
kv = np.zeros((nlay, nrow, ncol), dtype=float) # [m/d] - Vertical hydraulic
conductivity
Ss = np.zeros((nlay, nrow, ncol), dtype=float) # [1/m] - Specific storage
Sy = np.zeros((nlay, nrow, ncol), dtype=float) # [-] - Specific yield/storage
coefficient
por = np.zeros((nlay, nrow, ncol), dtype=float) # [-] - Porosity

"Fill array with radialized parameters:"
kh[:,0,:] = kh_layers.reshape(nlay, 1) * theta * r # [m.m/d] - horizontal
hydraulic conductivity
kv[:,0,:] = kv_layers.reshape(nlay, 1) * theta * r # [m.m/d] - vertical
hydraulic conductivity
Sy[:,0,:] = Sy_layers.reshape(nlay, 1) * theta * r # [m] - Specific yield

```

```
Ss[:,0,:] = Ss_layers.reshape(nlay, 1) * theta * r # [m.1/m] - Specific
storage
por[:, 0, :] = por_layers.reshape(nlay, 1) * theta * r # [m] - Porosity
```

H.2.3 Initial conditions

```
"Heads:"
ic_gwf = np.ones((nlay, nrow, ncol), dtype=float) * 0 # Initial head in aquifer [m]
          (eigenlijk -2.5 mNap ongeveer)

species_names = ['EC', 'Temperature']

"EC:"
sconcl = np.ones((nlay, nrow, ncol), dtype=float)
sconcl[:,0,:] = layerdata['TDS'].values.reshape(nlay, 1) * np.ones(ncol) # Initial
concentrations --> TDS from layerdata used
sconcl = sconcl / 0.8 #
          Conversion EC vs TDS, according to Vincent Post

"Temperature:"
sconcl2 = np.zeros((nlay, nrow, ncol), dtype=float) # Initial temperature [oC]

# According to DTS data:
def polynomial(A, B, C, D, E, x):
    return A * x**4 + B*x**3 + C * x**2 + D*x + E

A, B, C, D, E = np.array([-2.54792332e-08, -4.98291662e-06, -1.03581121e-04,
1.51961380e-02, 1.10776562e+01])
C1, D1, E1 = np.array([-0.03276278, -0.5116307, 8.92880182])

zmid = (z[:-1] + z[1:]) / 2

Tint = np.zeros(nlay)
Tint[zmid>=-8] = polynomial(A=0, B=0, C=C1, D=D1, E=E1, x=zmid[
zmid>=-8])
Tint[(zmid<-8) & (zmid>=-120)] = polynomial(A, B, C, D, E, zmid[(zmid<-8) & (zmid
>=-120)])
Tint[zmid<-120] = polynomial(A, B, C, D, E, -120)

sconcl2[:, 0, :] = Tint.reshape(nlay, 1) * np.ones(ncol)
```

H.2.4 Model features

Wells:

```
"Input:"
z_19FNPH001_1 = (-53.59, - 81.58) # mNAP
z_19FNPH001_2 = (-91.97, -101.58) # mNAP

printinfo = None

"Assimilation:"
cells_19FNPH001_1 = [] # list with coordinates of the cells where shallow well is
located ~[layer, row, col]
cells_19FNPH001_2 = [] # list with coordinates of the cells where deep well is
located ~[layer, row, col]

pump1_in_layer = False
pump2_in_layer = False
```

```

for i in range(len(z) - 1):
    if z_19FNPH001_1[0] > z[i+1]: pump1_in_layer = True
    if z_19FNPH001_2[0] > z[i+1]: pump2_in_layer = True

    if z_19FNPH001_1[1] > z[i]: pump1_in_layer = False
    if z_19FNPH001_2[1] > z[i]: pump2_in_layer = False

    # Print info and store cells:
    text = ''
    if pump1_in_layer: text += f' \t Shallow pump in layer'; cells_19FNPH001_1 +=
        [[i, 0, 0]] # ~[layer, row, col]
    if pump2_in_layer: text += f' \t Deep pump in layer' ; cells_19FNPH001_2 +=
        [[i, 0, 0]] # ~[layer, row, col]

    if printinfo: print(f'Layer {i}: \t {np.array([z[i], z[i+1]]).round(1)}' +
        text)

# Get k-values for well cells:
ksi = np.array(cells_19FNPH001_1)[: ,0]
kdi = np.array(cells_19FNPH001_2)[: ,0]

# Divide discharge based on k-values (and thickness, but these are equal):
Qs_division = kh_layers[ksi]/sum(kh_layers[ksi])
Qd_division = kh_layers[kdi]/sum(kh_layers[kdi])

# Create dict for the stress period data:
welspd = {} # welspd = {0: [wel_rec0], 1: [wel_rec1], ...}

for sp_nr in range(len(df_spd)):
    __, Qdeep, Qshallow = df_spd.iloc[sp_nr]

    cQ = np.hstack((Qs_division * Qshallow, Qd_division * Qdeep)) * 24 #
    Discharge [m3/d]
    cx, cy, cz = np.array(cells_19FNPH001_1 + cells_19FNPH001_2).T #
    Cell coordinates

    welspd[sp_nr] = list(zip(cx, cy, cz, cQ))

```

Constant head boundary:

```

"MODFLOW model:"
ibound = np.ones((nlay, nrow, ncol), dtype=int) # Regular active cells
(1)
ibound[:, 0, -1] = -1 # Constant head boundary
(-1)

"Mt3ds model:"
icbund = np.ones((nlay, nrow, ncol)) # Boundary condition: 0 = inactive,
<0 = constant, >0 = active
icbund[:, 0, -1] = -1 # Constant concentration boundary
(-1)

"Stress period data:"
# Create dataframe:
df_Cin_spd = pd.DataFrame()

# Input data:
df_Cin_spd['Tdeep'] = PLRdata['HOI002_TT10_corr'].interpolate()
df_Cin_spd['Tshallow'] = PLRdata['HOI001_TT10_corr'].interpolate()
df_Cin_spd['ECdeep'] = PLRdata['HOI002_QT10_corr20'].fillna(500) / 1000
df_Cin_spd['ECshallow'] = PLRdata['HOI001_QT10_corr20'].fillna(500) / 1000

```

```

# Set index:
df_Cin_spd.index          = PLRdata['datum']
df_Cin_spd.index.name    = 'Date'

# Set range:
df_Cin_spd = df_Cin_spd[strtDate_spd:end_Date_spd]

"Input"
# EC:
Cshal = df_Cin_spd['ECshallow']
Cdeep = df_Cin_spd['ECdeep']
cchd  = 1.25 # [mS/cm]

# Temperature:
Tshal = df_Cin_spd['Tshallow']
Tdeep = df_Cin_spd['Tdeep']
Tchd  = 11.5 # [oC]

"Assimilation:"
# Type of source:
itype = mt3d.Mt3dSsm.itype_dict()

# Function to compute a record for 1 specific stress period (considering well
  cells):
def func_conc_rec(cwell_1, cwell_2, Twell_1, Twell_2):
    # from ~[layer, row, col] to ~[layer, row, col, concentration, source]
    conc_rec_well1 = list(map(lambda ci: ci + [1] + [itype['WEL']] + [cwell_1] + [
    Twell_1], cells_19FNPH001_1))
    conc_rec_well2 = list(map(lambda ci: ci + [1] + [itype['WEL']] + [cwell_2] + [
    Twell_2], cells_19FNPH001_2))
    conc_rec_chd   = [[0, 0, ncol-1, 1, itype['CHD'], cchd, Tchd]]
    return conc_rec_well1 + conc_rec_well2 + conc_rec_chd

# Create stress period data:
conc_spd = {} # ~{0: [(0, 0, 0, cwell, itype['WEL']), (0, 0, ncol-1, cchd, itype['
  CHD'])],
              # 1: [(0, 0, 0, 0.0, itype['WEL']), (0, 0, ncol-1, cchd, itype['
  CHD'])],}

for i in range(nper):
    conc_spd[i] = func_conc_rec(Cshal[i], Cdeep[i], Tshal[i], Tdeep[i])

```

Advection:

```

"Solver method:"
mixelm = 3 # Advection solution option: 0 = standard finite-difference, 1 =
  forward-tracking MOC, 2 = backward-tracking MMOC, 3 = hybrid HMOC, -1 =
  third-order TVD scheme
itrack = 3 # Particle-tracking algorithm: 1 =
  first-order Euler, 2 = fourth-order Runge-Kutta, 3 = hybrid first- and
  fourth-order algorithm
nplane = 0 # Pattern for initial placement: 0 = random pattern, >0 = fixed pattern

"Number of initial particles per cell to be placed at cells:"
npl = 0 # Where the Relative Cell Concentration Gradient is less than or equal to
  DCEPS
nph = 16 # Where the Relative Cell Concentration Gradient is greater than DCEPS

"Particles allowed per cell:"
npmin = 3 # Minimum
npmax = 32 # Maximum

```



```

"Correction factors:"
percel = 7.5 # Courant number (i.e., the number of cells, or a fraction of a cell)
          advection will be allowed in any direction in one transport step.
wd      = 0.7 # Concentration weighting factor

"Gradient boundaries:"
dceps  = 1e-5 # A small Relative Cell Concentration Gradient below which advective
            transport is considered
dchmoc = 1e-3 # Critical Relative Concentration Gradient for controlling the
            selective use of either MOC or MMOC in the HMOC solution scheme.

"MMOC settings:"
nlsink = nplane # Flag indicating whether the random or fixed pattern is selected
            for initial placement of particles to approximate sink cells in the MMOC
            scheme
npsink = nph    # Number of particles used to approximate sink cells in the MMOC
            scheme

```

Dispersion:

```

"EC:"
all     = 0.1      # Longitudinal dispersivity [m]
trpt1   = 1       # Ratio of the horizontal transverse dispersivity to the
            longitudinal dispersivity
dmcoef1 = 8.64e-5 # Effective molecular diffusion coefficient [m2/d]

"Temperatuur:"
dmcoef2 = 0.14   # Effective molecular diffusion coefficient [m2/d]

```

Retardation:

```

isothm = 1        # 1 = Linear isotherm (equilibrium-controlled);
rhoB    = 1961    # [kg/m3] - Bulk density
rhoB    = np.array([[r * theta * rhoB]] * nlay) # [kg.m/m3] - Bulk density

"EC:"
Kd1_layers = 0 # [m3/kg] - Adsorption coefficient

"Temperature"
Kd2_layers = layerdata['Kd2'].values # [m3/kg] - Adsorption coefficient

Kd2_layers.reshape(nlay,1) * np.ones(ncol)

```

Buoyancy

```

mfnavdfd = 2 # internodal conductance values used to
            conserve fluid mass are calculated using a central-in-space algorithm
iwttable = 0 # IWTABLE = 0 -> Water-table correction
            will NOT be applied.
denseref = 1000 # rho_inj: fluid density at the reference
            concentration, temperature, and pressure
denseslp = 0.7143 # drhodc: slope of the linear equation of
            state that relates fluid density to solute concentration (Guo & Langevin 2002:
            0.7143)
crhoref  = 0 # Reference concentration (C0) for species
indense  = 1 # INDENSE >= 1, values for the DENSE array
            will be read
dense    = denseref + sconcl * denseslp # Fluid density array read for each layer

```

H.2.5 Solver criteria

```
hclose, rclose = 1e-3, 1e-3
nouter, ninner = 10000, 10000
relax          = 1.0
```